Journal of Nanomaterials

Diamond and Related Nanomaterials for MEMS/NEMS Applications

Guest Editors: Rakesh K. Joshi and Ashok Kumar

Diamond and Related Nanomaterials for MEMS/NEMS Applications

Journal of Nanomaterials

Diamond and Related Nanomaterials for MEMS/NEMS Applications

Guest Editors: Rakesh K. Joshi and Ashok Kumar

Contents

Hindawi Publishing Corporation
Journal of Nanomaterials
Volume 2009, Article ID 637530, 1 page
doi:10.1155/2009/637530

Editorial

Diamond and Related Nanomaterials for MEMS/NEMS Applications

Rakesh K. Joshi and Ashok Kumar

Department of Mechanical Engineering, University of South Florida, Tampa, FL 33620, USA

Correspondence should be addressed to Rakesh K. Joshi, joshi@eng.usf.edu

Received 28 July 2009; Accepted 28 July 2009

Diamond materials offer great potential for electronic and biomedical application. Properties like very high stiffness, thermal conductivity, optical transparency range, chemical stability and erosion resistance for the diamond based materials extend their applicability for several aspects of science and technology. Nanostructures of diamond materials have extraordinary multifunctional properties such as high thermal conductivity and a Youngs modulus value close to the one for single crystal diamond. Controlled nucleation and growth of nanocrystalline diamond along with their applicability for MEMS and NEMS structures are useful of future generation sensor platforms. Researchers around the world have been putting their efforts to achieve high precision in the direction of fabricating the devices based on diamond materials. Nanomanufacturing of such devices requires the controlled design of nanoscale diamond structures.

This issue covers various topics related to carbon-based nanomaterials. The first article by Hanada et al. reports deposition process of ultrananocrystalline diamond films. Authors have demonstrated application of pulse laser deposition for diamond growth. The second article (by Ohmagari et al.) in this issue is about atomic bonding configuration of ultrananocrystalline diamond (UNCD)/hydrogenated amorphous carbon (a-C: H) films, where authors have used near-edge X-ray absorption fine structure spectroscopy. The third article (by Teng et al.) is about structural transformation upon nitrogen doping of ultrananocrystalline diamond films. Tanaka et al. report high-resolution magnetic force microscopy using carbon nanotube probes in the fourth article of this issue. In the fifth article, Tung et al. report fabrication of carbon nanotubes STM tips by liquid catalyst-assisted microwave plasma-enhanced chemical vapor deposition. In a similar type of study, Sakamoto et al. (the sixth article) report fabrication of Pd-filled carbon nanotubes for SPM applications. In the seventh article (by Katzenmeyer et al.), the authors report Poly (hydridocarbyne) as highly processable insulating polymer precursor to micro/nanostructures and graphite conductors. In the concluding article, I. Chasiotis and K. N. Jonnalagadda report strength and fracture resistance of amorphous diamond-like carbon films for MEMS applications.

Acknowledgments

We thank all the contributing authors and reviewers for their help in putting together this special issue. The authors also thank the Editor-in-Chief of the Journal of Nanomaterials, Dr. Michael Z. Hu, for his support and encouragement. The authors highly appreciate Dr. Hu's contribution to the Journal of Nanomaterials.

Rakesh K. Joshi
Ashok Kumar

Hindawi Publishing Corporation
Journal of Nanomaterials
Volume 2009, Article ID 901241, 6 pages
doi:10.1155/2009/901241

Research Article

Time-Resolved Observation of Deposition Process of Ultrananocrystalline Diamond/Hydrogenated Amorphous Carbon Composite Films in Pulsed Laser Deposition

Kenji Hanada,[1] Takashi Nishiyama,[2] Tsuyoshi Yoshitake,[1] and Kunihito Nagayama[2]

[1] *Department of Applied Science for Electronics and Materials, Kyushu University, 6-1 Kasuga, Fukuoka 816-8580, Japan*
[2] *Department of Aeronautics and Astronautics, Kyushu University, 744 Motooka, Nishi-ku, Fukuoka 819-0395, Japan*

Correspondence should be addressed to Tsuyoshi Yoshitake, yoshitake@asem.kyushu-u.ac.jp

Received 1 November 2008; Accepted 25 November 2008

Recommended by Rakesh Joshi

Optical emission spectroscopy was used to study pulsed laser ablation of graphite in a hydrogen atmosphere wherein ultrananocrystalline diamond (UNCD)/hydrogenated amorphous carbon (a-C:H) composite films were grown on heated substrates. Time-resolved photographs of a plume that expanded from a laser-irradiation spot toward a substrate were taken using a high-speed ICCD camera equipped with narrow-bandpass filters. While the emissions from C atoms and C_2 dimers lasted above the laser-irradiation spot on the target, the emission from C^+ ions lasted above the substrate surface for approximately 7 microseconds, although the emission lifetime of species is generally approximately 10 nanoseconds. This implies that C^+ ions actively collided with each other above the substrate surface for such a long time. We believe that the keys to UNCD growth in PLD are the supply of highly energetic carbon species at a high density to the substrate and existence of atomic hydrogen during the growth.

1. Introduction

Ultrananocrystalline diamond (UNCD) films are new candidates for hard coatings, semiconducting devices, and microelectromechanical systems (MEMSs). UNCD is obviously distinguished from nanocrystalline diamond (NCD). The grain sizes of NCD and UNCD have been quoted as less than 100 nm and 2–15 nm, respectively [1]. UNCD films are structurally characterized by the existence of grain boundaries with volume fractions more than 10% for the total and coexistence of a great proportion of amorphous carbon in the films [1], which induces an extremely large optical absorption [2]. In addition, it is possible for a highly nitrogenated film to possess a high *n*-type conductivity [3, 4].

The UNCD films have mostly been fabricated by chemical vapor deposition (CVD) [5]. It is well known that C_2 dimers have an important role in the growth of UNCD films by CVD [6]. Recently, we have succeeded in growing UNCD films, wherein 5-nm diamond crystallites are embedded in a hydrogenated amorphous carbon (a-C:H) matrix, in a hydrogen atmosphere by pulsed laser deposition (PLD) with a graphite target [7, 8]. They can be grown at low substrate temperatures and high deposition rates. In addition, while CVD necessitates the pretreatment of substrates on the surface of which diamond crystallites are seeded using diamond powders [6, 9], pulsed laser deposition (PLD) does not. In other words, PLD enables not only the growth of UNCD films but also the nucleation of diamond. Since the deposition conditions in PLD are completely different from those in CVD, there must be a difference in the UNCD growth mechanism.

In this paper, we discuss the UNCD growth mechanism in PLD on the basis of previous reports and the experimental results of this study. In this study, we deposited UNCD films, and by using a high-speed intensified charge-coupled (ICCD) camera, we observed the ablation process of graphite under the deposition conditions of these films. Further, we evaluated the structure of the deposited films.

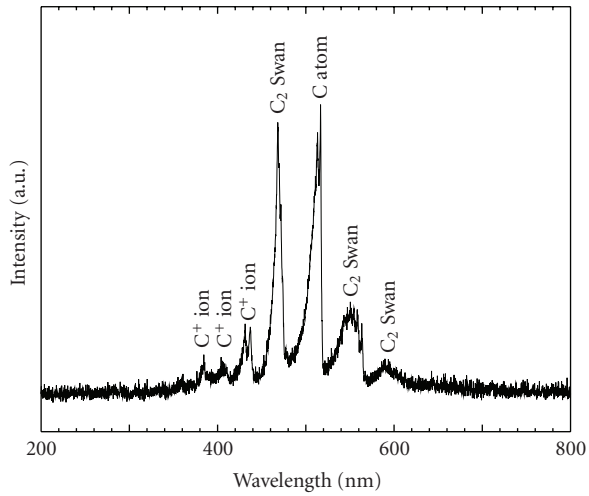

Figure 1: Optical emission spectrum of the entire plume.

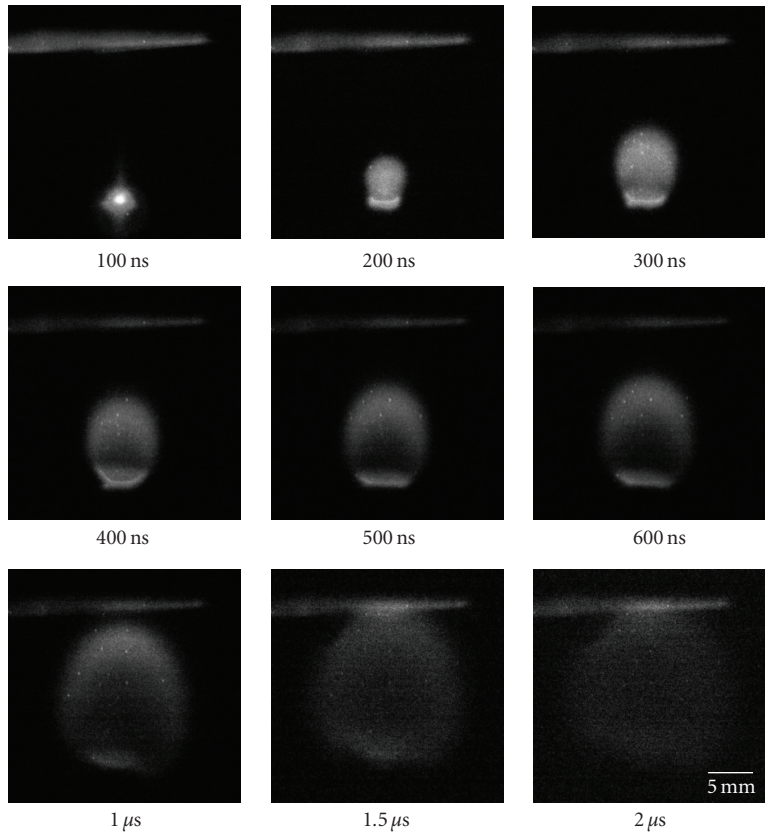

Figure 2: Time-resolved photographs taken without using a filter.

2. Experimental Section

Optical emission spectroscopy was used to study the laser ablation process. Observations were made under the optimum deposition condition of the UNCD/a-C:H films. The film preparation conditions have been detailed in our previous papers [2, 10]. Optical emission spectra of a plume were measured in the wavelength region of 200 to 800 nm by using a multichannel spectrometer (Ocean Photonics, USB4000). Time-resolved plume images were recorded using an ICCD camera system (C7972-11) capable of recording 12-bit images and equipped with

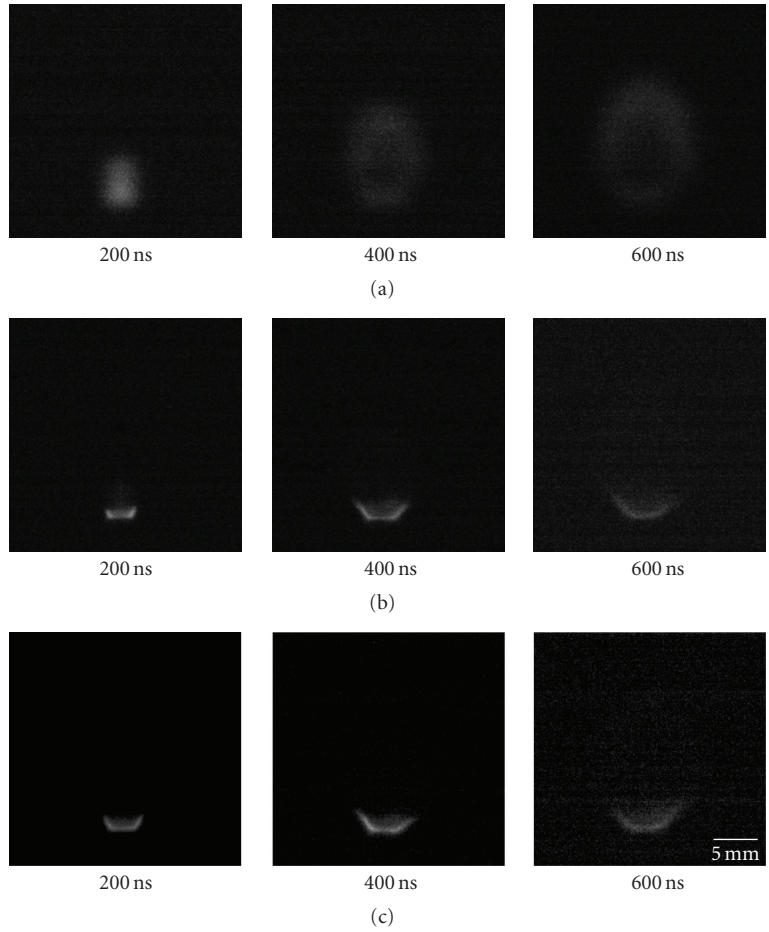

FIGURE 3: Time-resolved photographs captured using (a) 394-nm (C^+ ion), (b) 505-nm (C atom), and (c) 515-nm (C_2 dimer) bandpass filters.

an 18-mm diameter image intensifier and a 1024×1024 pixel CCD array. In order to observe the behavior of C^+ ions, C atoms, and C_2 dimers separately, narrow-bandpass filters transparent to the wavelengths of 394, 505, and 515 nm were placed between the vacuum chamber and the lens. The wavelengths of 394, 505, and 515 nm correspond to those of the representative emission lines of C^+ ions, C atoms, and C_2 dimers, respectively. The images were taken from laser-irradiation until the plume disappeared, at an interval of 100 nm and an exposure time of 20 ns.

3. Results and Discussion

A typical optical emission spectrum of the plume is shown in Figure 1. The spectrum is continuous at wavelengths between 300 and 700 nm, and the intense peaks that originate from C_2 Swan bands, C atoms, and C^+ ions were broadened. This is evidently due to Bremsstrahlung radiation. High-density plasma that is similar to previously reported ablation plumes was formed [11]. The emission intensity was markedly large in the area surrounding the laser irradiation spot on the target. The spectrum shown in Figure 1 predominantly comprises the emissions from that area.

Figure 2 shows the time-resolved plume images captured using the high-speed ICCD camera without a bandpass filter. The plume gradually expanded with time. It is well known that a plume expands behind a traveling shock wave in this pressure range [11]. Although the emission lifetimes of species are approximately 10 nanoseconds in general [11], the emission lasted up to 20 μs. This indicates that the plume has a sufficiently high density for the species to collide with each other. The plume front area located behind the shock wave markedly emitted since the species ejected from the target caught up with the shock wave and gathered inside this area [12]. The front edge of the plume reached the substrate, which was 15 mm away from the target, at delay times between 1.0 and 1.5 μs. After that, the emission above the substrate surface further lasted for several microseconds. This evidently implies that high densities of species are present above the substrate surface for such a long time. This situation must have a significant role in UNCD growth.

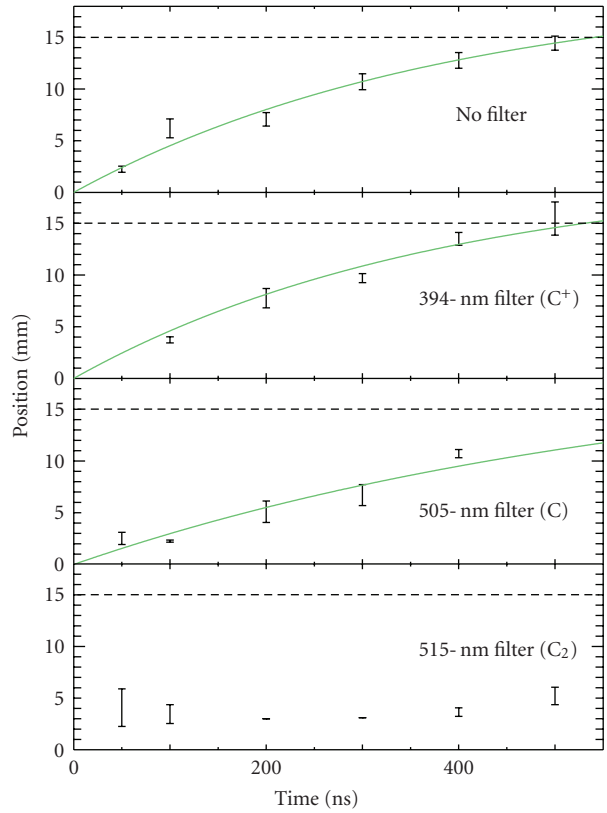

Figure 4: Change in the front-edge position of the plume with time. Here, the laser-irradiation spot is defined as the origin.

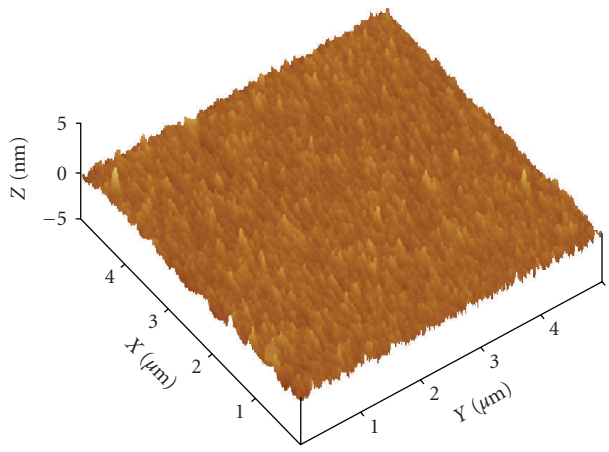

Figure 5: AFM image of the UNCD/a-C:H film deposited on Si.

In order to observe the behavior of C^+ ions, C atoms, and C_2 dimers in the plume separately, time-resolved images were taken using narrow-bandpass filters. Typical time-resolved images for C^+ ions, C atoms, and C_2 dimers are shown in Figures 3(a), 3(b), and 3(c), respectively. While the emissions from C atoms and C_2 dimers lasted around the target, the emission from C^+ ions was observed for 7 μs above the substrate surface. The emission observed above the substrate surface in the images captured without using the filters is evidently attributable to C^+ ions. It was evidently shown that high-energy C^+ ions are present in high density above the substrate surface.

In Figure 4, the plume's front-edge position from the target surface is plotted as a function of time. The front-edge positions were carefully determined from the images that were digitally analyzed using image processing software. The plume expansion was fitted with the drag model [12], and the expansion velocity at the substrate was estimated to be 14 km/s for C^+ ions. For the other species, the expansion velocities were impossible to be estimated since their emissions disappeared from the front edge of the plume.

On the basis of previous reports and the experimental results of this study, the UNCD growth mechanism can be considered to be as follows. (i) The root-mean-square roughness of the film surface was estimated to be 0.6 nm by using atomic force microscopy (AFM), as shown in Figure 5. This value is extremely small as compared to that of the UNCD films prepared by CVD [13]. This implies that UNCD crystallites are formed at a subsurface rather than the film surface. It has been reported that diamond nucleation occurs when highly energetic C^+ ions are implanted into amorphous carbon [14]. This does not contradict the fact that the pretreatment of substrates is not required for PLD, while it is indispensable for CVD. We believe that the supply of highly energetic C^+ ions at a high density to the substrate has an important role in UNCD growth in PLD. Here we must emphasize that this does not have the predominant role on the UNCD growth because the UNCD crystallites do not grow in vacuum wherein the velocities of species must be greater than those in 53.3 Pa hydrogen atmospheres. Although a 53.3 Pa hydrogen atmosphere reduces the mean-free-paths and velocities of species, it is indispensable for UNCD growth in PLD. (ii) It has been theoretically predicted that carbon clusters whose dangling bonds are terminated by atomic hydrogen and whose sizes are smaller than 3 nm will energetically prefer a tetrahedral structure (diamond) to a hexagonal one (graphite) [15]. The UNCD crystallites grown by PLD have an average size of 5 nm. This size is close to the predicted value of 3 nm. Since UNCD growth by PLD requires a hydrogen atmosphere, the existence of atomic hydrogen during UNCD film deposition might contribute to UNCD growth in the mechanism mentioned above. (iii) It has been reported that diamond nucleation is induced under supersaturated conditions [16]. In other words, UNCD crystallites can be formed under supersaturated conditions without pretreating the substrates. Supersaturated conditions might be realized by the presence of high-density C^+ ions on the substrate surface. The probable mechanisms mentioned above are summarized in Figure 6. We believe that these mechanisms (i), (ii), and (iii) interactively contribute to UNCD growth in PLD.

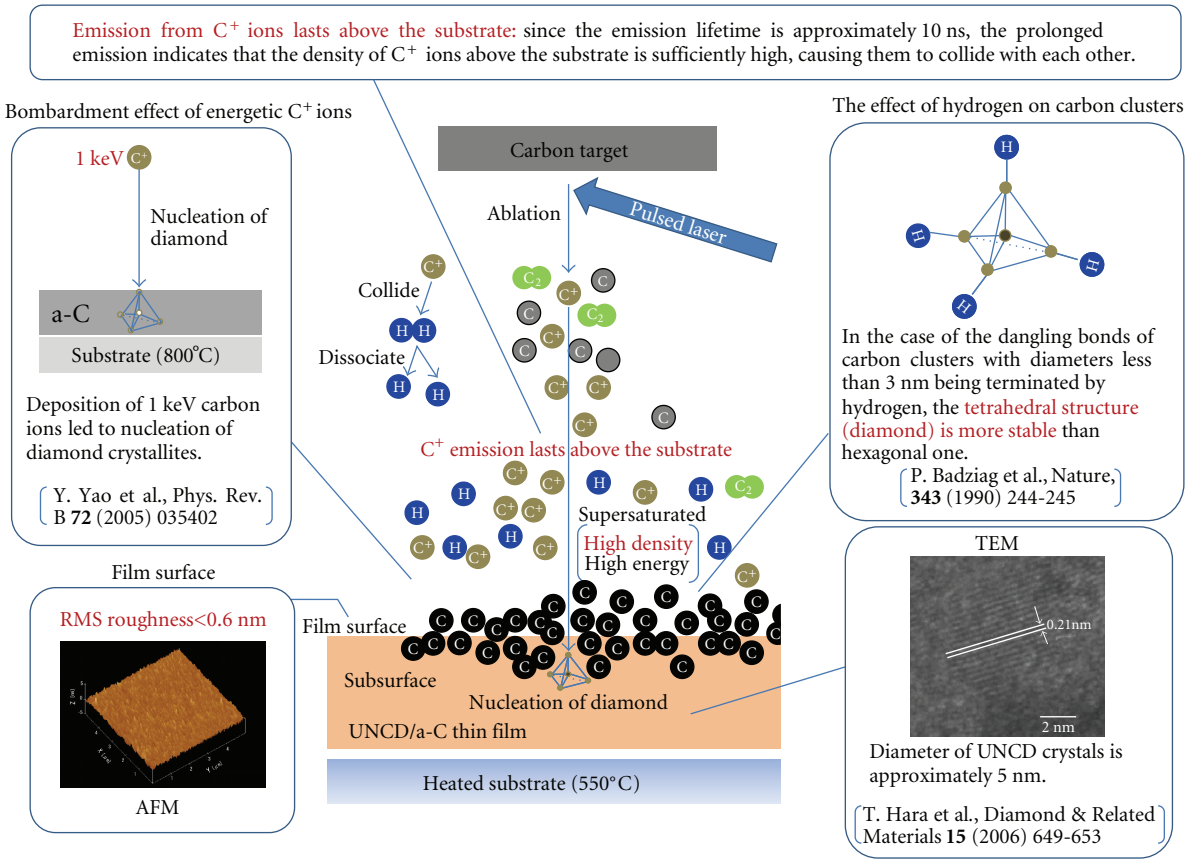

Figure 6: Schematic diagram of probable growth mechanisms of UNCD crystallites in the film, based on previous reports and our experimental results.

4. Conclusions

Optical emission spectroscopy was used to study pulsed laser ablation of graphite in a hydrogen atmosphere wherein UNCD films were grown. Time-resolved photographs were taken using a high-speed ICCD camera equipped with 394-, 505-, and 515-nm filters. Emissions from C atoms and C_2 dimers lasted around the laser-irradiation spot on the target. On the other hand, emission from C^+ ions lasted above the target surface for approximately 7 microseconds, although the emission lifetime is approximately 10 nanoseconds. This implies that C^+ ions actively collide with each other above the substrate surface for such a long time. We believe that the keys to UNCD growth in PLD are the supply of energetic carbon species at a high density to the substrate and existence of atomic hydrogen during the growth.

References

[1] O. A. Williams and M. Nesládek, "Growth and properties of nanocrystalline diamond films," *Physica Status Solidi (A)*, vol. 203, no. 13, pp. 3375–3386, 2006.

[2] T. Yoshitake, A. Nagano, M. Itakura, N. Kuwano, T. Hara, and K. Nagayama, "Spectral absorption properties of ultrananocrystalline diamond/amorphous carbon composite thin films prepared by pulsed laser deposition," *Japanese Journal of Applied Physics Part 2*, vol. 46, no. 36–40, pp. L936–L938, 2007.

[3] O. A. Williams, S. Curat, J. E. Gerbi, D. M. Gruen, and R. B. Jackman, "*n*-type conductivity in ultrananocrystalline diamond films," *Applied Physics Letters*, vol. 85, no. 10, pp. 1680–1682, 2004.

[4] P. Achatz, O. A. Williams, P. Bruno, D. M. Gruen, J. A. Garrido, and M. Stutzmann, "Effect of nitrogen on the electronic properties of ultrananocrystalline diamond thin films grown on quartz and diamond substrates," *Physical Review B*, vol. 74, no. 15, Article ID 155429, 7 pages, 2006.

[5] C. Poppv, W. Kulisch, S. Boycheva, K. Yamamoto, G. Ceccone, and Y. Koga, "Structural investigation of nanocrystalline diamond/amorphous carbon composite films," *Diamond and Related Materials*, vol. 13, no. 11-12, pp. 2071–2075, 2004.

[6] F. Bénédic, G. Lombardi, K. Hassouni, F. Mohasseb, and A. Gicquel, "Plasma-assisted synthesis: plasma experimental diagnostics and modeling," in *Ultrananocrystalline Diamond Synthesis, Properties, and Applications*, O. A. Shenderova and D. M. Gruen, Eds., William Andrew, New York, NY, USA, 2006.

[7] T. Yoshitake, T. Hara, T. Fukugawa, et al., "Low-temperature growth of nanocrystalline diamond by reactive pulsed laser deposition under a hydrogen atmosphere," *Japanese Journal of Applied Physics*, vol. 43, no. 2B, pp. L240–L242, 2004.

[8] T. Hara, T. Yoshitake, T. Fukugawa, et al., "Ultrananocrystalline diamond prepared by pulsed laser deposition,"

Diamond and Related Materials, vol. 15, no. 4–8, pp. 649–653, 2006.

[9] C. Popov, S. Bliznakov, and W. Kulisch, "Influence of the substrate nature on the properties of nanocrystalline diamond films," *Diamond and Related Materials*, vol. 16, no. 4–7, pp. 740–743, 2007.

[10] A. Nagano, T. Yoshitake, T. Hara, and K. Nagayama, "Optical properties of ultrananocrystalline diamond/amorphous carbon composite films prepared by pulsed laser deposition," *Diamond and Related Materials*, vol. 17, no. 7–10, pp. 1199–1202, 2008.

[11] D. B. Geohegan, "Diagnostics and characteristics of laser-produced plasmas," in *Pulsed Laser Deposition of Thin Films*, G. Hubler and D. B. Chrisey, Eds., John Wiley & Sons, New York, NY, USA, 1994.

[12] D. B. Geohegan, "Fast intensified-CCD photography of $YBa_2Cu_3O_{7-x}$ laser ablation in vacuum and ambient oxygen," *Applied Physics Letters*, vol. 60, no. 22, pp. 2732–2734, 1992.

[13] C. Popov, W. Kulisch, P. N. Gibson, G. Ceccone, and M. Jelinek, "Growth and characterization of nanocrystalline diamond/amorphous carbon composite films prepared by MWCVD," *Diamond and Related Materials*, vol. 13, no. 4–8, pp. 1371–1376, 2004.

[14] Y. Yao, M. Y. Liao, Th. Köhler, et al., "Diamond nucleation by energetic pure carbon bombardment," *Physical Review B*, vol. 72, no. 3, Article ID 035402, 5 pages, 2005.

[15] P. Badziag, W. S. Verwoerd, W. P. Ellis, and N. R. Greiner, "Nanometre-sized diamonds are more stable than graphite," *Nature*, vol. 343, no. 6255, pp. 244–245, 1990.

[16] W. Kulisch, *Deposition of Diamond-Like Superhard Materials*, chapter 4, Springer, Berlin, Germany, 1999.

Hindawi Publishing Corporation
Journal of Nanomaterials
Volume 2009, Article ID 876561, 5 pages
doi:10.1155/2009/876561

Research Article

Near-Edge X-Ray Absorption Fine Structure of Ultrananocrystalline Diamond/Hydrogenated Amorphous Carbon Films Prepared by Pulsed Laser Deposition

Shinya Ohmagari,[1] Tsuyoshi Yoshitake,[1] Akira Nagano,[1] Sausan AL-Riyami,[1] Ryota Ohtani,[2] Hiroyuki Setoyama,[2] Eiichi Kobayashi,[2] and Kunihito Nagayama[3]

[1] *Department of Applied Science for Electronics and Materials, Kyushu University, 6-1 Kasuga, Fukuoka 816-8580, Japan*
[2] *Kyushu Synchrotron Light Research Center, 8-7 Yayoigaoka, Tosu, Saga 841-0005, Japan*
[3] *Department of Aeronautics and Astronautics, Kyushu University, 744 Motooka, Nishi-ku, Fukuoka 819-0395, Japan*

Correspondence should be addressed to Tsuyoshi Yoshitake, tsuyoshi_yoshitake@kyudai.jp

Received 17 January 2009; Revised 17 January 2009; Accepted 19 February 2009

Recommended by Rakesh Joshi

The atomic bonding configuration of ultrananocrystalline diamond (UNCD)/hydrogenated amorphous carbon (a-C:H) films prepared by pulsed laser ablation of graphite in a hydrogen atmosphere was examined by near-edge X-ray absorption fine structure spectroscopy. The measured spectra were decomposed with simple component spectra, and they were analyzed in detail. As compared to the a-C:H films deposited at room substrate-temperature, the UNCD/a-C:H and nonhydrogenated amorphous carbon (a-C) films deposited at a substrate-temperature of 550°C exhibited enhanced π^* and $\sigma^*C\equiv C$ peaks. At the elevated substrate-temperature, the π^* and $\sigma^*C\equiv C$ bonds formation is enhanced while the σ^*C–H and σ^*C–C bonds formation is suppressed. The UNCD/a-C:H film showed a larger σ^*C–C peak than the a-C film deposited at the same elevated substrate-temperature in vacuum. We believe that the intense σ^*C–C peak is evidently responsible for UNCD crystallites existence in the film.

1. Introduction

Ultrananocrystalline diamond (UNCD) films comprising diamond crystallites with diameters less than 10 nm and an amorphous carbon matrix [1, 2] have attracted considerable attention from the physical and technological viewpoints because of the following features: (i) some properties resembling those of diamond and sp^3-rich amorphous carbon, so-called diamond-like carbon (DLC); (ii) smooth surface [3], which is contrastive to that of polycrystalline diamond; (iii) higher temperature stability as compared to that of DLC; (iv) unique optical and electrical properties owing to a large number of grain boundaries in the film [4]. Here, the grain boundaries exactly mean the interfaces between UNCDs and between an amorphous carbon matrix and UNCDs. It has been theoretically predicted that a large number of grain boundaries generate additional energy states between the bottom of the conduction band and the top of the valence band of diamond [5]. Experimentally, a large absorption coefficient caused by the direct optical bandgap with a value of 2.2 eV that might be due to grain boundaries has been reported [6]. As for the electrical properties, the *n*-type conduction of nitrogen-doped UNCD films is realized by the grain boundary conductions [7]. The effects of the grain boundaries on the film properties are hot topics specific to the UNCD films. The local atomic structure in the UNCD films significantly influences their physical properties. However, thus far, there have been a few researches on the local atomic structure [8, 9].

Raman spectroscopy has ever been widely utilized for the characterization of carbon-based materials [10, 11]. However, this technique has the following shortcomings for the structural measurement of mixed sp^2- and sp^3- bonded carbon materials. (i) There is the large difference in the

Raman cross-section between sp^2 and sp^3 bonds. The Raman cross-section for graphitic features can be up to 50 times compared to that of diamond [12]. This results in the extremely large sensitivity to the sp^2 bonds as compared to the sp^3 bonds [13]. (ii) Long range ordering factors in the materials indirectly contribute to the spectrum in Raman spectroscopy. Since the wavelength of an incident probe beam is on the order of micrometers, the sensitivity is strongly dependent on the wavelength of the incident beam and the crystallite size in materials. The detectable crystallite size has a critical value that depends on the wavelength of the incident beam. An ultraviolet incident beam is required for the detection of nanocrystalline diamond. From these shortcomings, for amorphous or nanocrystalline carbon wherein sp^2 and sp^3 bonds coexist, the qualification of the sp^2 and sp^3 bond fractions in their mixed materials is difficult to be reliably performed.

On the other hand, Near-edge X-ray absorption fine structure (NEXAFS) spectroscopy can overcome these problems. This spectroscopy probes the final-state wave function near the excited atom wherein transitions from the C 1s core level to the unoccupied states area are caused by X-ray photon absorption. The dominant interaction terms could be approximated to those between the localized bonds. Thus the NEXAFS spectrum can roughly be decomposed with the simple component spectra [14, 15].

NEXAFS spectroscopy has been successfully utilized for investigating the local bonding configurations within amorphous and nanocrystalline carbon. For amorphous carbon films, the spectrum has been decomposed into the components spectra originating from π^* and σ^* bonds, and the bonding configuration structure has been studied in detail [16, 17]. The sp^2 fraction estimation method that has been established in electron energy loss spectroscopy (EELS) is applicable to the NEXAFS measurement [18, 19]. For hydrogenated amorphous carbon [15, 20] and nitrogen-doped amorphous carbon films [21, 22], the bonding configurations of hydrogen and nitrogen atoms with carbon atoms have been investigated. For UNCD films, on the other hand, there have been a few researches thus far [9, 23].

As above-mentioned, the UNCD films have the complicated structure including the grain boundaries, which must have a significant role on the unique physical properties of the UNCD films. In this paper, we discuss on the atomic bonding configuration of UNCD/hydrogenated amorphous carbon (a-C:H) composite films by analyzing the NEXAFS spectra. Here we call our films "UNCD/a-C:H" films since UNCD crystallites are exactly surrounded by an a-C:H matrix. The peak decomposition of the measured spectrum revealed the specific bonding configuration to the UNCD/a-C:H films.

2. Experimental

UNCD/a-C:H films were deposited on Si substrates at a substrate-temperature (T_s) of 550°C and an ambient hydrogen pressure (P_{H2}) of 53.3 Pa by pulsed laser deposition (PLD) using a graphite target. The detailed conditions have been indicated in our previous paper [6]. For comparison, hydrogenated amorphous carbon (a-C:H) and nonhydrogenated amorphous carbon (a-C) films were prepared at T_s = room temperature (RT) in 53.3 Pa hydrogen and T_s = 550°C in vacuum, respectively. The UNCDs formation was confirmed by transmission electron microscopy (TEM). NEXAFS was performed on the UNCD/a-C:H, a-C:H, and a-C films with the same thickness of 100 nm. NEXAFS spectra were taken in a total electron yield mode by measuring the current from the sample to ground using synchrotron radiation at the beam line 12 of SAGA Light Source. Highly

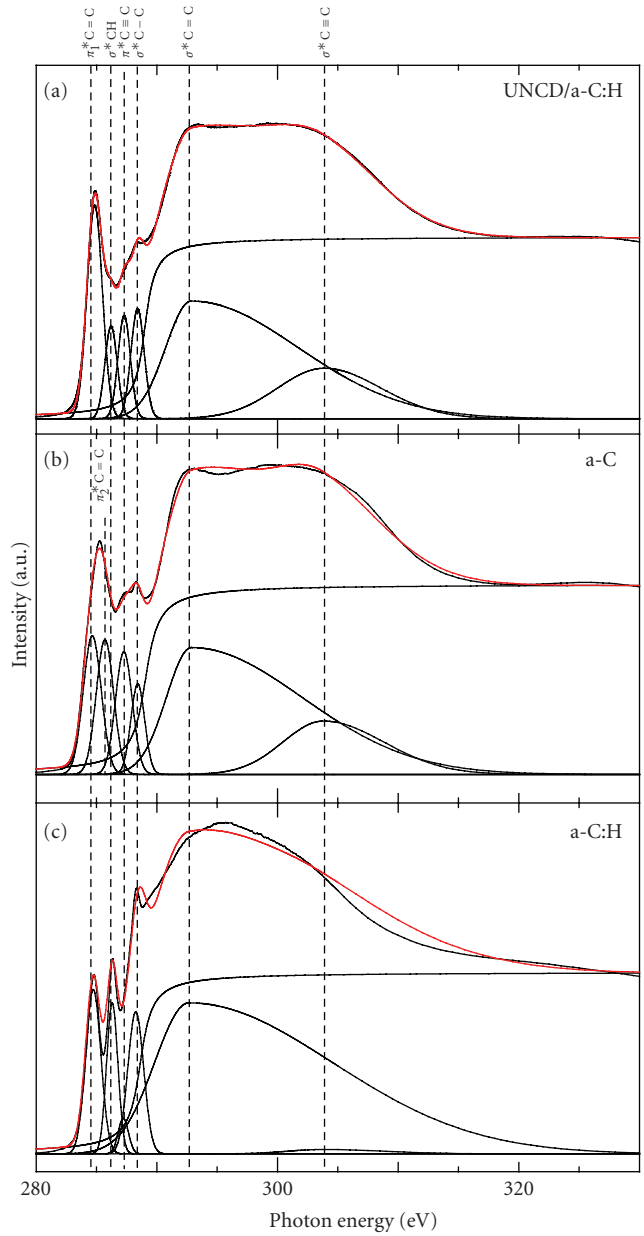

Figure 1: NEXAFS spectra, which are decomposed with an error-function step and Gaussians, of (a) UNCD/a-C:H film deposited at T_s = 550°C and P_{H2} = 53.3 Pa, (b) a-C film deposited at T_s = 550°C in vacuum, and (c) a-C:H film deposited at T_s = RT and P_{H2} = 53.3 Pa.

Table 1: Comparison of the peak positions and FWHMs of the decomposed component spectra of the UNCD/a-C:H films deposited at T_s = 550°C and P_{H2} = 53.3 Pa, a-C films deposited at T_s = 550°C in vacuum, a-C:H films deposited at T_s = RT and P_{H2} = 53.3 Pa in this study, and carbon films in previous reports.

	π_1*C=C (eV)	π_2*C=C (eV)	σ*C–H (eV)	π* C≡C (eV)	σ*C–C (eV)	σ*C=C (eV)	σ* C≡C (eV)
UNCD/a-C:H							
position	284.87		286.22	287.27	288.42	292.87	303.81
FWHM	1.48		1.50	1.30	1.30		
a-C							
position	284.65	285.70		287.27	288.42	292.87	303.81
FWHM	1.76	1.70		1.64	1.35		
a-C:H							
position	284.73		286.30	287.22	288.25	292.65	303.81
FWHM	1.48		1.10	1.00	1.55		
<Previous reports>							
position	285[a] [26] 284[b] [27] 284.6[b] [15]	286[b] [15]	287.5[a] [26] 287[b] [27]		289.3[c] [24]	292.7[d] [22]	

[a] UNCD/a-C:H, [b] a-C, [c] nanocrystalline diamond (NCD), and [d] amorphous nitrogenated carbon.

oriented pyrolytic graphite (HOPG) was used as a sample reference for the energy calibration.

3. Results and Discussion

The NEXAFS spectra of the UNCD/a-C:H film deposited at T_s = 550°C and P_{H2} = 53.3 Pa, a-C film deposited at T_s = 550°C in vacuum, and a-C:H film deposited at T_s = RT and P_{H2} = 53.3 Pa are shown in Figures 1(a), 1(b), and 1(c), respectively. These spectra were normalized in intensity at 330 eV. The spectra consist of two major peaks. One peak centered at 285 eV is due to the π^* bonding structure. The other peak positioned between 290 and 295 eV originates from the σ^* bonding structure. In the photon energy range between 285 and 290 eV, there is the obvious difference in the spectrum between the films. This implies that several peaks are superpositioned in this range.

The sp^2 fraction was estimated using the following equation:

$$f_{sp2} = \frac{I_{sam}^{\pi*}\, I_{ref}(\Delta E)}{I_{ref}^{\pi*}\, I_{sam}(\Delta E)}, \quad (1)$$

where $I_{sam}^{\pi*}$ and $I_{ref}^{\pi*}$ are the area of the π^* peak of the samples and reference HOPG, respectively, and $I_{sam}(\Delta E)$ and $I_{ref}(\Delta E)$ are the areas calculated under the remainder of each spectrum from 288.6 eV to 315 eV [24]. The sp^2 fractions were estimated to be 58%, 67%, and 40% for the UNCD/a-C:H, a-C, and a-C:H films, respectively. The a-C:H film deposited at T_s = RT shows the less sp^2 fraction as compared to the others deposited at T_s = 550°C. The sp^2 fraction of the UNCD/a-C:H film is smaller than that of a-C film, which might be mainly because of the existence of UNCD crystallites in the UNCD/a-C:H film.

In order to analyze the atomic bonding configuration in detail, the NEXAFS spectra were decomposed into component peaks. The decomposition was carried out based on the following assumptions. (a) The peak profile is predominantly responsible for the wave function; it cannot be dramatically changed between the similar kind of materials. (b) The peak profiles of the fitting component spectra were supposed to be approximately uniform between the samples. (c) The peak position was also almostly fixed because the bond length does not dramatically differ from those of similar materials.

The decomposed spectra of the UNCD/a-C:H, a-C, and a-C:H films are shown in Figures 1(a), 1(b), and 1(c), respectively. The integral spectrum resulting from the decomposed component spectra is shown in red solid line. The jump of the C K-edge at the ionization potential was fitted with an error-function step, and the subtracted spectra are decomposed into Gaussian peaks [14, 25]. The spectra were decomposed with the component spectra due to π^*C=C, σ^*C–H, π^*C≡C*, σ^*C–C, σ^*C=C, and σ^*C≡C. Here, the a-C film showed the obviously wide π^*C=C peak as compared to the other films. The π^*C=C peak of the a-C film was decomposed into two. This implies that the bonds with different bond lengths coexist in the a-C film. Table 1 shows the peak position and full width at half maximum (FWHM) of the decomposed component spectrum.

There are two obvious differences between the UNCD/a-C:H and a-C films. One is that the σ^*C≡C weakens and the σ^*C–H peak appears for the UNCD/a-C:H film. The σ^*C≡C bonds are partially replaced with the σ^*C–H bonds by hydrogenation. The other is that the UNCD/a-C:H shows the greater σ^*C–C peak than that of the a-C film. In the spectrum of the UNCD/a-C:H film, the σ^*C–C peak is relatively intense as compared to the σ^*C–H and π^*C≡C peaks. This is different from the other spectra. And the UNCD crystallites were confirmed by TEM only in the UNCD/a-C:H film. We believe that the relatively intense σ^*C–C peak is responsible for the existence of UNCDs.

In comparison with the a-C:H film, there are the following differences. (i) The UNCD/a-C:H film including the a-C film deposited at T_s = 550°C showed stronger π^*

and σ^* C≡C peaks than the a-C:H film deposited at T_s = RT. The C≡C bonds formation is enhanced at the elevated T_s. (ii) The a-C:H film showed intense σ^*C–H and σ^*C–C peaks instead of the π^* and σ^* C≡C peaks being weakened. Since the a-C:H film was deposited at T_s = RT, the intense σ^*C–H peak might result from a large amount of hydrogen in the film as compared to the UNCD/a-C:H film. At T_s = RT, the σ^*C–C bonds, instead of the C≡C bonds, were preferentially formed in the amorphous film.

4. Conclusion

The chemical bonding structure of the ultrananocrystalline diamond/hydrogenated amorphous carbon composite films prepared by pulsed laser deposition was investigated by near-edge X-ray absorption fine structure spectroscopy. The ultrananocrystalline diamond/hydrogenated amorphous carbon and amorphous carbon films deposited at the substrate-temperature of 550°C in 53.3 Pa hydrogen atmosphere and vacuum showed larger π^* and σ^*C≡C peaks than that of hydrogenated amorphous carbon film deposited at room substrate-temperature in 53.3 Pa hydrogen atmosphere. The ultrananocrystalline diamond/hydrogenated amorphous carbon composite films showed a greater σ^*C−C peak as compared to the amorphous carbon film. This is evidently responsible for the existance of ultrananocrystalline diamond crystallites in the film.

References

[1] T. Yoshitake, T. Hara, T. Fukugawa, et al., "Low-temperature growth of nanocrystalline diamond by reactive pulsed laser deposition under a hydrogen atmosphere," *Japanese Journal of Applied Physics, Part 2*, vol. 43, no. 2B, pp. L240–L242, 2004.

[2] T. Hara, T. Yoshitake, T. Fukugawa, et al., "Ultrananocrystalline diamond prepared by pulsed laser deposition," *Diamond and Related Materials*, vol. 15, no. 4–8, pp. 649–653, 2006.

[3] T. Hara, T. Yoshitake, T. Fukugawa, et al., "Nanocrystalline diamond film prepared by pulsed laser deposition in a hydrogen atmosphere," *Diamond and Related Materials*, vol. 13, no. 4–8, pp. 679–683, 2004.

[4] F. Cleri, P. Keblinski, L. Colombo, D. Wolf, and S. R. Phillpot, "On the electrical activity of sp^2-bonded grain boundaries in nanocrystalline diamond," *Europhysics Letters*, vol. 46, no. 5, pp. 671–677, 1999.

[5] P. Zapol, M. Sternberg, L. A. Curtis, T. Frauenheim, and D. M. Gruen, "Tight-binding molecular-dynamics simulation of impurities in ultrananocrystalline diamond grain boundaries," *Physical Review B*, vol. 65, no. 4, Article ID 045403, 11 pages, 2001.

[6] T. Yoshitake, A. Nagano, M. Itakura, N. Kuwano, T. Hara, and K. Nagayama, "Spectral absorption properties of ultrananocrystalline diamond/amorphous carbon composite thin films prepared by pulsed laser deposition," *Japanese Journal of Applied Physics, Part 2*, vol. 46, no. 36–40, pp. L936–L938, 2007.

[7] S. Bhattacharyya, O. Auciello, J. Birrell, et al., "Synthesis and characterization of highly-conducting nitrogen-doped ultrananocrystalline diamond films," *Applied Physics Letters*, vol. 79, no. 10, pp. 1441–1443, 2001.

[8] Y. C. Chen, X. Y. Zhong, A. R. Konicek, et al., "Synthesis and characterization of smooth ultrananocrystalline diamond films via low pressure bias-enhanced nucleation and growth," *Applied Physics Letters*, vol. 92, no. 13, Article ID 133113, 3 pages, 2008.

[9] C. Poppv, W. Kulisch, S. Boycheva, K. Yamamoto, G. Ceccone, and Y. Koga, "Structural investigation of nanocrystalline diamond/amorphous carbon composite films," *Diamond and Related Materials*, vol. 13, no. 11-12, pp. 2071–2075, 2004.

[10] Y. Hirose and Y. Terasawa, "Synthesis of diamond thin films by thermal CVD using organic compounds," *Japanese Journal of Applied Physics, Part 2*, vol. 25, no. 6, pp. L519–L521, 1986.

[11] M. S. Dresselhaus, M. A. Pimenta, P. C. Eklund, and G. Dresselhaus, "Raman scattering in fullerenes and related carbon-based materials," in *Raman Scattering in Materials Science*, W. H. Weber and R. Merlin, Eds., pp. 314–368, Springer, Berlin, Germany, 2000.

[12] D. S. Knight and W. B. White, "Characterization of diamond films by Raman spectroscopy," *Journal of Materials Research*, vol. 4, no. 2, pp. 385–393, 1989.

[13] F. L. Coffman, R. Cao, P. A. Pianetta, S. Kapoor, M. Kelly, and L. J. Terminello, "Near-edge X-Ray absorption of carbon materials for determining bond hybridization in mixed *sp2/sp3* bonded materials," *Applied Physics Letters*, vol. 69, no. 4, pp. 568–570, 1996.

[14] J. Stöhr, *NEXAFS Spectroscopy*, Springer, New York, NY, USA, 1992.

[15] J. Díaz, S. Anders, X. Zhou, E. J. Moler, S. A. Kellar, and Z. Hussain, "Analysis of the π^* and σ^* bands of the X-Ray absorption spectrum of amorphous carbon," *Physical Review B*, vol. 64, no. 12, Article ID 125204, 19 pages, 2001.

[16] J. Díaz, O. R. Monteiro, and Z. Hussain, "Structure of amorphous carbon from near-edge and extended X-Ray absorption spectroscopy," *Physical Review B*, vol. 76, no. 9, Article ID 094201, 12 pages, 2007.

[17] C. Lenardi, P. Piseri, V. Briois, C. E. Bottani, A. Li Bassi, and P. Milani, "Near-edge X-Ray absorption fine structure and Raman characterization of amorphous and nanostructured carbon films," *Journal of Applied Physics*, vol. 85, no. 10, pp. 7159–7167, 1999.

[18] K. Kanda, T. Kitagawa, Y. Shimizugawa, et al., "Characterization of hard diamond-like carbon films formed by Ar gas cluster ion beam-assisted fullerene deposition," *Japanese Journal of Applied Physics, Part 1*, vol. 41, no. 6B, pp. 4295–4298, 2002.

[19] J. Birrell, J. E. Gerbi, O. Auciello, J. M. Gibson, D. M. Gruen, and J. A. Carlisle, "Bonding structure in nitrogen doped ultrananocrystalline diamond," *Journal of Applied Physics*, vol. 93, no. 9, pp. 5606–5612, 2003.

[20] C. Lenardi, M. A. Baker, V. Briois, L. Nobili, P. Piseri, and W. Gissler, "Properties of amorphous a-CH(:N) films synthesized by direct ion beam deposition and plasma-assisted chemical vapour deposition," *Diamond and Related Materials*, vol. 8, no. 2–5, pp. 595–600, 1999.

[21] S. S. Roy, R. McCann, P. Papakonstantinou, et al., "Near edge X-Ray absorption fine structure study of aligned π-bonded carbon structures in nitrogenated ta-C films," *Journal of Applied Physics*, vol. 99, no. 4, Article ID 043511, 5 pages, 2006.

[22] S. Bhattacharyya, M. Lübbe, and F. Richter, "Near edge X-Ray absorption fine structure of thermally annealed amorphous nitrogenated carbon films," *Journal of Applied Physics*, vol. 88, no. 9, pp. 5043–5049, 2000.

[23] A. V. Sumant, D. S. Grierson, J. E. Gerbi, J. A. Carlisle, O. Auciello, and R. W. Carpick, "Surface chemistry and bonding configuration of ultrananocrystalline diamond surfaces and their effects on nanotribological properties," *Physical Review B*, vol. 76, no. 23, Article ID 235429, 11 pages, 2007.

[24] A. V. Sumant, P. U. P. A. Gilbert, D. S. Grierson, et al., "Surface composition, bonding, and morphology in the nucleation and growth of ultra-thin, high quality nanocrystalline diamond films," *Diamond and Related Materials*, vol. 16, no. 4–7, pp. 718–724, 2007.

[25] D. A. Outka and J. Stöhr, "Curve fitting analysis of near-edge core excitation spectra of free, adsorbed, and polymeric molecules," *The Journal of Chemical Physics*, vol. 88, no. 6, pp. 3539–3554, 1988.

[26] A. Hoffman, A. Heiman, H. P. Strunk, and S. H. Christiansen, "Microstructure and phase composition evolution of nanocrystalline carbon films: dependence on deposition temperature," *Journal of Applied Physics*, vol. 91, no. 5, pp. 3336–3344, 2002.

[27] T.-Y. Kim, C. S. Lee, Y. J. Lee, K.-R. Lee, K.-H. Chae, and K. H. Oh, "Reduction of the residual compressive stress of tetrahedral amorphous carbon film by Ar background gas during the filtered vacuum arc process," *Journal of Applied Physics*, vol. 101, no. 2, Article ID 023504, 5 pages, 2007.

Hindawi Publishing Corporation
Journal of Nanomaterials
Volume 2009, Article ID 621208, 7 pages
doi:10.1155/2009/621208

Research Article

Structural Transformation upon Nitrogen Doping of Ultrananocrystalline Diamond Films by Microwave Plasma CVD

Chien-Chung Teng,[1] Shin-Min Song,[2] Chien-Min Sung,[3] and Chhiu-Tsu Lin[1]

[1] *Department of Chemistry and Biochemistry, Northern Illinois University, Dekalb, IL 60115, USA*
[2] *Department o f Mechanical Engineering, Northern Illinois University, Dekalb, IL 60115, USA*
[3] *Diamond Technology Center, Kinik Company, No. 64, Chung-San Road, Ying-Ko, Taipei County 239, Taiwan*

Correspondence should be addressed to Chhiu-Tsu Lin, ctlin@niu.edu

Received 31 October 2008; Revised 16 January 2009; Accepted 11 February 2009

Recommended by Rakesh Joshi

The molecular properties and surface morphology of undoped and N-doped ultra-nanocrystalline diamond (UNCD) films deposited by microwave plasma CVD with addition of nitrogen are investigated with various spectroscopic techniques. The results of spatially resolved Raman scattering, ATR/FT-IR and XPS spectra show more amorphous and sp^2/sp^3 ratio characteristics in N-doped UNCD films. The surface morphology in AFM scans shows larger nanocrystalline diamond clusters in N-doped UNCD films. Incorporation of nitrogen into UNCD films has promoted an increase of amorphous sp^2-bonded carbons in the grain boundaries and the size of nanocrystalline diamond grains that are well correlated to the reported enhancement of conductivity and structural changes of UNCD films.

1. Introduction

Ultrananocrystalline diamond (UNCD) films have become very attractive materials for microelectronics applications since UNCD films with and without nitrogen doping have recently been shown to have mild n- and p-type semiconductor characteristics [1–8]. UNCD films are usually prepared by 1%CH_4/Ar microwave plasma CVD (MPCVD) [9]. Typically, UNCD films compose of 3∼8 nm polycrystalline nanodiamond grains, containing the mixtures of sp^2/sp^3-bonded carbon (trans-polyacetylene (t-PA) like, and graphite-like sp^2-bonded CH groups and sp^3-bonded CH_2 groups), with boundaries of ∼0.5 nm in width [3, 10–12].

Both theoretical calculations and experimental data showed that the preferential incorporation of nitrogen into the grain boundaries of N-doped UNCD films would form the larger clustering and disordering of graphite-like sp^2-bonded carbons [5, 6, 11]. Recently, diamond nanowires consisting of diamond core sheathed with sp^2-bonded carbon about 1 nm in thickness are observed in N-doped UNCD films with addition of 10% N_2 [11, 12].

Raman spectroscopy has been used to characterize molecular properties of UNCD films. On the other hand, IR spectroscopy is known as a complementary technique to Raman scattering for the studies of structural vibrations, such as C–H bonds stretching (2750 ∼ 3300 cm^{-1}) in sp^2/sp^3 carbon-based materials [2, 13]. In particular, attenuated total reflection Fourier transform infrared (ATR/FT-IR) spectroscopy is an effective technique for UNCD mirror-flat thin films samples due to the increasing optical path length by the multiple-reflected radiation in the total internal reflection element [14]. In this paper, we investigate and compare the spatial uniformity of molecular properties and surface morphology of MPCVD UNCD films processed with and without the addition of 20% nitrogen by using Raman and ATR/FT-IR spectroscopy as well as AFM for morphology images and XPS for chemical environment identifications. The correlations of spectroscopic results and the reported electrical conductivity and structural modifications are also discussed.

2. Experimental

2.1. UNCD Films by MPCVD. The UNCD films grown on Si with and without N_2 addition samples were prepared using 6

in CYRRANUS Innovative Plasma System (MPECVD, IPLAS GmbH) and provided by Dr. Gruen's group at Argonne National Lab, USA. The details of deposition parameters were the same as described in [12].

The UNCD films were deposited on a large 4 in Si wafer. The size, distribution, and uniformity of microwave plasma and substrate temperature can effectively affect the quality, property, and morphology of UNCD films. In particular, the UNCD film grown at the center of the Si wafer may be quite different from that at the edge. In this work, the UNCD film on Si wafer was divided into ten (10) intervals along the radius from the edge to the center, and labeled as #1 → #10.

2.2. Characterization Methods. Renishaw Raman Scattering Noodles System 2000, equipped with a Leica microscope and a HeNe red laser (632.8 nm) as an excitation source, was used to examine the molecular properties of UNCD films. X-ray photoelectron spectroscopy (Mg-K_α radiation of 1253.6 eV with a surface analysis depth of ~2 nm) was used to prove the binding states of carbon 1s core level in UNCD films without Ar^+ sputtering pretreatment. ATR/FT-IR spectrometer (PIKE, MIRacle Single Reflection Horizontal ATR Accessory equipped with 1.8 mm round ZnSe crystal IRE plate) was used to diagnose the molecular vibrations of UNCD films in mid-IR (650~4000 cm^{-1}) range recorded with 500 scans and 1 cm^{-1} resolution. Atomic force microscopy (AFM, Quesant Q-scope 350) measurements were scanned for the surface morphology of UNCD films.

3. Results and Discussions

3.1. Raman Spectra of UNCD Films. The spectroscopic measurement was monitored at each interval position. Figure 1 shows Raman spectra of undoped and N-doped UNCD films. The top two (green and pink) and the bottom two (brown and blue) are recorded at the edge and at the center of substrate, respectively. The assignment and interpretation of Raman spectra of undoped and N-doped UNCD films deposited from 1%CH_4/N_2/Ar MPCVD have been extensively discussed recently [4, 6, 11, 12]. The following spectral features are typically observed: (1) a broad band at 1332 cm^{-1} from nanodiamond crystallites, (2) the sp^2-bonded carbon features around 1340~1600 cm^{-1} (in particular at ~1350 cm^{-1} and ~1580 cm^{-1} for graphite D- & G-bands), and (3) The C–H vibration characteristics of short-chain conjugated t-PA in the grain boundaries at 1120 ~1190 cm^{-1} together with a weak peak at 1460 cm^{-1} and the overtone features at 2245~2810 cm^{-1} [3, 9, 10]. Moreover, the sp^3/sp^2 ratio in N-doped UNCD films normally decreases as compared to the undoped UNCD films [4].

In the bottom two spectra of Figure 1, the differences in the Raman spectra between undoped and N-doped UNCD films taken at the center position are similar to those observed by Polyakov et al. [7]. However, Polyakov et al. did not report the Raman spectra measured at the edge position for UNCD films. When the top two spectra (edge) and bottom two spectra (center) in Figure 1 are compared, the following observations are noted: (1) a large increase (or almost inverse) in the $I(G)/I(D)$ ratio, (2) the t-PA peak has transformed from a weak shoulder band at 1130 cm^{-1} to a well-defined peak at 1180 cm^{-1} and a large enhancement in overtone feature around 2270~2600 cm^{-1}, and (3) a stronger Raman intensity in 1100~1650 cm^{-1} for N-doped UNCD films is observed at the edge. These observed results strongly suggest that (1) the undoped UNCD films grown at the edge seem to contain a larger percentage of sp^2-bonded carbons due to the smaller nanodiamond crystallite clusters (see Figure 4 of AFM images) as compared to that at the center, and (2) the N-doped UNCD films show an increase in clustering and disordering of aromatic sp^2 (π)-bonded carbons in the grain boundaries [5, 6, 11]. However, one should also note that a large increase in Raman intensity of the top two spectra, such as the peak at 1540 cm^{-1}, may in part due to the higher scattering cross-section of sp^2 sites for visible Raman transitions.

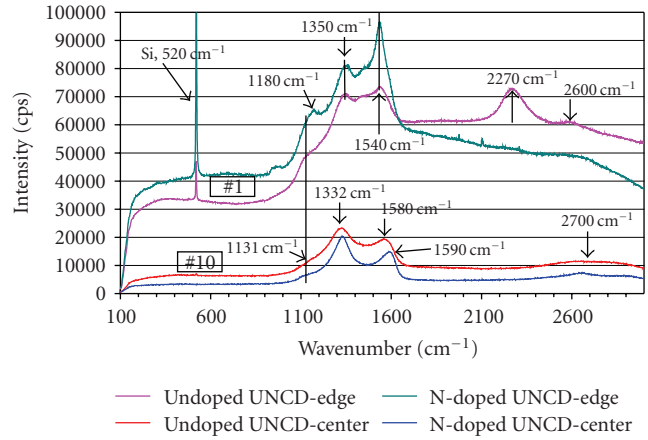

Figure 1: Raman spectra of UNCD films taken along the radius from the edge to the center position, labeled as #1 → #10.

The nanodiamond crystallinity for both undoped and N-doped UNCD films has shown to enhance as going from the edge to the center of substrate. This is evidenced by the observation of an increase in Raman intensity ratio (sp^3/sp^2) of diamond peak (shift from 1350 cm^{-1} to 1332 cm^{-1}) relative to graphite G-peak (shift from 1540 cm^{-1} to 1560~1590 cm^{-1}). On the other hand, the spectral peaks of t-PA seem to disappear gradually from the edge to the center substrate position, while only a small shoulder around 1130 cm^{-1} and a broad band around 2600~2700 cm^{-1} are observed, suggesting an improvement of sp^2-bonded carbons phases in the grain boundaries of UNCD films. Meanwhile, the broad spectral background is also greatly reduced.

The spatial variation in compositional changes of the UNCD films with and without N-doping as shown in Figure 1 is possibly resulted from the varying alpha parameter (appearing of crystal facets) due to the inhomogeneous of plasma density distribution from the perimeter of the plasma ball to the center of substrate that leads to different gas phase composition, varying substrate temperature and surface chemistry for diamond film growth [15, 16].

Figure 2 shows the intensity variation of spatially resolved Si Raman peak at 520 cm^{-1} taken along the radial

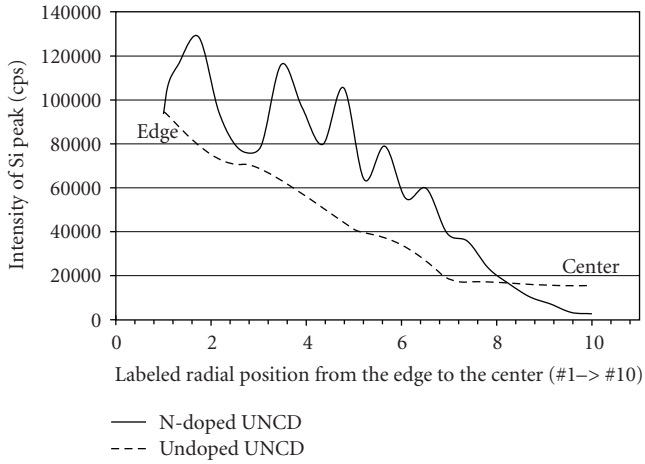

FIGURE 2: Intensity variation of spatially resolved Si Raman peak at 520 cm^{-1} of UNCD film from the edge to the center position of substrates.

position of substrate from the edge to the center, for both UNCD films with (solid) and without (dash) N_2 doping. For comparison, the Si peak of undoped UNCD film is normalized by referring to that of N-doped UNCD film at the edge position, labeled #1. The Si peak is observed because the thicknesses of UNCD films are thin enough for being penetrated through by the excitation laser beam. The penetration depth of the visible light at an excitation wavelength of 632.8 nm is about 1~2 μm [11]. Therefore, the change of Si peak intensity should inversely reflect the thickness uniformity of UNCD films over the Si substrate from the edge to the center. From the results illustrated in Figure 2, the films are thicker and smoother at the center (~1 μm) than those at the edge. The oscillation of Si peak intensity for N-doped UNCD film indicates its thickness fluctuation as going from the edge to the center positions, which is much larger than that of undoped UNCD film. The actual thickness profile of the films along the substrate position can be obtained by the calibration of Si Raman peak intensity.

3.2. ATR/FT-IR Spectra of UNCD Films. Figure 3(a) shows ATR/FT-IR absorption spectra of undoped (Blue) and N-doped (Red) UNCD films at the center position of substrate in the mid-IR range of 675~4000 cm^{-1}. The absorption of water (3500~3900 cm^{-1} and 1400~1800 cm^{-1}) and carbon dioxide (2350 cm^{-1}) is noticed in the spectra [17]. The C–C and C–H rocking characteristics of undoped UNCD films are observed between 800~1200 cm^{-1} and 600~900 cm^{-1}, respectively, in the spectrum (Blue) [13].

For this study, the focus is on the transformation of sp^3 to sp^2 CH vibrations upon nitrogen doping that are located in the spectral ranges of 2600 cm^2 to 3200 cm^2 as shown in Figures 3(b), 3(c). Both N-doped Figure 3(b) and undoped Figure 3(c) spectra are weak, broad, and featureless, so a detailed deconvolution technique of Gaussian fitting and baseline correction of ATR/FT-IR spectra is required to analyze the UNCD films at center of substrate. The tentative

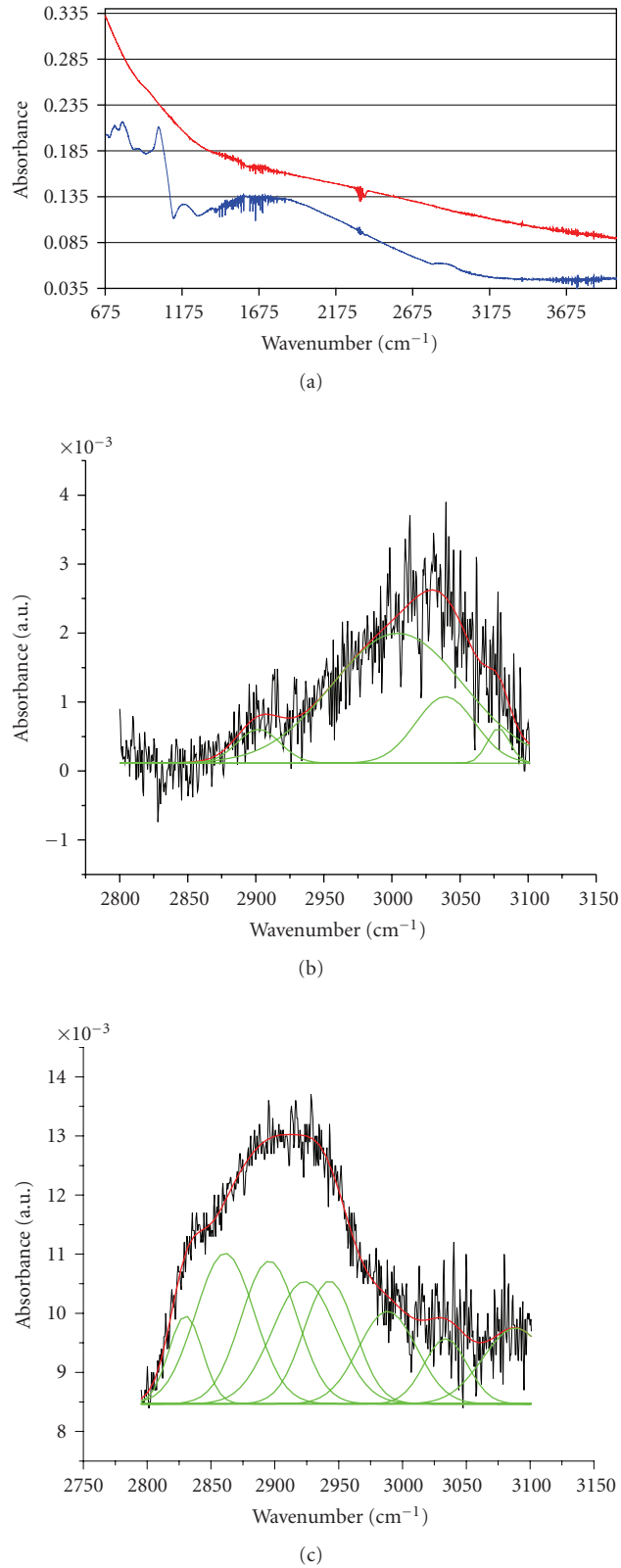

FIGURE 3: (a) ATR/FT-IR spectra of undoped (blue) and N-doped (red) UNCD films by MWCVD at the center position (labeled #10). (b), (c) Deconvolution (green) of ATR/FTIR spectra of N-doped (top) and undoped (bottom) UNCD films at the center position in CH vibrational region of 2600~3200 cm^{-1} after baseline correction and by Gaussian fitting (red).

Table 1: Spectral band assignment of CH_x stretching vibration modes of UNCD films at the center position, where minor peaks are shown in parenthesis.

Assignment in [13, 14, 16, 17]/(cm^{-1})	Assignment in experiments	
	N-doped UNCD films	Undoped UNCD films
sp^2-CH_2(sym.)/2980	3004	(2988)
sp^2-CH_2(asym.)/3080	3078	(3088)
sp^2-CH/3025	3039	(3033)
sp^3-CH/2900~2920	(2902)	2895
sp^3-CH_2(sym.)/2850	—	2861
sp^3-CH_2(asym.)/2920	—	2923

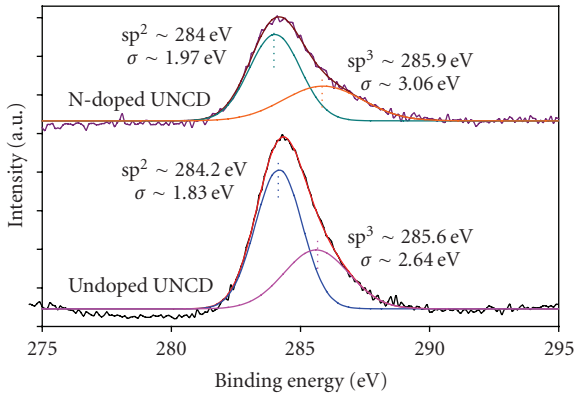

Figure 4: XPS C 1s spectra of undoped (bottom) and N-doped (top) UNCD films with Gauss fits of sp^2 & sp^3 peaks.

peak assignments are summarized in Table 1. The distinctive differences between N-doped and undoped UNCD films at center are in the spectral range of 2800~3100 cm^{-1}. The sp^2-CH_2 asymmetric and sp^2-CH stretching vibrations at 3078 cm^{-1} and 3039 cm^{-1} are observed in N-doped UNCD films [14, 18, 19]. The sp^3-CH and sp^3-CH_2 asymmetric stretching vibrations at 2895 cm^{-1} and 2923 cm^{-1} are shown for undoped UNCD films [13, 14, 18, 19]. We have also analyzed the ATR/FT-IR absorption spectra in the same spectral ranges as in Figure 3(b) for undoped and N-doped UNCD films at the edge position of substrate, and the results are quite similar to those at the center. The only difference is that the CH vibrational features of UNCD films are stronger and better defined at the center than those at the edge position. These results are in agreement with the Raman spectroscopic observations above that the incorporation of nitrogen into UNCD films would lead to the formation of sp^2-bonded carbons.

3.3. X-Ray Photoelectron Spectroscopy. In Figure 4, the XPS C 1s spectra of undoped and N-doped UNCD films at the center position (labeled #10) of the substrate are deconvoluted by Gaussian multiple peaks fitting into two main components with the binding energies (BEs) of 284.0~284.2 eV (for carbon sp^2 bonding) and 285.6~285.9 eV (for carbon sp^3 bonding). In N-doped UNCD films, the following XPS spectral features are observed: (1) sp^2 peak shifts to lower BE by 0.2 eV, (2) sp^3 peak shifts to higher BE by 0.3 eV, and (3) both sp^2 and sp^3 peaks are broadened as compared to the undoped UNCD films. The observed spectral broadening and shifts of C 1s BE have been suggested due to the interactions of C with N [20, 21]. The broadened C 1s peaks in XPS imply the increasing in the formation and disorderness of sp^2-bonded carbon phase as resulted from the incorporation of nitrogen into UNCD films that have also been illustrated in Raman and ATR/FT-IR spectra above.

3.4. AFM Morphology of UNCD Films. The AFM surface morphology of UNCD films was monitored for the spatial scanning areas with different film thickness. Figure 5 shows AFM surface morphology of undoped UNCD films (top four) and N-doped UNCD films (bottom four), both scanned at the edge (upper two labeled as (e)) and center (lower two labeled as (c)) positions of substrates.

In Figure 5 (top), the undoped UNCD films were formed by coalescence of coin-like diamond crystal clusters. In a smaller scanning area (or high resolution with a scale bar 100 nm) of Figure 5 (top, upper-right), the sizes of diamond crystal clusters at the edge are 433 nm and 391 nm as marked by red and blue arrows. In a larger scanning area (or low resolution with a scale bar 1 μm) of Figure 5 (top, lower-left), the sizes of diamond crystal clusters at the center are 817 nm, 701 nm, and 695 nm as marked by red, green, and blue arrows. In a smaller scanning area (or high resolution with a scale bar 100 nm) of Figure 5 (top, lower-right), the radius and central spacing of diamond crystal clusters at the center are about 471 nm and 527 nm as marked by green and blue arrows. Therefore, the sizes of diamond crystal clusters increase from 400~500 nm (top, upper-left, edge) to 700~800 nm (top, lower-left, center) along the radial position of substrate.

However in Figure 5 (bottom), the N-doped UNCD films were formed by coalescence of erythrocyte-like. In a larger scanning area (or low resolution with a scale bar 1 μm) of Figure 5 (bottom, left), the sizes of diamond crystal clusters at the edge are 794 nm, 915 nm, and 895 nm as marked by red, green, and blue arrows. The sizes of diamond crystal clusters at the center are 792 nm, 724 nm, and 781 nm as marked by red, green, and blue arrows. In a smaller scanning area (or high resolution with a scale bar 100 nm) of Figure 5 (bottom, upper), the widths of the thicker circumferential part of the erythrocyte-like diamond crystal cluster at the edge are about 348 nm and 189 nm as marked by green and blue arrows. Therefore, the diamond crystal clusters of 800~1000 nm in size over the substrate, both at the edge and center positions, are more uniform than that of undoped UNCD films over the entire substrate areas.

It is worthy of mentioning that the morphology of N-doped UNCD film seems to show a small opening in each diamond crystal cluster at the center as compared to that at the edge as shown in Figure 5 (bottom, lower-left). However, the similar morphology without those openings

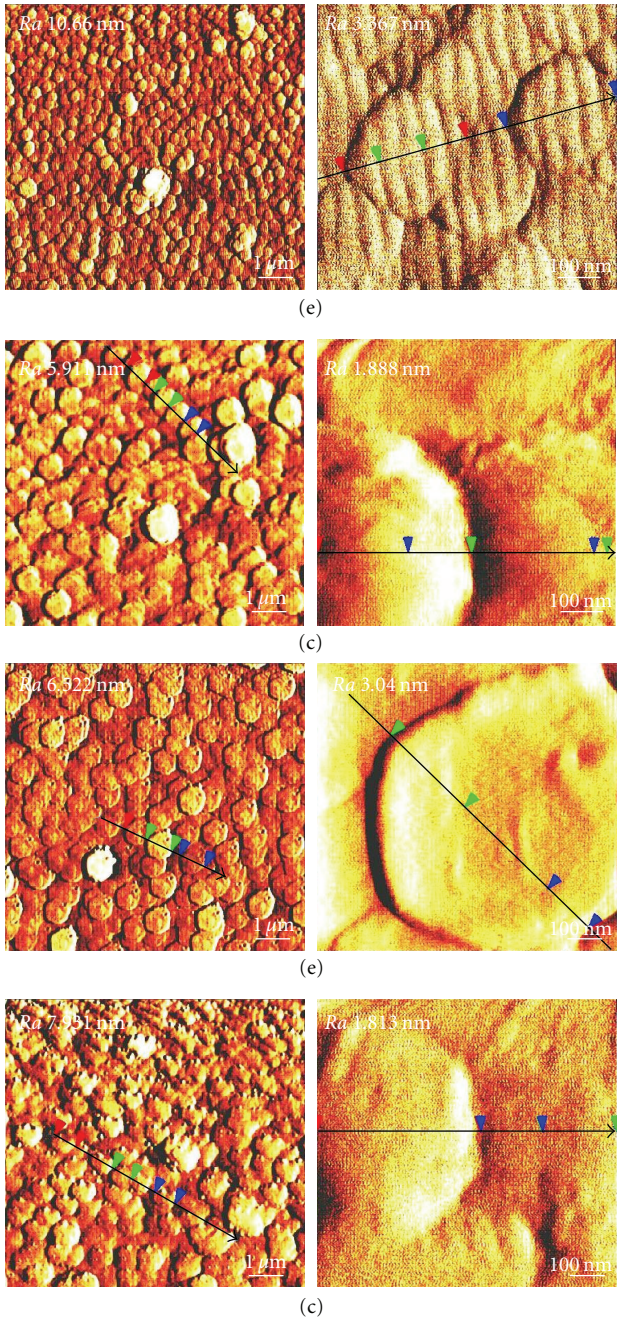

Figure 5: AFM surface morphology of undoped (top four) and N-doped (bottom four) UNCD films, scanned at edge (upper two labeled as (e)) and center (lower two labeled as (c)) in different areas.

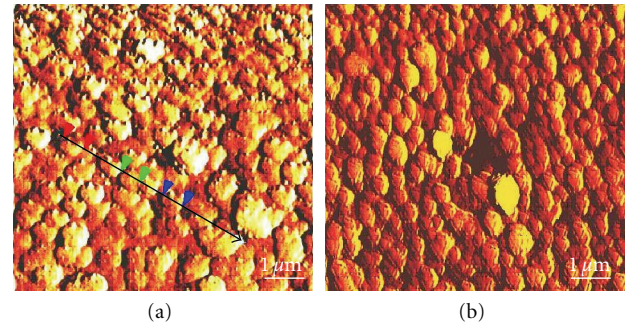

Figure 6: AFM surface morphology of N-doped UNCD films scanned at center by different probes (a) and (b).

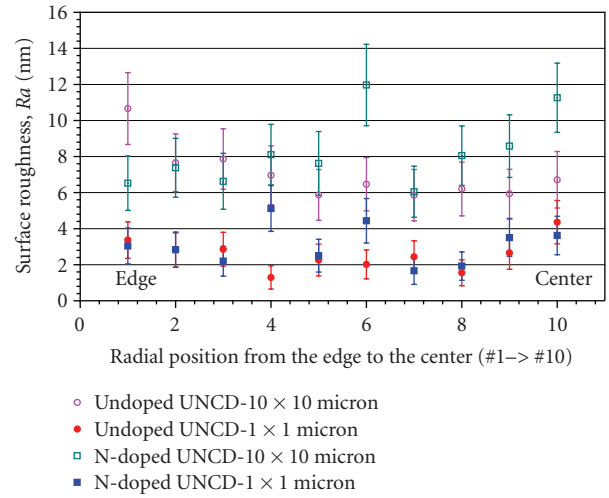

Figure 7: AFM mean surface roughness (*Ra*), with standard deviation error bar, of undoped and N-doped UNCD films scanned at different film areas.

was observed in the AFM image scanned by using a new probe as shown in Figure 6(b), where Figure 6(a) is the same AFM image as Figure 5 (bottom, lower-left). Therefore, those openings are the artifacts coming from the convolution of the tip and sample surface.

In a smaller scanning area (or a higher resolution with a scale bar 100 nm) of Figure 5 (top, right two), the surface morphology of each diamond crystal cluster of undoped UNCD films was revoluted from the periodically well-aligned ridges of 70~80 nm in spacing (two ridges of 155 nm as indicated by green arrows) at the edge (top, upper-right) into a ballic surface profile at the center (top, lower-right). On the other hand, in Figure 5 (bottom, right two), the surface morphology of each diamond crystal cluster of N-doped UNCD films was revoluted from a flat surface at the edge (bottom, upper-right) into a bump-like profile at the center (bottom, lower-right).

The observed AFM morphologies may suggest that when undoped UNCD films grow thicker at the center of substrate, the diamond crystal clusters as building blocks have transformed into a 3-dimensional growth, the larger diamond clusters have been grown from a plate-like at the edge into a ball-like at the center of substrate. However, as N-doped UNCD films become thicker, the diamond crystal clusters start with a similar size and then proceed to a preferentially growth in the direction perpendicular to the substrate surface.

Figure 7 shows the mean surface roughness (*Ra*) of the UNCD films for a larger scanning area, 10 μm × 10 μm (pink: undoped UNCD and light green: N-doped UNCD, hollow markers) and a smaller scanning area, 1 μm × 1 μm (red:

undoped UNCD and blue: N-doped UNCD, solid markers), from the edge (#1) to the center (#10) position as labeled in X-axis. The standard deviation error bars are indicated together with the mean *Ra* markers.

In pink markers, the *Ra* of the undoped UNCD film gradually decreases from 11 nm (edge, #1) to around 6 nm (center, #10), with the overall mean value of 7 nm (STED 1.4 nm). In red markers, on the other hand, the *Ra* of the undoped UNCD film displays a slight fluctuation with the overall mean *Ra* 2.5 nm (STED 0.9 nm).

This observation seems to associate with the numbers and size of diamond crystal clusters within the AFM scanning area. For example, in a ($1\,\mu$m $\times$ $1\,\mu$m) viewing area, the *Ra* (2.5 nm) is quite uniform within the area down to 1~4 diamond crystal clusters. For a larger viewing of undoped UNCD film, for example, $10\,\mu$m $\times$ $10\,\mu$m area covering about 100~400 diamond crystal clusters, the *Ra* increases up to 7 nm. The corresponding standard deviation of the mean *Ra* also increases in $10\,\mu$m $\times$ $10\,\mu$m area as compared to $1\,\mu$m $\times$ $1\,\mu$m area. The *Ra* is 6 nm at the center (#10) with a cluster size of 800 nm and the *Ra* = 11 nm in the edge (#1), while the cluster size is 500 nm, as shown in Figure 5 (top).

Similarly, in light green and blue markers, the overall mean *Ra* of the N-doped UNCD films, both in $10\,\mu$m $\times$ $10\,\mu$m and $1\,\mu$m $\times$ $1\,\mu$m scanning areas, is 8 nm (STED 1.8 nm) and 3 nm (STED 1.1 nm), respectively. But the *Ra* of N-doped UNCD films seems to fluctuate larger than that of undoped UNCD films, suggesting the formation of a larger diamond crystal cluster size for the N-doped UNCD films.

3.5. Effect of N-Doping on UNCD Films. Normally, UNCD films grown by MPCVD using CH_4 and Ar gas mixtures without the addition of N_2 gas should follow the C_2-based growth mechanism [7], where the grown UNCD films should compose of nanocrystalline diamond grains and a structurally disordered mixture of sp^3/sp^2-bonded carbons in the grain boundaries. Upon introducing nitrogen into UNCD films, the most energetically favorable sites should be at the grain boundaries, where the lone pair electrons in nitrogen can facilitate the transformation of tetrahedral coordinated sites of sp^3-like carbon configuration into a three-fold-coordinated site of sp^2-like carbon arrangement with a perturbed N-doped characteristic at the grain boundaries [6]. Thus, the incorporation of nitrogen into UNCD films could lead to an increase in amorphous sp^2-bonded (π-) carbon phase by the formation of conjugated networking of the chain-like sp^2 and sp^1 hybridized with N-doped structures together with aromatic carbon clusters in the grain boundaries as evidenced by the results of Raman, ATR/FT-IR, and XPS spectral investigations.

The sp^3 nanodiamond grains of undoped UNCD films are electrically inactive based on the theoretical tight-bonding calculations [8]. For N-doped UNCD film, the structural transformation has shown to lead to an increase of sp^2-carbon phase at the grain boundaries as illustrated in the spectroscopic investigation above that can give the n-type electrical conductivity as resulted from the increase in the electron delocalization of π-π^* transition states. This structural assessment is in agreement with the observed high conductivity (up to $150\,\Omega^{-1}\text{cm}^{-1}$) for the nitrogen containing UNCD films, via the enhanced sp^2-carbon phase about ~10% at the dense and connected grain boundaries [1, 21].

AFM surface morphology pictures of N-doped UNCD films in Figure 5 show larger nanocrystalline diamond clusters and more wrinkled surface than those of undoped UNCD films. The increase of the overall grain boundary volume and grain size in N-doped UNCD films measured at the center, and the edge positions of substrate could offer a possible film growth mechanism that the N-doped molecular species may reduce secondary nucleation rate by blocking potential sites for C_2 addition through the absorption of these N-doped molecules and thus enhance the growth of diamond crystals [4, 6].

4. Conclusions

The incorporation of nitrogen into UNCD films prepared by MPCVD using $CH_4/N_2/Ar$ gas mixtures has shown to lead to lower sp^3/sp^2-bonded carbon characteristic as evidenced in the spectral features of sp^2-bonded carbon phases in the grain boundaries of N-doped UNCD films. Higher amorphous and sp^2 carbon feature in thin UNCD film deposited at the edge position of substrate was observed. The increase in size of nanocrystalline diamond clusters leading to a larger fluctuation of surface roughness was also revealed by AFM surface morphology of N-doped UNCD films. The assessment of structural transformation of UNCD films upon nitrogen doping is in agreement with the previously proposed high electron transport via grain boundaries for N-doped UNCD films.

Acknowledgments

This work was supported by Kinik Company in Taiwan and Institute for Nano Science, Engineering and Technology of Northern Illinois University, USA. The authors would like to thank Dr. Dieter M. Gruen and Dr. Paola Bruno of Argonne National Lab for providing UNCD film samples and valuable discussions, and Dr. Haji-Shiekh for technical assistance on AFM measurement.

References

[1] O. A. Williams, T. Zimmermann, M. Kubovic, et al., "Electric properties and applications of ultrananocrystalline diamond," in *Synthesis, Properties and Applications of Ultrananocrystalline Diamond*, D. M. Gruen, O. A. Shenderova, and A. Ya. Vul', Eds., vol. 192 of *NATO Science Series II: Mathematics, Physics and Chemistry*, pp. 373–382, Springer, Berlin, Germany, 2005.

[2] D. M. Gruen, P. C. Redfern, D. A. Horner, P. Zapol, and L. A. Curtiss, "Theoretical studies on nanocrystalline diamond: nucleation by dicarbon and electronic structure of planar defects," *The Journal of Physical Chemistry B*, vol. 103, no. 26, pp. 5459–5467, 1999.

[3] X. Xiao, J. Birrell, J. E. Gerbi, O. Auciello, and J. A. Carlisle, "Low temperature growth of ultrananocrystalline diamond," *Journal of Applied Physics*, vol. 96, no. 4, pp. 2232–2239, 2004.

[4] Q. Chen, G. M. Swain, and D. M. Gruen, "Effects on N_2 in CH_4/Ar plasma on the microstructure and electrochemical properties of ultrananocrystalline diamond films," in *Proceedings of the 198th Electrochemistry Society Symposium on Electrochemistry of Carbon Materials*, vol. 34, pp. 73–82, Phoenix, Ariz, USA, October 2000.

[5] P. Zapol, M. Sternberg, L. A. Curtis, T. Frauenheim, and D. M. Gruen, "Tight-binding molecular-dynamics simulation of impurities in ultrananocrystalline diamond grain boundaries," *Physical Review B*, vol. 65, no. 4, Article ID 045403, 11 pages, 2002.

[6] J. Birrell, J. E. Gerbi, O. Auciello, J. M. Gibson, D. M. Gruen, and J. A. Carlisle, "Bonding structure in nitrogen doped ultrananocrystalline diamond," *Journal of Applied Physics*, vol. 93, no. 9, pp. 5606–5612, 2003.

[7] V. I. Polyakov, A. I. Rukovishnikov, N. M. Rossukanyi, et al., "Charge-based deep level transient spectroscopy of undoped and nitrogen-doped ultrananocrystalline diamond films," *Diamond and Related Materials*, vol. 12, no. 10-11, pp. 1776–1782, 2003.

[8] I. S. Beloborodov, P. Zapol, D. M. Gruen, and L. A. Curtiss, "Transport properties of *n*-type ultrananocrystalline diamond films," *Physical Review B*, vol. 74, no. 23, Article ID 235434, 5 pages, 2006.

[9] J. Birrell, J. E. Gerbi, O. Auciello, J. M. Gibson, J. Johnson, and J. A. Carlisle, "Interpretation of the Raman spectra of ultrananocrystalline diamond," *Diamond and Related Materials*, vol. 14, no. 1, pp. 86–92, 2005.

[10] D. M. Gruen, "Nanocrystalline diamond films," *Annual Review of Materials Science*, vol. 29, pp. 211–259, 1999.

[11] R. Arenal, G. Montagnac, P. Bruno, and D. M. Gruen, "Multiwavelength Raman spectroscopy of diamond nanowires present in *n*-type ultrananocrystalline films," *Physical Review B*, vol. 76, no. 24, Article ID 245316, 6 pages, 2007.

[12] R. Arenal, P. Bruno, D. J. Miller, M. Bleuel, J. Lal, and D. M. Gruen, "Diamond nanowires and the insulator-metal transition in ultrananocrystalline diamond films," *Physical Review B*, vol. 75, no. 19, Article ID 195431, 11 pages, 2007.

[13] N. Aggadi, C. Arnas, F. Benedic, et al., "Structural and chemical characterization of soot particles formed in $Ar/H_2/CH_4$ microwave discharges during nanocrystalline diamond film synthesis," *Diamond and Related Materials*, vol. 15, no. 4–8, pp. 908–912, 2006.

[14] P. John, D. K. Milne, I. C. Drummond, J. I. Wilson, M. G. Jubber, and J. A. Savage, "Attenuated total reflection infrared absorption in CVD diamond films," in *Diamond Optics V*, vol. 1759 of *Proceedings of SPIE*, pp. 209–217, San Diego, Calif, USA, July 1992.

[15] Private discussion with Dr. D. M. Gruen, Argonne National Lab, Argonne, Ill, USA.

[16] Y. Yokota, Y. Ando, K. Kobashi, T. Hirao, and K. Oura, "Morphology control of diamond films in the region of $\alpha = 1 - 1.5$ using a 60-kW microwave plasma CVD reactor," *Diamond and Related Materials*, vol. 12, no. 3–7, pp. 295–297, 2003.

[17] P. Thongnopkun and S. Ekgasit, "Attenuated total reflection Fourier transform infrared spectra of faceted diamonds," *Analytica Chimica Acta*, vol. 576, no. 1, pp. 130–135, 2006.

[18] K. M. McNamara, B. E. Williams, K. K. Gleason, and B. E. Scruggs, "Identification of defects and impurities in chemical-vapor-deposited diamond through infrared spectroscopy," *Journal of Applied Physics*, vol. 76, no. 4, pp. 2466–2472, 1994.

[19] E. J. Correa, Y. Wu, J.-G. Wen, R. Chandrasekharan, and M. A. Shannon, "Electrical conduction in undoped ultrananocrystalline diamond thin films and its dependence on chemical composition and crystalline structure," *Journal of Applied Physics*, vol. 102, no. 11, Article ID 113706, 10 pages, 2007.

[20] C. Ronning, H. Feldermann, R. Merk, H. Hofsäss, P. Reinke, and J.-U. Thiele, "Carbon nitride deposited using energetic species: a review on XPS studies," *Physical Review B*, vol. 58, no. 4, pp. 2207–2215, 1998.

[21] P. Achatz, O. A. Williams, P. Bruno, D. M. Gruen, J. A. Garrido, and M. Stutzmann, "Effect of nitrogen on the electronic properties of ultrananocrystalline diamond thin films grown on quartz and diamond substrates," *Physical Review B*, vol. 74, no. 15, Article ID 155429, 7 pages, 2006.

Hindawi Publishing Corporation
Journal of Nanomaterials
Volume 2009, Article ID 147204, 4 pages
doi:10.1155/2009/147204

Research Article

High-Resolution Magnetic Force Microscopy Using Carbon Nanotube Probes Fabricated Directly by Microwave Plasma-Enhanced Chemical Vapor Deposition

Kei Tanaka, Masamichi Yoshimura, and Kazuyuki Ueda

Nano High-Tech Research Center, Toyota Technological Institute, 2-12-1 Hisakata, Tempaku-ku, Nagoya 468-8511, Japan

Correspondence should be addressed to Masamichi Yoshimura, yoshi@toyota-ti.ac.jp

Received 27 September 2008; Accepted 31 October 2008

Recommended by Rakesh Joshi

Carbon nanotubes (CNTs) have been successfully grown on the tip apex of an atomic force microscopy (AFM) cantilever by microwave plasma-enhanced chemical vapor deposition (MPECVD). Both scanning electron microscopy (SEM) and transmission electron microscopy (TEM) observations reveal that the diameter of the CNTs is ~30 nm and the magnetic particles with diameter of ~20 nm, which was used as catalyst for the CNT growth, exist on the top. This CNT probe has been applied to magnetic force microscopy (MFM) on the ultrahigh-density magnetic recording media with 1200 kilo flux change per inch (kfci).

1. Introduction

Magnetic force microscopy (MFM) is a powerful tool to study the magnetic domain structure at a microscopic level, and is widely used in the research and development of magnetic nanodevices. Images with 50 nm resolution are routinely obtained when using commercial microscope and magnetic probes. However, higher resolution becomes more desired with increased recording density in future magnetic recording media. It is well known that the MFM resolution is limited by the tip geometry and height above the sample surface [1]. In particular, decrease in tip diameter is the most significant factor to improve the resolution.

Thus to achieve reedy tips, methods using focused ion beam (FIB) [2, 3] and the utilization of carbon nanotube (CNT) [4–9] have been proposed. There have been two methods for the fabrication of CNT-based MFM probes: a mechanical attachment of metal-filled CNTs or catalyst-attached CNTs under scanning electron microscopic (SEM) observation [7–9], and a coating of magnetic metal over a preattached CNT probe [4–6]. In the latter technique, Kuramochi et al. reported that the magnetic recording media up to 1100 kilo flux changes per inch (kfci) has been clearly observed with a resolution of approximately 10 nm [4]. However, the methods described above require time-consuming mechanical attachment or multiple processes, and seem inadequate for the large-scale production.

In a previous work, we successfully fabricated CNT probes for scanning tunneling microscopy (STM) by microwave plasma-enhanced chemical vapor deposition (MPECVD) [10]. This direct growth is quite suitable for the mass-scaled fabrication. It should be noted that the transmission electron microscopy (TEM) observation revealed the existence of magnetic particle as a catalyst on the top of each CNT. This feature can be applicable to MFM probes. Here, we have performed a growth of CNTs on the AFM cantilever made of Si, and have evaluated the resolution in the MFM measurement of longitudinal magnetic recording media with 1200 kfci.

2. Experimental

The growth of CNTs on the Si cantilever was performed by using an MPECVD system (CVD-CN-100, Ulvac Japan, Ltd., Kanagawa, Japan). A Co thin film 20 nm thick, as the catalyst, was coated on the Si cantilever ($k = 2.8$ N/m) by vacuum deposition. It was then set into the metal holder with seat mesh on the small hole in order to avoid the electric

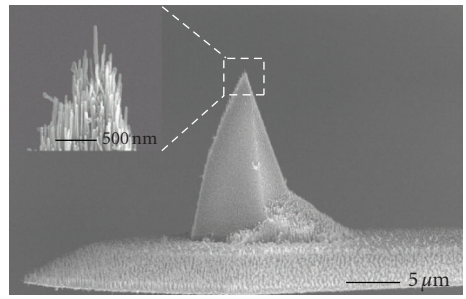

Figure 1: SEM image of CNTs on the tip apex of Si cantilever.

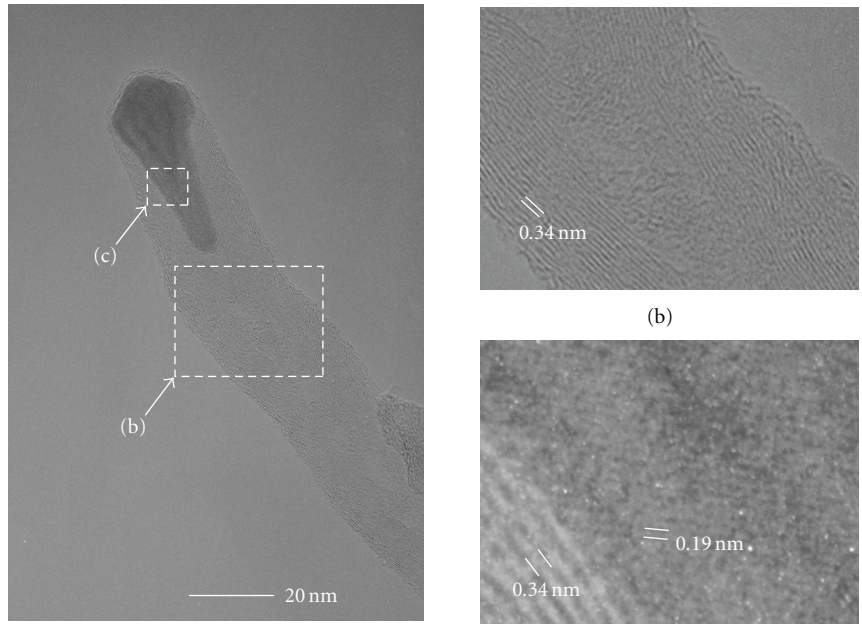

Figure 2: (a) TEM images of cocatalyzed CNT that scraped away from Si substrate. (b) and (c) are enlarged images of (a).

discharge and ion etching from the plasma [10], and was placed on the electrode in the MPECVD system. The mixed gas of CH_4 and H_2 was used for the CVD growth. The flow rate of H_2 and CH_4 was 80 and 20 sccm, respectively. Total gas pressure was set at 226 Pa. The microwave used was 2.45 GHz, 500 W and the growth time was 7 minutes. During the growth process, a voltage of 200 V was applied between the electrodes. Prior to the CNT growth, the cantilever was exposed to hydrogen plasma for cleaning as well as for activation of catalysts. During CVD process, no heater was used, but the substrate temperature was raised to approximately 600°C as measured by thermocouple. The morphology of tip apex after growth was observed by a field emission scanning electron microscope (FE-SEM, Hitachi, S4700). A high-resolution transmission electron microscope (TEM, JEOL, JEM2000EX) was used to determine the atomic structure of the CNT. In order to examine MFM performance, the surface of longitudinal magnetic recording media with densities of 600, 800, 1000, and 1200 kfci was observed by Nanoscpoe III (Digital Instruments, NY, USA) in air.

3. Results and Discussion

Figure 1 shows an SEM image of CNTs grown on the tip apex of the Si cantilever. The CNTs ~30 nm in diameter are clearly observed at the tip apex. Figure 2 shows a TEM image of a typical CNT similarly grown on an Si wafer. The catalyst particle exists on the top of CNT. This suggests that CNTs grew via the so-called tip growth mechanism [11]. The CNT shows tubular structure with graphene layers (lattice spacing of 0.34 nm) as resolved in the enlarged TEM image (Figure 2(b)). The magnified image of catalyst particle is shown in Figure 2(c), where the lattice of 0.19 nm is thoroughly observed. The lattice spacing corresponds to $Co_3C(103)$, suggesting that the CNT is grown with a nanoparticle of single crystalline Co_3C at its top [12].

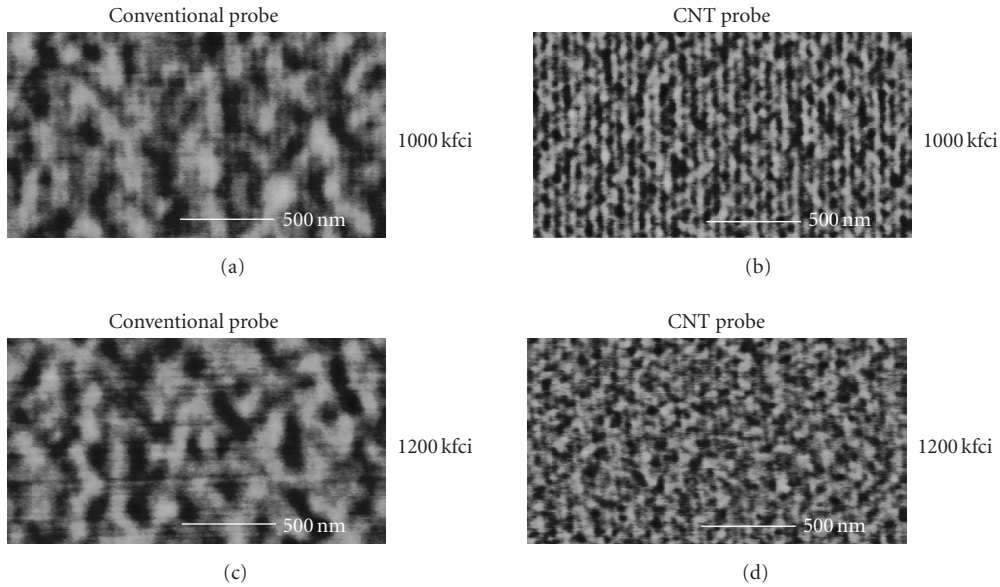

Figure 3: MFM images of ultrahigh-density recording media of 1000 and 1200 kfci using conventional and CNT probes. (a), (c) show MFM image obtained by conventional probe. (b), (d) show MFM image obtained by CNT probe. The recording densities were (a) and (b) 1000 kfci, (c) and (d) 1200 kfci.

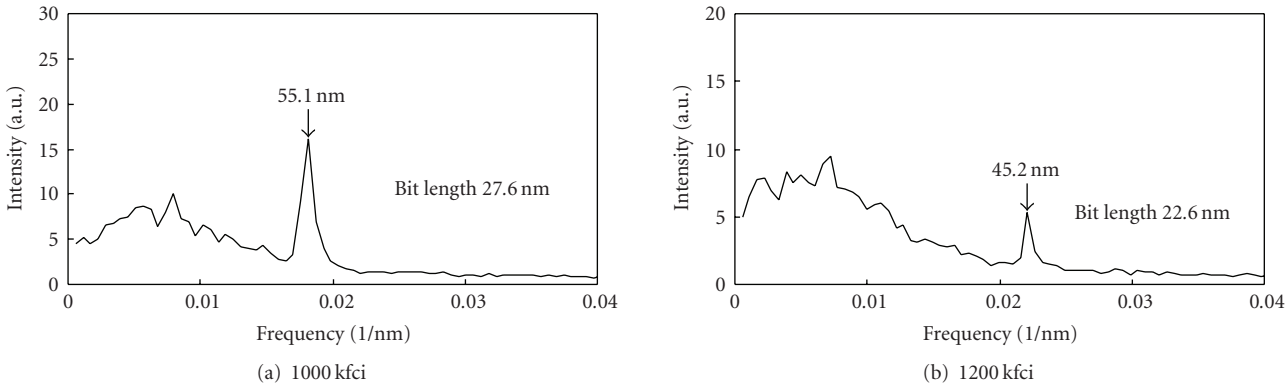

Figure 4: Power spectra corresponding to Figures 3(b) and 3(d). We have averaged twenty power spectra after performing a Fourier transform on a single-line profile obtained from MFM image.

Using this fabricated CNT probe and a conventional probe, MFM observation is performed for the ultrahigh-density recording media of 1000 and 1200 kfci, as shown in Figure 3. In the case of conventional probe, a stripe pattern of magnetic domain structure is observed up to 1000 kfci (Figure 3(a)), though the periodicity is not so clear. Irregular pattern appears appreciably comparable to the periodicity. In the case of 1200 kfci, no stripe magnetic domain structure is observed, as shown in Figure 3(c). In contrast, the recording period is clearly resolved up to 1000 kfci using the present CNT probe (Figure 3(b)), and even for 1200 kfci, the periodicity is visible on the background of the irregular pattern due to the limitation in the resolution and/or sample preparation.

Figure 4 shows the power spectra corresponding to Figures 3(b) and 3(d). These spectra were obtained by averaging twenty spectra after performing a Fourier transform of a single-line profile of the cross-section in MFM image. As shown in Figure 4, peaks at 55.1 and 45.2 nm are recognized (which is double the recoding bit size). These values are larger than the calculated values of 50.8 and 43.2 nm for 1000 and 1200 kfci. This may be due to inaccuracies in the recording process [2]. In these power spectra, strong background is observed on the low-frequency side. The inverse Fourier analysis indicates that this is caused by an irregular period due to disorder of the longitudinal recording. The writing of 1200 kfci is known to be difficult in the case of the longitudinal recording.

In order to estimate attainable resolution, we follow analysis procedure reported by Kuramochi et al. [4]. Figure 5(a) shows normalized intensity of power spectrum as a function of recording density. It is observed that the intensity decreases with increase in recording density. The intensity decreases with the increase of recording density.

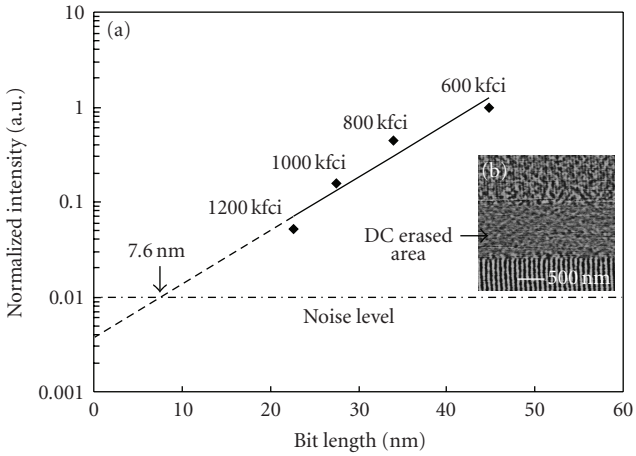

Figure 5: Plot of normalized intensity of power spectrum at the various recording bit length. The solid line was obtained by linear fitting for experimental plot. The sloping dashed line was obtained by extrapolating of solid line. The noise level was obtained from DC-erased area in (b) MFM image.

The attainable resolution in the observation of recording media is obtained from intersecting point of extrapolation of solid line and noise level line in Figure 5 [4]. The noise level was obtained from DC-erased area in MFM image as shown in Figure 5(b). The intersecting point corresponding to attainable resolution is around 7.6 nm, which is comparable to the value reported in [4]. It should be noted that in spite of the CNT-MFM probe by the present simple fabrication process without coating of magnetic materials, the resolution has been improved compared with conventional probe. The mass-scale fabrication of high-resolution CNT-MFM probes is also expected by this direct growth method.

4. Conclusion

In conclusion, we have successfully fabricated the CNT probes for MFM by direct growth using MPECVD. The CNTs of ~30 nm in diameter have been grown on the tip apex of Si cantilever, and the magnetic particle (~20 nm) is located at the end. The MFM observation using the fabricated CNT probe for magnetic recording media is demonstrated. The CNT probe resolves a stripe magnetic domain structure of ultrahigh-density recording media of 1000 and 1200 kfci much clearer than the conventional probe.

Acknowledgments

The authors would like to thank Dr. A. Okamoto (Toyota Central R&D Lab., Inc., Aichi, Japan) for his help in TEM observation, Dr. M. Oshiki (Fujitsu Ltd.) and Dr. I. Okamoto (Yamagata Fujitsu Ltd., Yamagata, Japan) for supplying the ultrahigh-density magnetic recording media. This work is supported by the "High-Tech Research Center" project for Private Universities: matching fund subsidy from the Ministry of Education, Culture, Sports, Science and Technology (MEXT), 2006–2008.

References

[1] D. Rugar, H. J. Mamin, P. Guethner, et al., "Magnetic force microscopy: general principles and application to longitudinal recording media," *Journal of Applied Physics*, vol. 68, no. 3, pp. 1169–1183, 1990.

[2] L. Gao, L. P. Yue, T. Yokota, et al., "Focused ion beam milled CoPt magnetic force microscopy tips for high resolution domain images," *IEEE Transactions on Magnetics*, vol. 40, no. 4, pp. 2194–2196, 2004.

[3] G. N. Phillips, M. Siekman, L. Abelmann, and J. C. Lodder, "High resolution magnetic force microscopy using focused ion beam modified tips," *Applied Physics Letters*, vol. 81, no. 5, pp. 865–867, 2002.

[4] H. Kuramochi, T. Uzumaki, M. Yasutake, A. Tanaka, H. Akinaga, and H. Yokoyama, "A magnetic force microscope using CoFe-coated carbon nanotube probes," *Nanotechnology*, vol. 16, no. 1, pp. 24–27, 2005.

[5] H. Kuramochi, H. Akinaga, Y. Semba, et al., "CoFe-coated carbon nanotube probes for magnetic force microscope," *Japanese Journal of Applied Physics*, vol. 44, no. 4A, part 1, pp. 2077–2080, 2005.

[6] Z. Deng, E. Yenilmez, J. Leu, et al., "Metal-coated carbon nanotube tips for magnetic force microscopy," *Applied Physics Letters*, vol. 85, no. 25, pp. 6263–6265, 2004.

[7] A. Winkler, T. Mühl, S. Menzel, et al., "Magnetic force microscopy sensors using iron-filled carbon nanotubes," *Journal of Applied Physics*, vol. 99, no. 10, Article ID 104905, 5 pages, 2006.

[8] T. Arie, H. Nishijima, S. Akita, and Y. Nakayama, "Carbon-nanotube probe equipped magnetic force microscope," *Journal of Vacuum Science and Technology B*, vol. 18, no. 1, pp. 104–106, 2000.

[9] N. Yoshida, M. Yasutake, T. Arie, S. Akita, and Y. Nakayama, "Quantitative analysis of the magnetic properties of metal-capped carbon nanotube probe," *Japanese Journal of Applied Physics*, vol. 41, no. 7B, pp. 5013–5016, 2002.

[10] K. Tanaka, M. Yoshimura, and K. Ueda, "Fabrication of carbon nanotube tips for scanning tunneling microscopy by direct growth using the microwave plasma-enhanced chemical vapor deposition," *e-Journal of Surface Science and Nanotechnology*, vol. 4, pp. 276–279, 2006.

[11] R. T. K. Baker, M. A. Barber, P. S. Harris, F. S. Feates, and R. J. Waite, "Nucleation and growth of carbon deposits from the nickel catalyzed decomposition of acetylene," *Journal of Catalysis*, vol. 26, no. 1, pp. 51–62, 1972.

[12] M. Tanemura, K. Iwata, K. Takahashi, et al., "Growth of aligned carbon nanotubes by plasma-enhanced chemical vapor deposition: optimization of growth parameters," *Journal of Applied Physics*, vol. 90, no. 3, pp. 1529–1533, 2001.

Hindawi Publishing Corporation
Journal of Nanomaterials
Volume 2009, Article ID 612549, 5 pages
doi:10.1155/2009/612549

Research Article

Direct Fabrication of Carbon Nanotubes STM Tips by Liquid Catalyst-Assisted Microwave Plasma-Enhanced Chemical Vapor Deposition

Fa-Kuei Tung, Masamichi Yoshimura, and Kazuyuki Ueda

Nano High-Tech Research Center, Toyota Technological Institute, 2-12-1 Hisakata, Tempaku-ku, Nagoya 468-8511, Japan

Correspondence should be addressed to Masamichi Yoshimura, yoshi@toyota-ti.ac.jp

Received 4 November 2008; Accepted 30 December 2008

Recommended by Rakesh Joshi

Direct and facile method to make carbon nanotube (CNT) tips for scanning tunneling microscopy (STM) is presented. Cobalt (Co) particles, as catalysts, are electrochemically deposited on the apex of tungsten (W) STM tip for CNT growth. It is found that the quantity of Co particles is well controlled by applied DC voltage, concentration of catalyst solution, and deposition time. Using optimum growth condition, CNTs are successfully synthesized on the tip apex by catalyst-assisted microwave-enhanced chemical vapor deposition (CA-MPECVD). A HOPG surface is clearly observed at an atomic scale using the present CNT-STM tip.

1. Introduction

Carbon nanotube (CNT) [1] has attracted considerable attention because of their unique and outstanding properties, such as chemical inertness, small tip radius, high-aspect ratio, mechanical robustness, and high electrical conductivity. It is demonstrated that the CNTs are suitable as tips of atomic force microscopy (AFM) [2–4] and scanning tunneling microscopy (STM) [5, 6]. Numerous methods to make CNTs tips have been reported: manual attachment of CNTs to the tip apex using an acrylic adhesive [2], electron beam-induced deposition (EBID) of amorphous carbon under SEM [7], and direct growth by a chemical vapor deposition (CVD) technique [8–12]. The CVD technique is most preferred in terms of mass production in the commercial use. Although a single CNT growth is ideally suitable for CNT tip in scanning probe microscopy (SPM), plenty of CNTs are grown over the whole tip by CVD because of the difficulty in positioning catalyst only at the tip apex [12].

In the present study, we have developed fast- and high-reproducible fabrication method of CNT-STM tips. Liquid catalyst-assisted microwave plasma-enhanced CVD (MPECVD) has been used to fabricate highly aligned CNTs onto the STM tip apex. Catalytic particles are deposited only at the STM tip apex by this electrochemical method. It is shown that the quantity of deposited catalyst particles is well controlled by tip immersion time, applied DC voltage, and solution concentration. Using an optimized growth condition, a single CNT is successfully grown onto the STM tip. The performance of the present CNT-STM tip is demonstrated by the observation of HOPG surface.

2. Experimental

A tungsten (W) tip (0.25 mm in diameter) for STM was prepared by electrochemical etching in KOH solution (2.5 N). The catalytic solution was prepared from pure water, liquid ammonia, 2-ethylhexanoicacid, and cobalt chloride with different concentrations as 10^{-1} M, 10^{-2} M, and 10^{-3} M. After a standstill for a couple of hours, the mixture separated into two gravity-stabilized layers, and the topmost transparent layer was used as catalytic solution. The prepared W tip was immersed in the solution by a micrometer-adjustable apparatus. The different DC voltages (2 V, 4 V, and 8 V) were applied on W tips to control the number of catalytic particles attached on the tip apex and to investigate aggregation of catalytic particles on W tips. The, thus, prepared catalyst covered W tip was placed into a

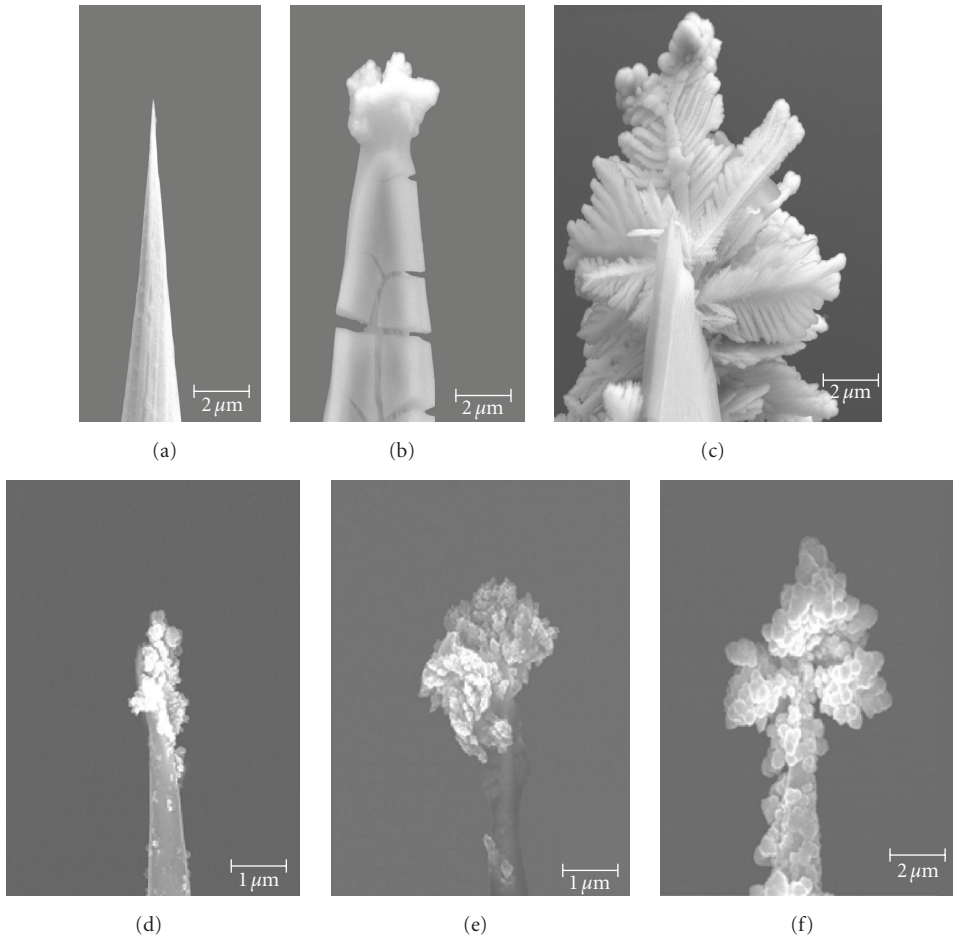

Figure 1: SEM pictures of catalyst-deposited tungsten tips with different electrochemical conditions. (a) voltage (4 V), concentration (0.05 M), and time (1 second); (b) 4 V, 0.05 M, and 5 seconds; (c) 8 V, 0.05 M, and 5 seconds; (d) 2 V, 0.001 M, and 5 seconds; (e) 2 V, 0.01 M, and 5 seconds; (d) 2 V, 0.1 M, and 5 seconds.

custom-made tip holder in a commercial MPECVD system (CVD-CN-100, Ulvac Japan, Kanagawa, Japan). The tip holder is designed so that the damage by plasma can be minimized during CNTs growth. Prior to CNTs growth, the tips were exposed to hydrogen plasma for the formation of catalyst particles as well as catalyst activation. Subsequently, methane and hydrogen gases were introduced for the CNTs growth. The mass flow ratio of CH_4:H_2 was kept at 1:4. The growth pressure was kept in the range of 1–5 torr. The microwave generator provides 2.45 GHz, 500 W microwave. The growth time was 5–10 minutes, and a DC voltage of −200 V was applied to the tip. The temperature of sample holder during CNTs growth process measured by a K-type thermocouple was about 700°C. Field emission scanning electron microscopy (FESEM, Hitachi S-4700) was used to characterize the attached quantity of catalyst particles and the CNTs structures. The crystallization of CNTs was studied by using a Raman spectroscopy (Jobin Yvon HR-800) with a 633 (1.96 eV) wavelength laser and the analysis power of 25 mW. STM measurement of a highly oriented pyrolytic graphite (HOPG) surface was performed in air to examine the capability of the CNTs tip prepared in this study.

3. Results and Discussion

The aggregation of catalyst particles on W tip apex was investigated with different deposition parameters. The effect of deposition time on catalytic aggregation was shown in Figure 1(a), and Figure 1(b) shows SEM images after deposition for 1 second (a) and 5 seconds (b), with immersing depth of 0.01 mm, solution concentration of 0.05 M, and applied voltage of 4 V. In Figure 1(a), no catalyst particles can be observed, while apparent catalyst particles are observed in Figure 1(b). This result suggests that the quantity of catalyst particles on the W tip increases with deposition time. Figures 1(b) and 1(c) show the effect of applied voltage on the aggregation of catalytic particles. Other deposition parameters are kept constant: immersing depth (0.01 mm), catalytic concentration (0.05 M), and deposited time (5 seconds). The effect of solution concentration on catalytic aggregation was shown in Figures 1(d)–1(f), where other deposition parameters are kept constant: immersing depth (0.1 mm), applied voltage (2 V), and deposited time (5 seconds). The higher solution concentration gives the larger size of deposited materials.

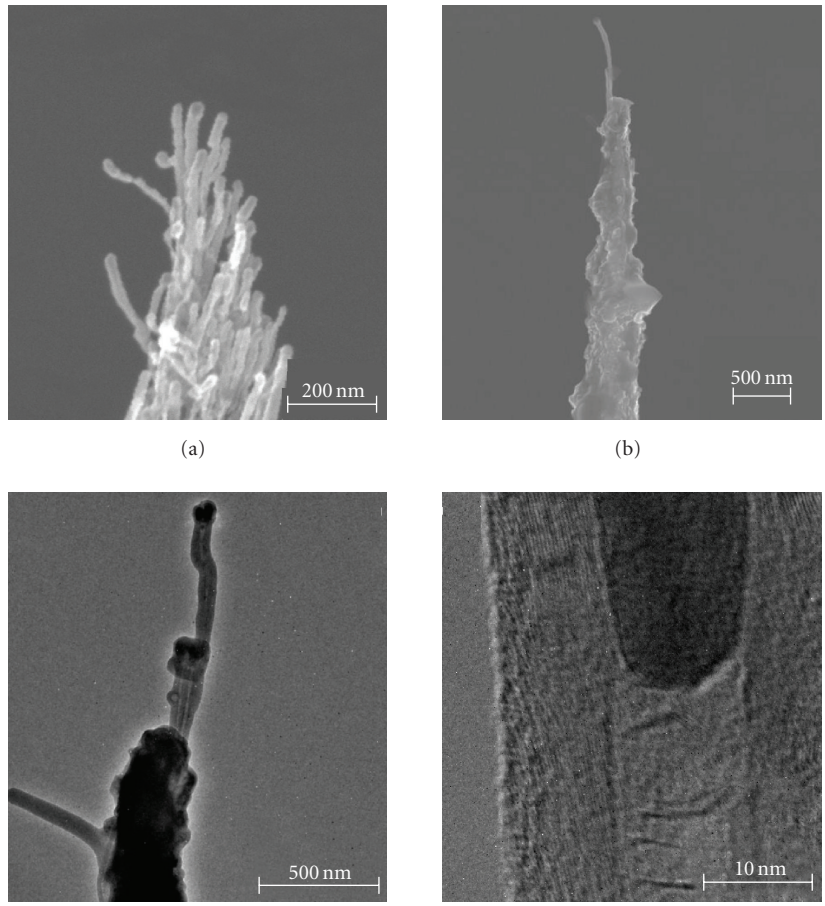

Figure 2: CNT-STM tips fabricated at the apex of tungsten tip. (a) CNTs from the deposited tip of Figure 1(d). (b) SEM and ((c), (d)) TEM images grown at the apex with optimum condition (2 V, 0.001 M, and ~0.5 seconds).

Co cationic particles in solvent are accelerated by electronic force forward to cathode W tip apex. The amount of deposited aggregation particles has been shown to be positively correlated with Co cationic particles flux, then, the relationship between relative parameters and cationic particles can be supposed as follows:

$$N \propto A * S * F,$$
$$F \propto M * V, \tag{1}$$

where N denotes amount of deposited aggregation particles, F denotes flux of ionic particles in unit time, A denotes deposition area perpendicular to flux, S denotes deposition time, M denotes concentration of ion solvent, and V denotes applied bias voltage.

Our experimental results can easily prove this postulate. Higher applied voltage enhances the more ionic particles passing through the unit area in a constant time, that is, the ion flux is increasing, further increases the deposited aggregation particles. In the same concentration and applied voltage, the ion flux in one unit area is in constant, then, the longer deposition time allows more ion particles to pass through the unit area, resulting in the increased deposition of particles. Finally, the higher concentration also increases the ion flux in unit area in a constant time and enhances the particles deposition. Those results allow us to assume that catalyst particles aggregation on W tip increases with the increasing of the ionic flux. Thus, the amount of deposited ionic particles can be controlled by the ion flux and depositing time. Besides, in this comparison, the over-deposition cases were employed in order to emphasize the relationship between different applied parameters and the catalyst particles aggregations on the W tip. Figure 2(a) shows CNTs grown on the catalyst-coated tungsten tip as shown in Figure 1(d) (2 V, 0.001 M, and 5 seconds). Numerous CNTs are grown on the tip surface, indicating the presence of catalytic Co particles using the present deposition technique.

Figure 2(b) shows low-magnification SEM image of the W tip apex which was deposited by applied bias 2 V, catalytic concentration (0.001 M), and deposited time (~ 0.5 second) after CNT growth. Figures 2(c) and 2(d) show TEM images of the same tip. The diameter and length are ~ 40 nm and ~ 900 nm, respectively. The number of graphen layers is 20–30. The CNT growth mechanism is clearly confirmed as tip growth [13], since the Co particle can be observed at the end

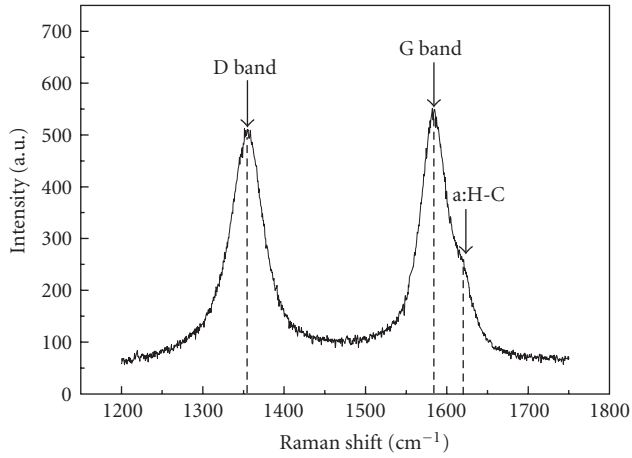

Figure 3: The baseline-treated Raman spectrum of CNT tip. In addition to graphite structure (G band) and disordered carbon structure (D band), amorphous hydrogenated carbon structure (a:H-C) is also observed.

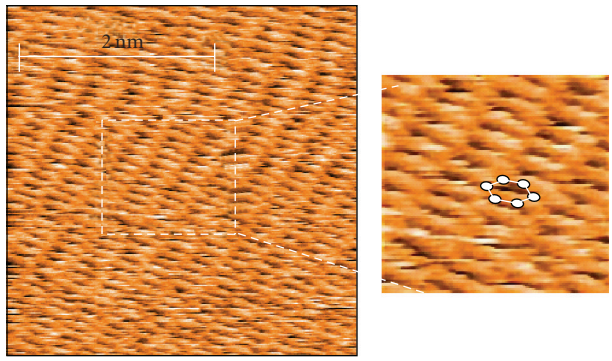

Figure 4: STM image of HOPG surface obtained at a bias voltage of 6.2 mV. Honeycomb structure is clearly resolved.

of the CNTs. As previously shown, the CNTs of 50 nm to 80 nm in diameter and ~800 nm to 1000 nm in length can be controlled by growth time [12].

Raman spectra are taken to spectroscopically characterize CNTs grown. The baseline-corrected Raman spectrum from CNT tip is shown in Figure 3. After using three Lorentzian peaks fitting, the center positions were specified at 1354 cm^{-1},1584 cm^{-1}, and 1619 cm^{-1}. The intensity rate and area rate were 5.47:5.84:1 and 12.51:11.03:1, respectively. The peak at 1354 cm^{-1} as defined as D band [14] and high D band shows the amorphous carbon structure similar with active coal. The peak at 1584 cm^{-1} is defined as G band, and it shows the graphite structure of CNTs similar with polycrystalline graphite powder [14]. The high intensity I_D/I_G ratio shows the structure defects of CNTs which were synthesized by catalyst pyrolytic method [15]. Peak at 1619 cm^{-1} comes from amorphous hydrogenated carbon (a:H-C) [16], which is regarded as one kind of defective graphite structure.

In order to demonstrate the capability of the CNT tip fabricated, highly-ordered pyrolytic graphite (HOPG) surface was observed as a test sample. Figure 4 shows the STM image taken in air. A honeycomb structure of graphite was obviously resolved at a bias voltage of 6.2 mV, although the image is somewhat distorted due to thermal drift. The corrugation measured is about 0.2 nm, comparable to the value obtained by conventional STM tips. However, we believe the present CNT tip becomes more powerful in the characterization of deep trench-like structures because of its high aspect ratio.

4. Conclusion

We have succeeded in fabricating the CNT-STM tip by liquid catalyst-assisted MPECVD. Highly aligned CNT with 30–50 nm in diameter was grown on STM tip apex, as revealed by FE-SEM and TEM. We have demonstrated the performance of those STM tips by obtaining atomic images of the HOPG surface. This method allows us to place and deposit catalytic particles in a controlled way on the tip apex much easier than conventional methods. It should be noted that even a single CNT-STM tip can be fabricated by our CA-MPECVD method.

Acknowledgments

This work is supported by "High-Tech Research Center" project for private universities: matching fund subsidy from Ministry of Education, Culture, Sports, Science and Technology (MEXT), 2006–2008. The authors also would like to thank Professor Hisanori Shinohara and Mr. Yuya Kamizono of Nagoya University for Raman spectra measurements, Professor Takayoshi Tanji, and Mr. Yutaka Ohira for TEM observation.

References

[1] S. Iijima, "Helical microtubules of graphitic carbon," *Nature*, vol. 354, no. 6348, pp. 56–58, 1991.

[2] H. Dai, J. H. Hafner, A. G. Rinzler, D. T. Colbert, and R. E. Smalley, "Nanotubes as nanoprobes in scanning probe microscopy," *Nature*, vol. 384, no. 6605, pp. 147–150, 1996.

[3] S. S. Wong, A. T. Woolley, T. W. Odom, et al., "Single-walled carbon nanotube probes for high-resolution nanostructure imaging," *Applied Physics Letters*, vol. 73, no. 23, pp. 3465–3467, 1998.

[4] J. H. Hafner, C.-L. Cheung, T. H. Oosterkamp, and C. M. Lieber, "High-yield assembly of individual single-walled carbon nanotube tips for scanning probe microscopies," *Journal of Physical Chemistry B*, vol. 105, no. 4, pp. 743–746, 2001.

[5] M. Ishikawa, M. Yoshimura, and K. Ueda, "A study of friction by carbon nanotube tip," *Applied Surface Science*, vol. 188, no. 3-4, pp. 456–459, 2002.

[6] M. Ishikawa, M. Yoshimura, and K. Ueda, "Carbon nanotube as a probe for friction force microscopy," *Physica B*, vol. 323, no. 1–4, pp. 184–186, 2002.

[7] H. Nishijima, S. Kamo, S. Akita, et al., "Carbon-nanotube tips for scanning probe microscopy: preparation by a controlled process and observation of deoxyribonucleic acid," *Applied Physics Letters*, vol. 74, no. 26, pp. 4061–4063, 1999.

[8] C. L. Cheung, J. H. Hafner, T. W. Odom, K. Kim, and C. M. Lieber, "Growth and fabrication with single-walled carbon nanotube probe microscopy tips," *Applied Physics Letters*, vol. 76, no. 21, pp. 3136–3138, 2000.

[9] E. Yenilmez, Q. Wang, R. J. Chen, D. Wang, and H. Dai, "Wafer scale production of carbon nanotube scanning probe tips for atomic force microscopy," *Applied Physics Letters*, vol. 80, no. 12, p. 2225, 2002.

[10] Y. Shingaya, T. Nakayama, and M. Aono, "Carbon nanotube tip for scanning tunneling microscopy," *Physica B*, vol. 323, no. 1–4, pp. 153–155, 2002.

[11] F. M. Pan, Y. B. Liu, Y. Chang, et al., "Selective growth of carbon nanotube on scanning probe tips by microwave plasma chemical vapor deposition," *Journal of Vacuum Science and Technology B*, vol. 22, no. 1, pp. 90–93, 2004.

[12] M. Yoshimua, S. Jo, and K. Ueda, "Fabrication of carbon nanostructure onto the apex of scanning tunneling microscopy probe by chemical vapor deposition," *Japanese Journal of Applied Physics*, vol. 42, no. 7B, pp. 4841–4843, 2003.

[13] S. B. Sinnott, R. Andrews, D. Qian, et al., "Model of carbon nanotube growth through chemical vapor deposition," *Chemical Physics Letters*, vol. 315, no. 1-2, pp. 25–30, 1999.

[14] M. J. Matthews, M. A. Pimenta, G. Dresselhaus, M. S. Dresselhaus, and M. Endo, "Origin of dispersive effects of the Raman D band in carbon materials," *Physical Review B*, vol. 59, no. 10, pp. R6585–R6588, 1999.

[15] P. Tan, S.-L. Zhang, K. T. Yue, et al., "Comparative Raman study of carbon nanotubes prepared by D.C. arc discharge and catalytic methods," *Journal of Raman Spectroscopy*, vol. 28, no. 5, pp. 369–372, 1997.

[16] N. Boutroy, Y. Pernel, J. M. Rius, et al., "Hydrogenated amorphous carbon film coating of PET bottles for gas diffusion barriers," *Diamond and Related Materials*, vol. 15, no. 4–8, pp. 921–927, 2006.

Hindawi Publishing Corporation
Journal of Nanomaterials
Volume 2009, Article ID 851290, 5 pages
doi:10.1155/2009/851290

Research Article

Growth of Pd-Filled Carbon Nanotubes on the Tip of Scanning Probe Microscopy

Tomokazu Sakamoto,[1] Chien-Chao Chiu,[1] Kei Tanaka,[2] Masamichi Yoshimura,[1] and Kazuyuki Ueda[1]

[1] *Nano High-Tech Research Center, Toyota Technological Institute, 2-12-1 Hisakata, Tempaku, Nagoya 468-8511, Japan*
[2] *Daido Bunseki Research Inc., 2-30 Daido-cho, Minato-ku, Nagoya 457-8545, Japan*

Correspondence should be addressed to Masamichi Yoshimura, yoshi@toyota-ti.ac.jp

Received 31 October 2008; Revised 14 February 2009; Accepted 16 February 2009

Recommended by Rakesh Joshi

We have synthesized Pd-filled carbon nanotubes (CNTs) oriented perpendicular to Si substrates using a microwave plasma-enhanced chemical vapor deposition (MPECVD) for the application of scanning probe microscopy (SPM) tip. Prior to the CVD growth, Al thin film (10 nm) was coated on the substrate as a buffer layer followed by depositing a 5 ~ 40 nm-thick Pd film as a catalyst. The diameter and areal density of CNTs grown depend largely on the initial Pd thickness. Scanning electron microscopy (SEM) and transmission electron microscopy (TEM) images clearly show that Pd is successfully encapsulated into the CNTs, probably leading to higher conductivity. Using optimum growth conditions, Pd-filled CNTs are successfully grown on the apex of the conventional SPM cantilever.

1. Introduction

Since their discovery by Iijima in 1991 [1], CNTs have successfully been synthesized via various techniques such as arc-discharged method [2], laser vaporization [3], and chemical vapor deposition (CVD) [4]. The advantage of CVD lies in the controlled fabrication at a designated position on the substrate using patterned catalysts. In particular, plasma-enhanced CVD (PECVD) technique can control the growth direction of individual CNTs by electric field [5–7].

Recently, growth of metal-filled CNTs (MF-CNTs) using Pd as the catalyst has been demonstrated and their structure and growth mechanism were investigated [8–10]. The anomalous feature of the Pd-filled CNTs was that they contained a Pd nanowire of the length of micrometer size and diameter of nanometer size. Since Pd has been shown to be particularly useful for achieving reliable ohmic contacts to single walled CNTs (SWCNTs) [11], the Pd-filled CNTs are expected to have higher conductivity from conventional hollow nanotubes. This property has potential application for the conductive tip in scanning probe microscopy (SPM). In addition, Pd, in nanosize and low dimension, is known to change its magnetism from paramagnetic to ferromagnetic [12, 13]. The feature extends the application to the tip of magnetic force microscopy (MFM).

Here, we demonstrate controlled synthesis of Pd-filled CNTs on the Si substrate as well as on the tip apex of SPM probes using the microwave plasma-enhanced chemical vapor deposition (MPECVD). The diameter and density of CNTs are well controlled by changing Pd thickness. The structure is investigated by field emission scanning electron microscopy (FE-SEM) and high-resolution transmission electron microscopy (TEM). Raman spectroscopy is also conducted to investigate the quality of the Pd-filled CNTs.

2. Experimental

Pd-filled CNTs were synthesized by using a MPECVD system (CVD-CN-100, Ulvac, Japan). A 10 nm-thick Al film was deposited as a buffer layer on a Si wafer or cantilever. This layer is known to prevent the formation of silicide as well as to support catalyst as nanoparticle [14, 15]. Then Pd of 5–40 nm was deposited as catalyst by sputtering. The mixture

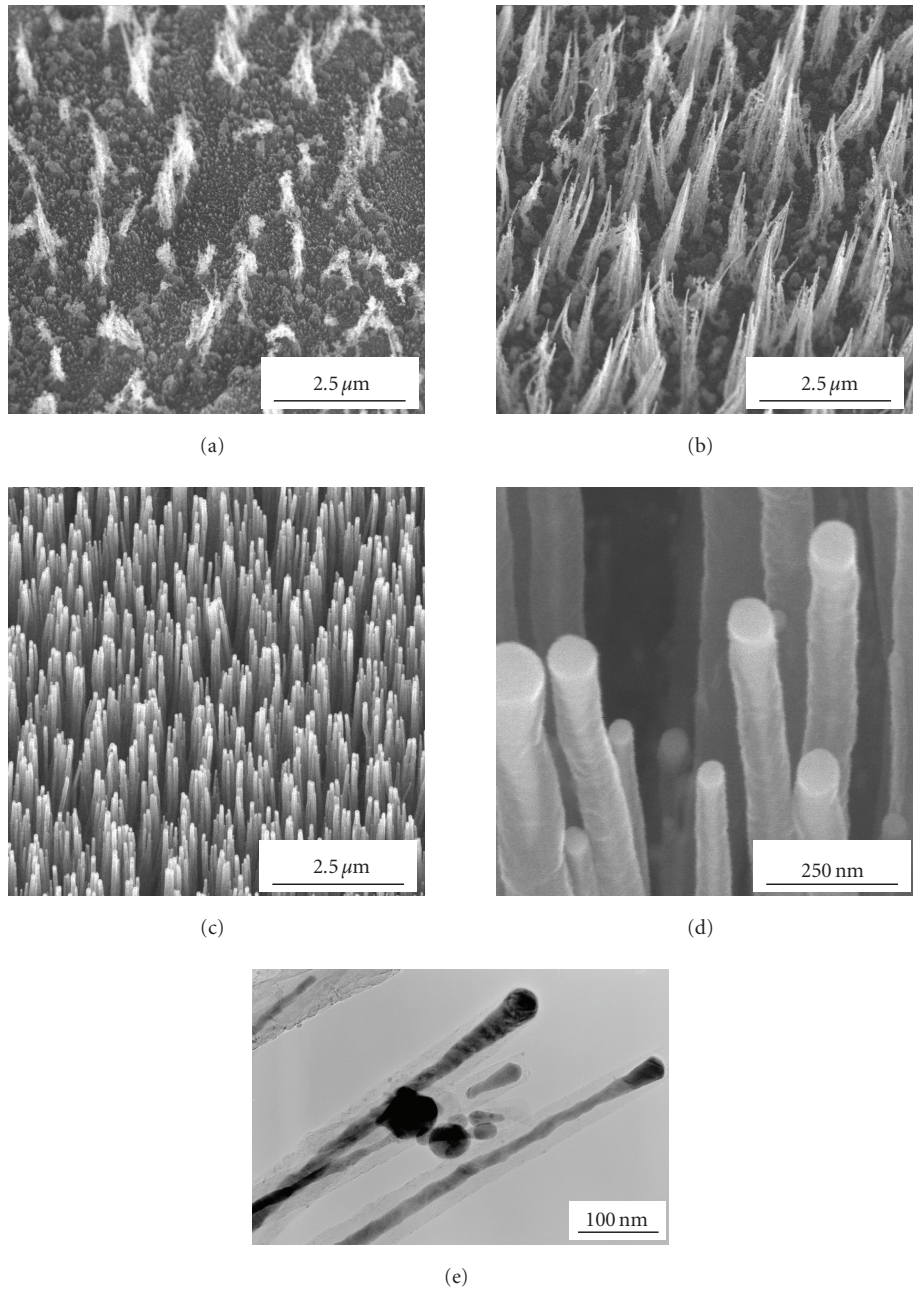

Figure 1: Low magnification SEM images of CNTs grown on (a) Pd (10 nm)/Al (10 nm)/Si, (b) Pd (20 nm)/Al (10 nm)/Si, (c) Pd (40 nm)/Al (10 nm)/Si. (d) High magnification SEM image of the CNTs in Figure 1(c). TEM image of the CNTs in Figure 1(a).

of H_2 and CH_4 gases was used for the CVD growth. The flow ratio of H_2 : CH_4 was kept constant at 80 : 20. Total gas pressure was set at 1.7 torr. We used a microwave of 2.45 GHz and 500 W, and the growth time was 10 minutes. During the growth process, a voltage of 200 V was applied between electrodes. Prior to the CNTs growth, the substrate was exposed to hydrogen plasma for 3 minutes to clean the substrate as well as to activate the catalyst. Hydrogen plasma has a significant annealing effect on Pd particles and alters their morphology [16]. The CNTs grown were characterized by field emission scanning electron microscopy (FE-SEM, Hitachi S4700), and high-resolution transmission electron microscopy (TEM, JEOL, JEM2000EX) and Raman spectroscopy (Jovin Yvon, LabRAM HR800) were carried out to determine the structure of the Pd-filled CNTs.

3. Results and Discussion

Figures 1(a)–1(c) show SEM images of CNTs grown with different Pd thickness. The CNTs grown on Pd (10 nm)/Al (10 nm)/Si, as shown in Figure 1(a), were sparsely distributed on the substrate. The CNTs on Pd (20 nm)/Al (10 nm)/Si

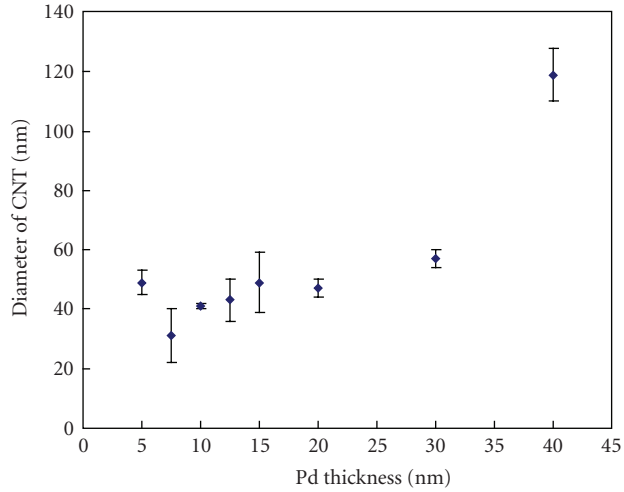

FIGURE 2: Pd thickness dependence of CNTs diameter. Hydrogen cleaning time is 3 minutes. Growth time is 10 minutes.

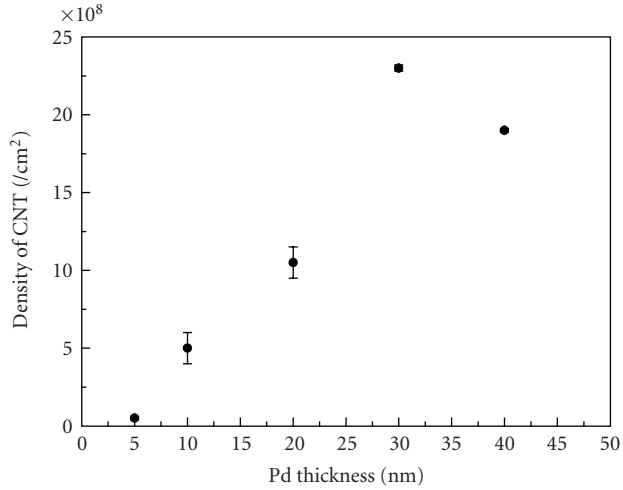

FIGURE 3: Pd thickness dependency of CNTs density. Hydrogen cleaning time is 3 minutes. Growth time is 10 minutes.

in Figure 1(b) and those on Pd (40 nm)/Al (10 nm)/Si in Figure 1(c) are well aligned and homogeneously distributed by the plasma sheath effect in MPECVD [16]. The diameter of the tip of CNTs is approximately 100 nm, and Pd-related materials are visible as bright contrast inside the CNTs as shown in Figure 1(d). TEM image in Figure 1(e) reveals that Pd is encapsulated inside the hollow of CNTs. In previous reports, metals were considered to be encapsulated in the hollows of CNTs by the capillary force [8, 9, 17–20].

Figure 2 shows the diameter of CNTs as a function of Pd thickness. The diameter of CNTs decreases with decreasing Pd thickness. It means that the diameter of CNTs depends on the size of catalyst particles. Thus the diameter can be reduced to approximately 30 nm at a Pd thickness of 7.5 nm. Figure 3 shows the density of CNTs as a function of Pd thickness. The curve was like mountain and it has a peak

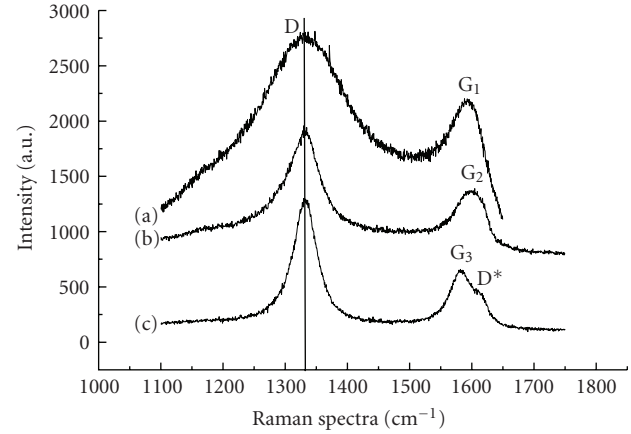

FIGURE 4: Raman spectra of CNTs grown on (a) Pd (1 nm)/Al (10 nm)/Si, (b) Pd (10 nm)/Al (10 nm)/Si, (c) Pd (30 nm)/Al (10 nm)/Si.

at a Pd thickness of 30 nm. CNTs were hardly grown on the substrates with Pd less than 5 nm because Pd was removed from the substrate by plasma etching in MPECVD.

Figure 4 shows Raman spectra of the CNTs grown in different conditions: (a) Pd (1 nm)/Al (10 nm)/Si, remote plasma, (b) Pd (10 nm)/Al (10 nm)/Si, MPECVD, (c) Pd (30 nm)/Al (10 nm)/Si, MPECVD. Remote plasma growth was done for comparison, where Pd was not encapsulated into the whole CNTs. Two strong peaks are observed in all the spectra at around 1350 cm^{-1} (D band) and around 1580–1600 cm^{-1} (G band). G peaks in Figures 4(b) and 4(c) are accompanied by an additional D* peak at around 1610–1620 cm^{-1}. The origin of D and D* bands have been attributed to disorder induced features such as defects generated in the graphitic planes of CNTs, due to curvature [21] and presence of amorphous carbon. On the other hand, G band is a characteristic of graphitic phase corresponding to in-plane vibration of C atoms, which indicates the presence of crystalline graphitic carbon in CNTs [22]. The appearance of D* band in Figures 4(b) and 4(c) agrees with the previous report, indicating the presence of Pd inside the whole CNTs [8, 23]. The intensity ratio of these two bands (I_D/I_G) [24] is considered as a parameter to characterize the quality of disorders in CNTs. The intensity ratios of I_D/I_G in all the spectra are larger than unity, indicating that the Pd-filled CNTs in the present study are multiwall CNTs (MWCNTs) with defective structure.

Since the growth condition is now optimized, growth of Pd-filled CNTs onto the SPM tip apex is performed. The Si cantilever was used as a specimen, and the same preparation, Al (10 nm) and Pd (10 nm) deposition, was conducted. The conditions are optimized to decrease the density of CNT and reduce the number or to produce only one CNT on the apex of tip. Figure 5(a) shows a low-magnified SEM image of CNTs grown on the cantilever surface. It is found that the pyramidal structure keeps its original shape after the growth. This is because the damage was minimized using a metal mesh for shielding from the direct impact of plasma

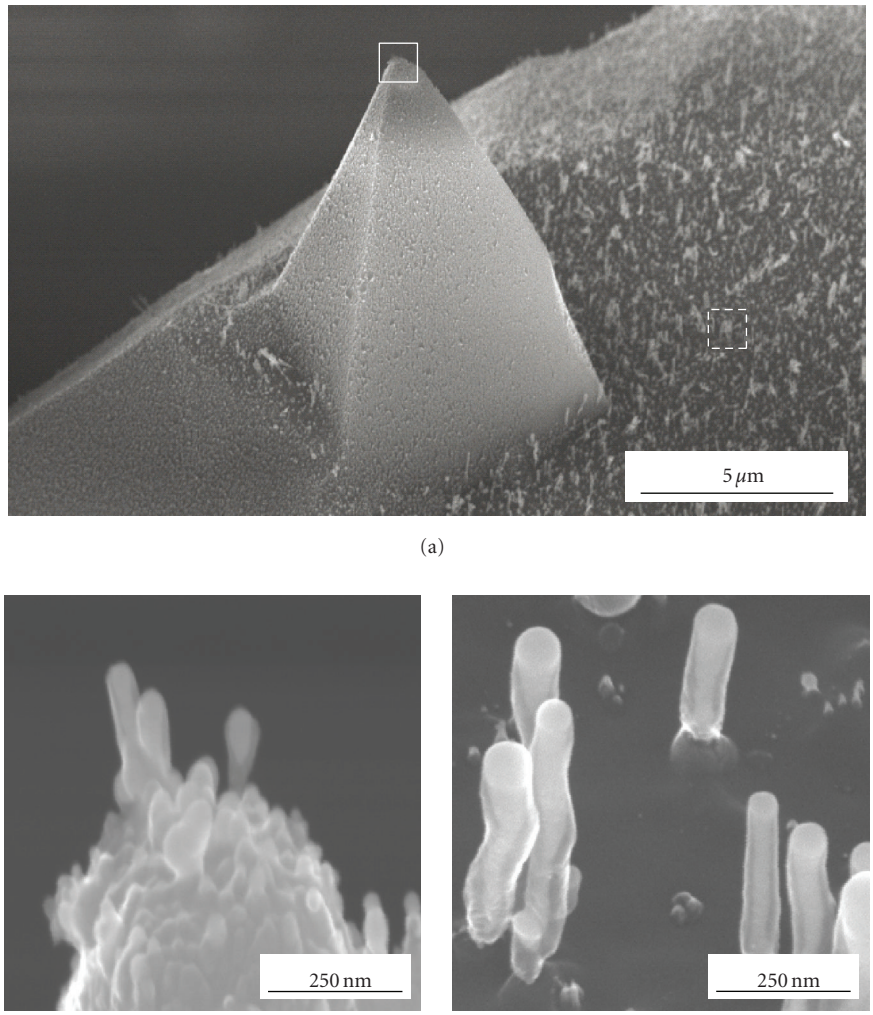

Figure 5: (a) Low magnification SEM image of CNTs grown on Al (10 nm)/Si cantilever. High magnification SEM images of CNTs at the tip apex (b) and of substrate Si (c).

ions [25]. The CNTs are well aligned and homogeneously distributed on the tip surface (Figure 5(b)) as well as on the cantilever surface (Figure 5(c)). The diameter of CNTs on the apex of tip is estimated to be approximately 50 nm. Figure 5(c) clearly reveals that Pd is encapsulated into the whole CNTs, as is on the Si wafer.

4. Conclusion

Pd-filled CNTs have been synthesized perpendicularly on Pd/Al (10 nm)/Si substrates by MPECVD. The diameter of CNTs has been controlled from 30 nm to 140 nm depending on the Pd thickness. Both SEM and TEM images clearly show that Pd is encapsulated into the whole CNTs. Raman revealed that Pd-filled CNTs were composed of poorly ordered graphene layers. Using optimum growth parameters, we have successfully fabricated Pd-filled CNTs on the apex of SPM probes.

Acknowledgments

The authors thank Professor H. Shinohara and Mr. Kamizono (Nagoya University) for the help of Raman measurements. This work is supported by the "Nano High-Tech Research Center" project for Private Universities: matching fund subsidy from the Ministry of Education, Culture, Sports, Science and Technology (MEXT).

References

[1] S. Iijima, "Helical microtubules of graphitic carbon," *Nature*, vol. 354, no. 6348, pp. 56–58, 1991.

[2] C. Guerret-Piécourt, Y. Le Bouar, A. Lolseau, and H. Pascard, "Relation between metal electronic structure and morphology of metal compounds inside carbon nanotubes," *Nature*, vol. 372, no. 6508, pp. 761–765, 1994.

[3] P. Castrucci, M. Scarselli, M. De Crescenzi, et al., "Effect of coiling on the electronic properties along single-wall carbon

nanotubes," *Applied Physics Letters*, vol. 85, no. 17, pp. 3857–3859, 2004.

[4] M. Tanemura, K. Iwata, K. Wakasugi, et al., "Synthesis of ni nanowire-encapsulated carbon nanotubes," *Japanese Journal of Applied Physics*, vol. 44, no. 4A, pp. 1577–1580, 2005.

[5] K. Tanaka, M. Yoshimura, and K. Ueda, "Fabrication of carbon nanotube tips for scanning tunneling microscopy by direct growth using the microwave plasma-enhanced chemical vapor deposition," *e-Journal of Surface Science and Nanotechnology*, vol. 4, pp. 276–279, 2006.

[6] M. Tanemura, K. Iwata, K. Takahashi, et al., "Growth of aligned carbon nanotubes by plasma-enhanced chemical vapor deposition: optimization of growth parameters," *Journal of Applied Physics*, vol. 90, no. 3, pp. 1529–1533, 2001.

[7] C.-C. Chiu, M. Yoshimura, and K. Ueda, "Regrowth of carbon nanotube array by microwave plasma-enhanced thermal chemical vapor deposition," *Japanese Journal of Applied Physics*, vol. 47, no. 4, pp. 1952–1955, 2008.

[8] Y. Hayashi, T. Tokunaga, S. Toh, W.-J. Moon, and K. Kaneko, "Synthesis and characterization of metal-filled carbon nanotubes by microwave plasma chemical vapor deposition," *Diamond and Related Materials*, vol. 14, no. 3–7, pp. 790–793, 2005.

[9] L. H. Chan, K. H. Hong, S. H. Lai, X. W. Liu, and H. C. Shih, "The formation and characterization of palladium nanowires in growing carbon nanotubes using microwave plasma-enhanced chemical vapor deposition," *Thin Solid Films*, vol. 423, no. 1, pp. 27–32, 2003.

[10] Q. Ngo, A. M. Cassell, V. Radmilovic, et al., "Palladium catalyzed formation of carbon nanofibers by plasma enhanced chemical vapor deposition," *Carbon*, vol. 45, no. 2, pp. 424–428, 2007.

[11] A. Javey, J. Guo, Q. Wang, M. Lundstrom, and H. Dai, "Ballistic carbon nanotube field-effect transistors," *Nature*, vol. 424, no. 6949, pp. 654–657, 2003.

[12] T. Shinohara, T. Sato, and T. Taniyama, "Surface ferromagnetism of Pd fine particles," *Physical Review Letters*, vol. 91, no. 19, Article ID 197201, 4 pages, 2003.

[13] A. Delin, E. Tosatti, and R. Weht, "Magnetism in atomic-size palladium contacts and nanowires," *Physical Review Letters*, vol. 92, no. 5, Article ID 057201, 4 pages, 2004.

[14] T. de los Arcos, F. Vonau, M. G. Gamier, et al., "Influence of iron-silicon interaction on the growth of carbon nanotubes produced by chemical vapor deposition," *Applied Physics Letters*, vol. 80, no. 13, pp. 2383–2385, 2002.

[15] Y. Zhao, K. Seko, and Y. Saito, "Effects of process parameters and substrate structures on growth of single-walled carbon nanotubes by catalytic decomposition of ethanol," *Japanese Journal of Applied Physics*, vol. 45, no. 8A, pp. 6508–6512, 2006.

[16] R. Hatakeyama and T. Kato, "Aligned carbon nanotube formation via radio-frequency magnetron plasma chemical vapor deposition," *Journal of Plasma and Fusion Research*, vol. 81, no. 9, pp. 653–659, 2005.

[17] S. Wei, W. P. Kang, W. H. Hofmeister, J. L. Davidson, Y. M. Wong, and J. H. Huang, "Effects of deposition and synthesis parameters on size, density, structure, and field emission properties of Pd-catalyzed carbon nanotubes synthesized by thermal chemical vapor deposition," *Journal of Vacuum Science and Technology B*, vol. 23, no. 2, pp. 793–799, 2005.

[18] R. K. Joshi, M. Yoshimura, C.-C. Chiu, F.-K. Tung, K. Ueda, and K. Tanaka, "Electrochemical growth of Pd for the synthesis of multiwall carbon nanotubes," *Journal of Physical Chemistry C*, vol. 112, no. 6, pp. 1857–1864, 2008.

[19] R. K. Joshi, M. Yoshimura, Y. Matsuura, K. Ueda, and K. Tanaka, "Electrochemically grown Pd nanoparticles used for synthesis of carbon nanotube by microwave plasma enhanced chemical vapor deposition," *Journal of Nanoscience and Nanotechnology*, vol. 7, no. 12, pp. 4272–4277, 2007.

[20] R. K. Joshi, M. Yoshimura, K. Tanaka, K. Ueda, A. Kumar, and N. Ramgir, "Synthesis of vertically aligned Pd_2Si nanowires in microwave plasma enhanced chemical vapor deposition system," *Journal of Physical Chemistry C*, vol. 112, no. 36, pp. 13901–13904, 2008.

[21] J. Kürti, V. Zólyomi, J. Koltai, F. Simon, R. Pfeiffer, and H. Kuzmany, "Curvature effects in the D^* band of small diameter carbon nanotubes," *Physica Status Solidi B*, vol. 244, no. 11, pp. 4261–4264, 2007.

[22] P. M. Ajayan, T. W. Ebbesen, T. Ichihashi, S. Iijima, K. Tanigaki, and H. Hiura, "Opening carbon nanotubes with oxygen and implications for filling," *Nature*, vol. 362, no. 6420, pp. 522–525, 1993.

[23] A. C. Ferrari and J. Robertson, "Interpretation of Raman spectra of disordered and amorphous carbon," *Physical Review B*, vol. 61, no. 20, pp. 14095–14107, 2000.

[24] C.-C. Chiu, C.-Y. Chen, N.-H. Tai, and C.-H. Tsai, "Growth of high-quality single-walled carbon nanotubes through the thermal chemical vapor deposition using co-sputtering Fe-Mo films as catalysts," *Surface and Coatings Technology*, vol. 200, no. 10, pp. 3199–3202, 2006.

[25] M. Yoshimura, S. Jo, and K. Ueda, "Fabrication of carbon nanostructure onto the apex of scanning tunneling microscopy probe by chemical vapor deposition," *Japanese Journal of Applied Physics*, vol. 42, no. 7B, pp. 4841–4843, 2003.

Hindawi Publishing Corporation
Journal of Nanomaterials
Volume 2009, Article ID 832327, 4 pages
doi:10.1155/2009/832327

Research Article

Poly(hydridocarbyne) as Highly Processable Insulating Polymer Precursor to Micro/Nanostructures and Graphite Conductors

Aaron M. Katzenmeyer,[1] Yavuz Bayam,[1,2] Logeeswaran VJ,[1] Michael W. Pitcher,[3] Yusuf Nur,[3] Semih Seyyidoğlu,[3] Levent K. Toppare,[3] A. Alec Talin,[4] Huilan Han,[5] Cristina E. Davis,[5] and M. Saif Islam[1]

[1] *Department of Electrical and Computer Engineering, University of California at Davis, Davis, CA 95616, USA*
[2] *Department of Computer Engineering, Sakarya University, 54178 Sakarya, Turkey*
[3] *Department of Chemistry, Middle East Technical University, 06531 Ankara, Turkey*
[4] *Sandia National Laboratories, Livermore, CA 94551, USA*
[5] *Department of Mechanical and Aeronautical Engineering, University of California at Davis, Davis, CA 95616, USA*

Correspondence should be addressed to M. Saif Islam, saif@ece.ucdavis.edu

Received 2 November 2008; Accepted 25 November 2008

Recommended by Rakesh Joshi

Carbon-based electronic materials have received much attention since the discovery and elucidation of the properties of the nanotube, fullerene allotropes, and conducting polymers. Amorphous carbon, graphite, graphene, and diamond have also been the topics of intensive research. In accordance with this interest, we herein provide the details of a novel and facile method for synthesis of poly(hydridocarbyne) (PHC), a preceramic carbon polymer reported to undergo a conversion to diamond-like carbon (DLC) upon pyrolysis and also provide electrical characterization after low-temperature processing and pyrolysis of this material. The results indicate that the strongly insulating polymer becomes notably conductive in bulk form upon heating and contains interspersed micro- and nanostructures, which are the subject of ongoing research.

1. Introduction

Poly(hydridocarbyne) (PHC) is an sp^3 hybridized random network carbon polymer, comprised of amonomeric unit containing one carbon-hydrogen and three carbon-carbon single bonds not unlike hydrogenated tetrahedral amorphous carbon (ta-C:H). Much interest was generated by the synthesis of this easily processable polymer and the report of its conversion to diamond and DLC by means of pyrolysis [1]. Diamond has been reported to have interesting electrical properties [2, 3] and applications in MEMS [4] and biology [5]. And ta-C:H has also been shown to be relevant to the electrical and biological communities in the form of protectivecoatings in magnetic disk memories [6] and a haemocompatible material [7], respectively.

2. Experimental

We developed a new method for the synthesis of PHC [8] which enables faster, easier production and makes this interesting material more accessible for research. The method of synthesis involves the electropolymerization of chloroform ($CHCl_3$) which proceeds as shown in Figure 1. UV/visible data collected during the polymerization are consistent with the production of a polycarbyne, namely PHC [1, 9, 10]. Transmission infrared spectroscopy shows no evidence of carbon-carbon double bonds, only carbon-carbon single bond and carbon-hydrogen stretches.

It was found that the polymer could be annealed at 100°C for processing as a liquid, in addition to the known method of suspending it in tetrahydrofuran (THF) or toluene, without the loss of its electrically insulating nature after cooling; an ~|8nA| current was measured via probe station at room temperature for |5V| bias. Semiconductor-like behavior was observed in the I(V) as the sample was heated.

Pyrolysis of the PHC polymer was performed under constant Ar flow at 1000°C for 24 hours in a Thermolyne tube furnace. A blackened bulk material was produced

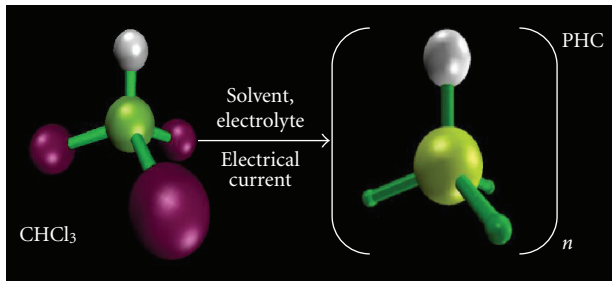

Figure 1: Electrolysis of chloroform ($CHCl_3$) in acetonitrile in the presence of tetrafluoroborate results in the production of PHC.

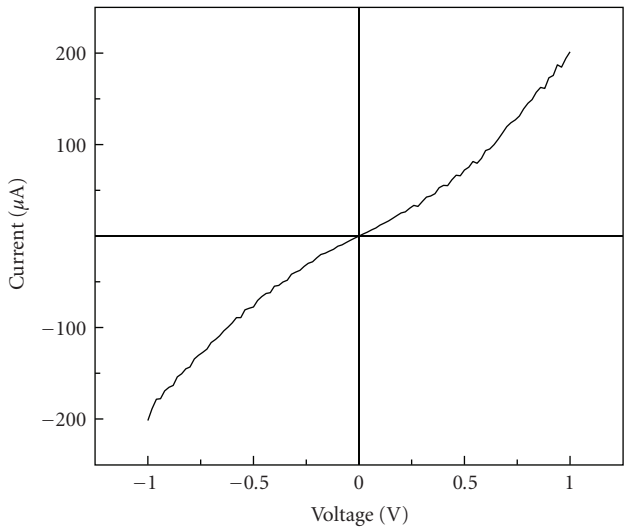

Figure 2: The I(V) plot for the pyrolyzed bulk shows a significant conductivity increase with respect to the annealed polymer.

which we electrically analyzed and characterized via Raman spectroscopy. This bulk material was probed (Figure 2) and found to be much more conductive than the annealed polymer despite exhibiting a nonlinear I(V) for $|V| > 0.25$. This increase in conductivity is rationalized by the formation of sp^2 hybridized carbon constituents during pyrolysis (see the following).

3. Raman Analysis

A vast body of work has been published on Raman spectroscopy of carbon-based materials and the techniques used to fit Raman spectra using their individual constituent peaks, and this remains an active area of research as certain peak contributions are still debated or are of unknown origin. Nonetheless, a literature review revealed well-developed theory, which enabled us to curve fit our sample to good approximation.

Figure 3 shows the spectrum of our material plotted against that ofknown diamond, the intended product of the pyrolysis. The two broadened features seen in our spectrum occur in the vicinity of the well-known D (disordered) and G (graphite) peaks that occur around 1360 cm^{-1} and

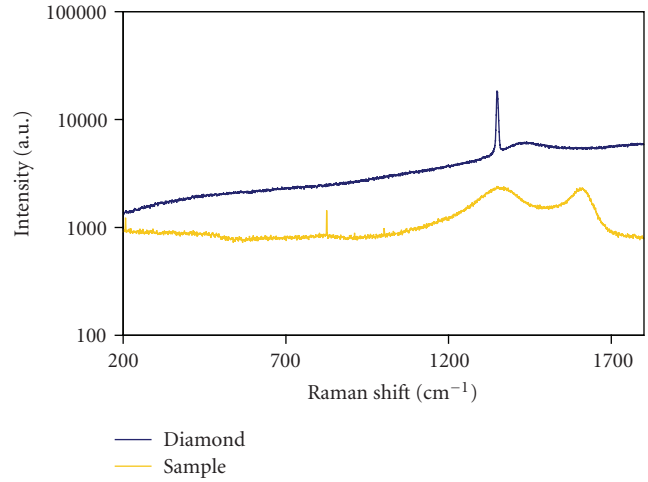

Figure 3: Raman spectra obtained for our pyrolyzed bulk sample and known diamond.

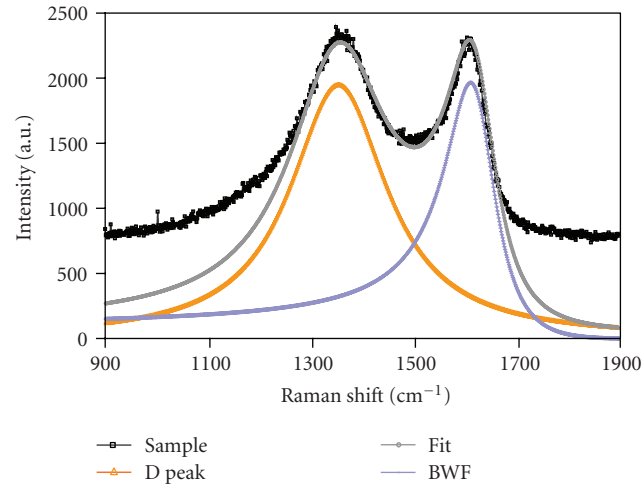

Figure 4: The Raman spectrum was fit using a Lorentzian function for the D peak. The other feature resulting from the combination of the G and D' peaks can be represented by a BWF function.

1560 cm^{-1}, respectively, [11] in graphitic carbon materials and are particularly characteristic of microcrystalline graphite [12].

To elucidate this, we followed the convention of curve fitting the spectrum using a Lorentzian function for the D peak and a Breit-Wigner-Fano (BWF) function for the contribution near the G peak (Figure 4). The motivation for the use of the BWF function lies in its ability to represent the merging of the G and D' peaks, a phenomenon which occurs when the crystalline domains of a graphitic material are sufficiently small [13, 14]. Due to the close fitting of our spectra using this methodology, we find the majority of the pyrolysis product is small-crystalline graphite, which explains the notable increase in conductivity after burning the PHC.

SEM did however reveal micro and nanostructures that were clearly morphologically distinct from the majority

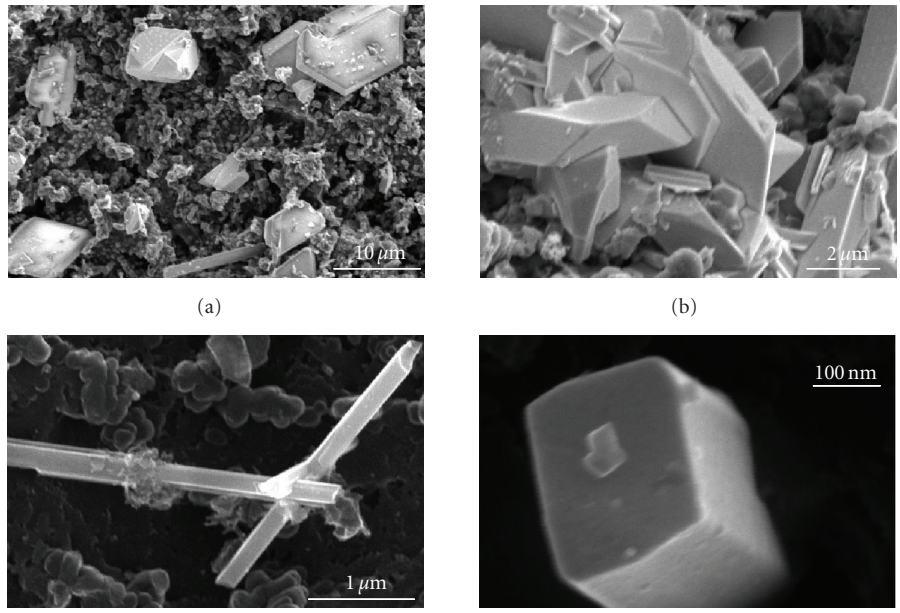

Figure 5: SEM micrographs of pyrolyzed PHC reveal micro and nanostructures interspersed in the bulk material.

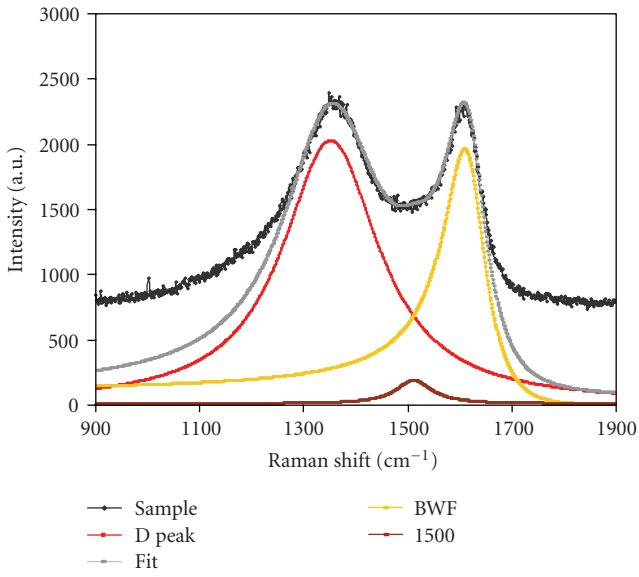

Figure 6: An improvement to the curve fit shown in Figure 4 can be made by adding another Lorentzian function at 1513 cm^{-1}.

product (Figure 5). We attempted to account for this material by adding an additional Lorentzian to the curve-fitting procedure (Figure 6). The added Lorentzian is relatively small in magnitude is centered at 1513 cm^{-1}, and improves the curve fitting of the sample's spectrum. Interestingly, an ~1500 cm^{-1} peak in the spectrum of a related polymer precursor, poly(phenylcarbyne) $(C_6H_5C)_n$, was observed after laser irradiation [15]. It has been suggested that such a peak could arise due to either impurity-carbon amorphous networks or amorphous networks of sp^2 and sp^3 carbon [16]. However, only the latter suggestion is applicable to our method of pyrolysis. Therefore, the micro and nanostructures interspersed throughout the bulk may be comprised of such three- and four-fold coordinated amorphous carbon networks.

4. Conclusion

We have developed a novel and facile method for the synthesis of PHC, an easily processed, insulating polymer. Upon pyrolysis in inert atmosphere, we note a significant increase in conductivity of the product with respect to the precursor for the sample we investigated. The majority of the product analyzed was shown to be consistent with small-crystalline graphite by way of curve fitting the sample's Raman spectrum. An improved curve fitting was found through incorporation of an additional minority constituent contributing to the spectrum at ~1500 cm^{-1}. This contribution may be the result of micro and nanostructures within the bulk observed by SEM.

References

[1] P. A. Bianconi, S. J. Joray, B. L. Aldrich, et al., "Diamond and diamond-like carbon from a preceramic polymer," *Journal of the American Chemical Society*, vol. 126, no. 10, pp. 3191–3202, 2004.

[2] J. Isberg, J. Hammersberg, E. Johansson, et al., "High carrier mobility in single-crystal plasma-deposited diamond," *Science*, vol. 297, no. 5587, pp. 1670–1672, 2002.

[3] C. E. Nebel, N. Yang, H. Uetsuka, T. Yamada, and H. Watanabe, "Quantized electronic properties of diamond," *Journal of Applied Physics*, vol. 103, no. 1, Article ID 013712, 5 pages, 2008.

[4] J. K. Luo, Y. Q. Fu, H. R. Le, J. A. Williams, S. M. Spearing, and W. I. Milne, "Diamond and diamond-like carbon MEMS," *Journal of Micromechanics and Microengineering*, vol. 17, no. 7, pp. S147–S163, 2007.

[5] J.-I. Chao, E. Perevedentseva, P.-H. Chung, et al., "Nanometer-sized diamond particle as a probe for biolabeling," *Biophysical Journal*, vol. 93, no. 6, pp. 2199–2208, 2007.

[6] S. Pisana, C. Casiraghi, A. C. Ferrari, and J. Robertson, "Roughness evolution during growth of hydrogenated tetrahedral amorphous carbon," *Diamond and Related Materials*, vol. 15, no. 4–8, pp. 898–903, 2006.

[7] L. Zhang, M. Chen, Z. Li, D. Chen, and S. Pan, "Effect of annealing on structure and haemocompatibility of tetrahedral amorphous hydrogenated carbon films," *Materials Letters*, vol. 62, no. 6-7, pp. 1040–1043, 2008.

[8] M. W. Pitcher and L. K. Toppare, "A new industrially viable method for the production of polycarbynes," US patent no. 60831172, 2006.

[9] G. T. Visscher, D. C. Nesting, J. V. Badding, and P. A. Bianconi, "Poly(phenylcarbyne): a polymer precursor to diamond-like carbon," *Science*, vol. 260, no. 5113, pp. 1496–1499, 1993.

[10] G. T. Visscher and P. A. Bianconi, "Synthesis and characterization of polycarbynes, a new class of carbon-based network polymers," *Journal of the American Chemical Society*, vol. 116, no. 5, pp. 1805–1811, 1994.

[11] A. C. Ferrari, "Raman spectroscopy of graphene and graphite: disorder, electron-phonon coupling, doping and nonadiabatic effects," *Solid State Communications*, vol. 143, no. 1-2, pp. 47–57, 2007.

[12] X. B. Yan, T. Xu, G. Chen, H. W. Liu, and S. R. Yang, "Effect of deposition voltage on the microstructure of electrochemically deposited hydrogenated amorphous carbon films," *Carbon*, vol. 42, no. 15, pp. 3103–3108, 2004.

[13] D. G. McCulloch, S. Prawer, and A. Hoffman, "Structural investigation of xenon-ion-beam-irradiated glassy carbon," *Physical Review B*, vol. 50, no. 9, pp. 5905–5917, 1994.

[14] R. Escribano, J. J. Sloan, N. Siddique, N. Sze, and T. Dudev, "Raman spectroscopy of carbon-containing particles," *Vibrational Spectroscopy*, vol. 26, no. 2, pp. 179–186, 2001.

[15] Y. F. Lu, S. M. Huang, and Z. Sun, "Raman spectroscopy of phenylcarbyne polymer films under pulsed green laser irradiation," *Journal of Applied Physics*, vol. 87, no. 2, pp. 945–951, 2000.

[16] R. J. Nemanich, J. T. Glass, G. Lucovsky, and R. E. Shroder, "Raman-scattering characterization of carbon bonding in diamond and diamond like thin-films," *Journal of Vacuum Science and Technology A*, vol. 6, no. 3, pp. 1783–1787, 1988.

Hindawi Publishing Corporation
Journal of Nanomaterials
Volume 2009, Article ID 204281, 8 pages
doi:10.1155/2009/204281

Research Article

Strength and Fracture Resistance of Amorphous Diamond-Like Carbon Films for MEMS

K. N. Jonnalagadda[1] and I. Chasiotis[2]

[1] *Mechanical Engineering, Johns Hopkins University, Baltimore, MD 21218, USA*
[2] *Aerospace Engineering, University of Illinois at Urbana-Champaign, Urbana, IL 61801, USA*

Correspondence should be addressed to I. Chasiotis, chasioti@uiuc.edu

Received 6 December 2008; Accepted 22 May 2009

Recommended by Rakesh Joshi

The mechanical strength and mixed mode I/II fracture toughness of hydrogen-free tetrahedral amorphous diamond-like carbon (ta-C) films, grown by pulsed laser deposition, are discussed in connection to material flaws and its microstructure. The failure properties of ta-C were obtained from films with thicknesses 0.5–3 μm and specimen widths 10–20 μm. The smallest test samples with 10 μm gage section averaged a strength of 7.3 $\pm$ 1.2 GPa, while the strength of 20-μm specimens with thicknesses 0.5–3 μm varied between 2.2–5.7 GPa. The scaling of the mechanical strength with specimen thickness and dimensions was owed to deposition-induced surface flaws, and, only in the smallest specimens, RIE patterning generated specimen sidewall flaws. The mode I fracture toughness of ta-C films is $K_{Ic} = 4.4 \pm 0.4\,\text{MPa}\sqrt{\text{m}}$, while the results from mixed mode I/II fracture experiments with cracks arbitrarily oriented in the plane of the film compared very well with theoretical predictions.

1. Introduction

The application of novel structural materials, such as nanocrystalline diamond [1] and amorphous diamond like carbon [2], in micro/nano-electromechanical systems (MEMS/NEMS) has increased in the recent years due to their advantageous mechanical and tribological properties. In order to expedite the insertion of these thin film materials in MEMS applications, thorough understanding of their mechanical behavior is required. In this regard, several experimental methods have been developed to measure the elastic and failure properties of materials for use in MEMS devices. A thorough literature review is provided in [3].

In this paper, previously reported and new results from toughness and mechanical strength experiments are presented in order to obtain further understanding of the reliability of hydrogen-free tetrahedral amorphous diamond-like carbon (ta-C) manufactured at the Sandia National Laboratories. Results from mixed mode stress intensity factors, K_I and K_{II}, are presented and discussed in terms of material fabrication, specimen size effects, and residual stress gradients.

2. Experiments

2.1. Specimen Preparation. The ta-C specimens were manufactured at the Sandia National Laboratories [4] from a graphite target by pulsed laser deposition (PLD). They were composed of 70–80% sp^3 and 20–30% sp^2 carbon. Their composition depended on the laser fluence, which was >25 J. The as-deposited ta-C consisted of uniformly distributed sp^2 and sp^3 phases [5] but it has been reported that small clusters of sp^2 phase form after thermal annealing, which are of the order of 1–3 nm [6]. During room-temperature deposition, subplantation of accelerated carbon atoms towards the substrate caused residual stresses of 6–12 GPa in as-deposited films [7]. These stresses were relieved by annealing the samples at 600°C for a few minutes in Ar, which reduced the stresses to less than 1 GPa. The high compressive stresses during deposition can cause film delamination from its substrate and, therefore, a maximum single layer thickness of about 200 nm is permitted. Thicker films can be deposited in the form of multiple layers with annealing performed after each deposition of each layer. In order to fabricate MEMS devices from ta-C, the films are

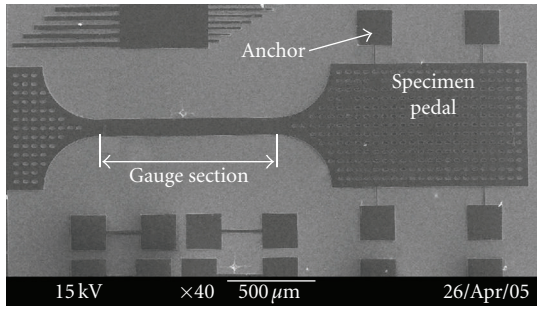

Figure 1: SEM micrograph of a ta-C microscale tension dog-bone specimen. The specimen pedal is used to grip the specimen and to apply a tensile load to the gauge section.

patterned by using aluminum mask and oxygen plasma [4]. Figure 1 shows the top view of a ta-C specimen anchored to a substrate by tethers which are connected to the square pads. The specimens for fracture mechanics studies were 100 μm wide, 1 μm thick, and 1000 μm long. The specimens used for fracture strength experiments were 20 μm wide, 500, or 1000 μm in length and 0.5-3.0 μm in thickness. Four different thicknesses were used to establish the effect of processing parameters on the mechanical failure of ta-C films.

The elastic properties of these films were presented in previous publications. The average elastic modulus for all thicknesses, as measured by uniaxial tension specimens and the AFM/DIC method [8], was 843 ± 54 GPa and their Poisson's ratio was 0.17 ± 0.03 [9, 10].

2.2. Preparation of Mixed Mode I/II Fracture Specimens. The procedure for creating oblique precracks for the mixed-mode fracture experiments is similar to the one employed for the mode-I fracture toughness work by the authors before [11]. Pre-cracks were introduced in the fracture specimens by microindentation as previously reported by the authors [10, 12] and first discussed by Keller [13] and Ballarini et al. [14]. A microindent was made next to the edge of unreleased specimens while they were attached on a silicon dioxide sacrificial layer. The radial median crack generated from the indent created a pre-crack in the specimen, as shown in Figure 2. The indenter was suitably rotated to form pre-cracks at various angles with different crack lengths. Specimens with pre-cracks that were straight along their entire length were used in the fracture experiments. The oblique pre-cracks allowed for uniaxial loading in the gauge section and various combinations of tensile and shear stresses at the crack tip.

To reduce the uncertainty in measuring the pre-crack geometry, and consequently the computed stress intensity factors (SIFs), scanning electron microscopy (SEM) micrographs provided the overall orientation of the crack with respect to the edge of the specimen, whereas, AFM images showed the local details of the crack tip. An accuracy of 10 nm in measuring the pre-crack length and of 1° or better in the measured pre-crack angle can be achieved by using an AFM. The crack lengths were in the range of 12–29 μm and the crack angles varied from 7°–38°. Film thickness measurements were performed by a surface profilometer and an SEM.

After the geometry measurements, the specimens were released from their substrate by wet etching the SiO_2 sacrificial layer in 49 wt.% HF and by performing CO_2 critical point drying (CPD). The same etching procedure was followed to obtain the freestanding tension the specimens for fracture strength measurements. SEM micrographs after specimen release showed no further pre-crack extension, while the pre-cracks "closed," asserting the fact that the pre-cracks were indeed sharp with singular crack tips.

2.3. Calculation of Strength and Mixed Mode I/II Fracture Toughness from Experiments. The freestanding specimens were tested in fixed-fixed configuration [12]. An important aspect of these fracture experiments was to ensure that loading was uniform and that no bending moment was applied in the in-plane direction. Loading was accomplished with a PZT actuator (Polytec PI) with a 1 nm displacement resolution and ~0.5% linearity. The force applied to the specimens was measured with a load cell (quasistatic) with a resolution of 0.1 mN and 1% linearity (with respect to its full-scale). Ta-C is brittle, linearly elastic, and because of its insignificant (calculated) process zone, see reference [10], the use of the plane strain assumption at the crack tip is valid in computing the stress intensity factors. The measured stress just before specimen failure is used in the calculations of the fracture strength and the stress intensity factor (SIF).

The majority of the fracture strength measurements were conducted with 20-μm wide specimens that had four different thicknesses, 0.5 μm, 1 μm, 2.2 μm, and 3 μm, and two different lengths, 500 μm and 1000 μm. The independent variation of the specimen outer surface area and volume, allowed quantifying the specimen size dependence of the measured mechanical strength. The load drop at failure and the cross-sectional area were used to compute the fracture strength. For each specimen thickness and length several experiments were conducted and their average values are reported here plus/minus one standard deviation.

The mixed-mode I/II stress intensity factors, K_I and K_{II}, for an oblique edge crack in a 2D plate under uniaxial tension, see Figure 3, are [15]

$$\begin{aligned} K_I &= Y_I \sigma_\infty \sqrt{\pi a} \cos^2(\theta), \\ K_{II} &= Y_{II} \sigma_\infty \sqrt{\pi a} \sin(\theta) \cos(\theta), \end{aligned} \tag{1}$$

where Y_I and Y_{II} are the mode-I and mode-II shape factors, associated with finite width specimen, which depend on the dimensions of the specimen, the crack length, a, and the pre-crack angle, θ.

Due to the nonstandard specimen geometry and load application in our mixed mode fracture experiments, there are no closed form solutions available to calculate K_I and K_{II} directly from boundary (stress) measurements. Instead, a finite element (FE) analysis was conducted to deduce the fracture parameters from our experimental data. Figure 3 shows the boundary conditions used in the FE analysis to extract K_I and K_{II}. The specimen length in the model was

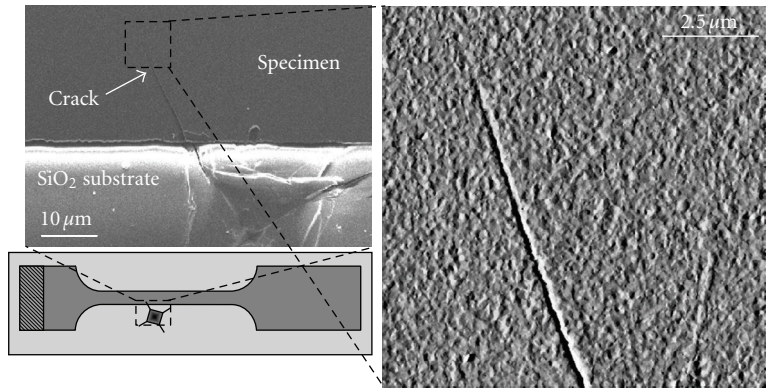

FIGURE 2: (Left) Indent next to a specimen edge and SEM micrograph of a microindent used to generate oblique edge pre-crack in a ta-C specimen. (Right): AFM image of a pre-crack and its tip.

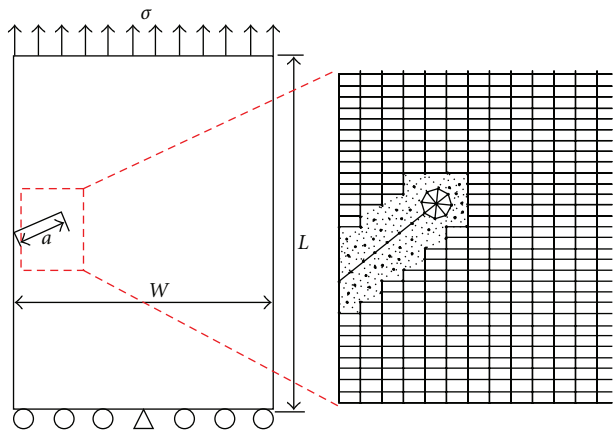

FIGURE 3: Specimen model showing the boundary conditions and the finite element mesh in the vicinity of the crack tip used in numerical calculations of the stress intensity factors.

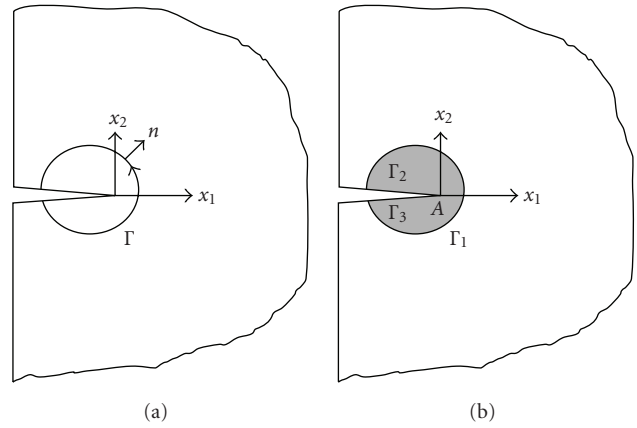

FIGURE 4: (a) Crack tip coordinate system in an infinite body for J-integral evaluation and (b) equivalent area domain for J-integral evaluation [19].

$L = 5w$. It was verified that the model geometry and its relative dimensions did not bias the computed K_I and K_{II}. The deformation fields and the stress intensity factors were calculated by FRANC2DL [16, 17]. This interactive FE analysis program allows for 2D modeling of cracks in solids and for calculating stress intensity factors via displacement correlation, modified crack closure integral, and J-integral based formulations. The J-integral method gave the most consistent results in our mixed mode stress intensity factor calculations.

The J-integral is a non-linear, elastic path independent, integral defined as [18]

$$J = \lim_{\Gamma \to 0} \int_{\Gamma} \left[W n_1 - \sigma_{ij} \frac{\partial u_i}{\partial x_1} n_j \right] d\Gamma, \tag{2}$$

where W is the strain energy density, σ is the stress tensor, n is the unit vector normal to the contour Γ, and u is the displacement vector, as shown in Figure 4(a). For a homogeneous linearly elastic material, J is equal to G, the energy release rate.

For this mixed mode plane strain fracture problem, J or G is equal to

$$J = G = \frac{(K_I^2 + K_{II}^2)(1 - \nu^2)}{E}, \tag{3}$$

where E is the elastic modulus and ν is the Poisson's ratio. This domain integral was later modified by Li et al. [20] into an area integral suitable for finite element calculations, as shown in Figure 4(b). The area form of the integral is [18]

$$\bar{J} = \int_A \left[\sigma_{ij} \frac{\partial u_i}{\partial x_1} - W \delta_{1j} \right] \frac{\partial q_1}{\partial x_i} dA, \tag{4}$$

where δ is the Kronecker delta and q is the weight function defined over the domain of integration. The value of q should be such that it is equal to zero at the crack tip and equal to *one* on the boundary [18]. It is seen that J or G in (3) are a combination of the stress intensity factors, K_I and K_{II}, which are separated into different fracture modes via a technique introduced by Ishikawa [19] and Bui [21]. The crack tip displacements were decomposed into their symmetric $\underset{\sim}{u}_I$ and antisymmetric $\underset{\sim}{u}_{II}$ components with respect to the crack.

Similarly, a decomposition of the stress field was obtained and the mode separated J-integral values and the plane strain SIFs are computed as

$$\bar{J}_I = \bar{J}_I\left(\underset{\sim}{u}_I, \underset{\sim}{\sigma}_I\right) \qquad \bar{J}_{II} = \bar{J}_{II}\left(\underset{\sim}{u}_{II}\underset{\sim}{\sigma}_{II}\right),$$
$$K_I = \sqrt{\frac{E\bar{J}_I}{(1-\nu^2)}} \qquad K_{II} = \sqrt{\frac{E\bar{J}_{II}}{(1-\nu^2)}}. \tag{5}$$

Finally, the values of K_I and K_{II} were extracted from the mixed mode fracture experimental data and the J-integral technique was implemented in FRANC2DL.

In terms of meshing, 6-node quarter point triangular elements (T6) were employed to capture the crack tip singularity. The mesh was refined around the crack tip until convergence was achieved. The rest of the model was meshed with 8-node bilinear quad elements. Figure 3 shows the mesh generated for a finite width specimen with an edge crack. For each sample tested a new mesh was generated to accommodate the new crack length and angle. The boundary conditions were set to satisfy the fixed-fixed loading configuration shown in Figure 3. Benchmark fracture problems were solved first and the computed SIFs were compared with those obtained by other methods to ensure the convergence and accuracy of the numerical solution with respect to the mesh density and element size. For instance, the case of a single edge crack in a very large plate was solved and the SIF was compared with the analytical solution [17], and the SIF values computed by Kim and Paulino [22] who used the M-integral in conjunction with the boundary element method (BEM).

3. Results and Discussion

3.1. Mechanical Strength Experiments. Table 1 lists the average tensile strength and its standard deviation as a function of specimen thickness and length [23]. In general, the tensile strength scaled adversely with the film thickness, Figure 5(a), when the specimen length was maintained the same. The thinnest films, 0.5 μm, did not demonstrate a change in their mechanical strength with the specimen length, which implies that, for small film thicknesses, there is a statistically representative (shown by the decrease in the standard deviation of strength values) surface flaw population in both small and large samples, which could be a combination of top and side wall film surface flaws of small size. Hence, for this film thickness the flaw population in a $20 \times 500\,\mu\text{m}^2$ film area was representative of the flaw distribution in the entire film deposited on the die and, therefore, the value for the mechanical strength of 5.4 ± 1.2 GPa is representative for the 0.5 μm thick ta-C films provided that they are comparable or larger in surface area than the tested specimens. SEM images actually showed randomly distributed small flaws which were of the order of a few nanometers and, potentially, the source of failure where the side-wall specimen ridges. However, the mechanical strength of brittle materials is considered a stochastic property and when stringent reliability requirements are in place then very conservative material proofing approaches are needed [24].

Table 1: Tensile strength of ta-C as a function of specimen dimensions.

Thickness (μm)	Length (μm)	Tensile Strength (GPa)
0.5	500	5.4 ± 1.2
	1000	5.7 ± 0.3
1.0	500	5.5 ± 0.9
	1000	3.9 ± 0.7
2.2	500	4.3 ± 1.4
	1000	3.4 ± 0.9
3.0	500	2.2 ± 0.5
	1000	2.3 ± 0.5

The same arguments are true for the thicker films, 3.0 μm, for which, the mechanical strength was independent of the specimen size. SEM images actually showed that the thickest films contained large surface flaws that initiated failure. Again, at this extreme of film thickness, the flaw population in $20 \times 500\,\mu\text{m}^2$ film area was representative of the flaw distribution in the entire film and, therefore, one may use this value, 2.2 ± 0.5 GPa, as a representative strength for the 3.0 μm films. In the thickest films, SEM images showed distributed large and deep flaws, some of which were submicron in size. One can then identify two different flaw populations, both distributed at the film surface/volume, whose size correlates with the film thickness, resulting in an apparent correlation between the specimen volume and its strength, as shown in Figure 5(b). However, this correlation is strongly biased by the strength data for the 3.0-μm films, and it does not have general applicability.

On the other hand, the strength of the two medium film thicknesses did vary with the specimen length. In these film thicknesses there was a distribution of small (similar to those in 0.5-μm films) and large flaws (similar to those in 3.0-μm films). Larger specimens contained larger number of large flaws that reduced the film strength significantly. Therefore, the detrimental flaws were not clearly volumetric (i.e., they still were surface flaws), since it was noticed that no flaws were entirely included inside a specimen; rather, all flaws discernible by an SEM were terminated at the specimen surface. Also, there were no flaws that started at the bottom surface of the films. Therefore, the failure-inducing flaws were attributed to carbon droplets that formed during deposition. As discussed in previous works for other brittle materials for MEMS, the existence of two or more competing flaw populations requires a thorough stress analysis of MEMS components fabricated by these films, since it is the local stress distribution that dictates the active (catastrophic) flaw population [25].

Tests conducted on ta-C fixed-fixed beams by Espinosa et al. [26] made of 0.5 μm and 1 μm films resulted in strengths between 4.7–5.2 GPa, which agree with our experimental results for the same film thicknesses. Espinosa et al. [26] identified the sidewall roughness as the key factor in failure. The data presented here [25] probed the flaw populations in specimens with different dimensions of top and sidewall surfaces pointing out that the flaws are rather volume related

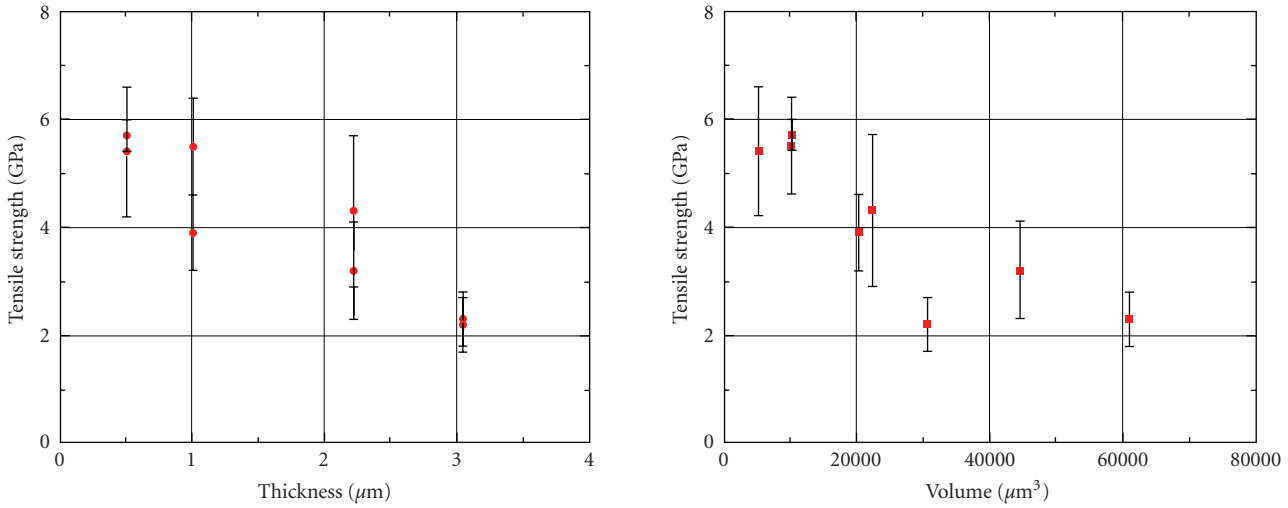

FIGURE 5: Tensile strength of ta-C as a function of specimen (a) thickness, (b) volume. The error bars correspond to one standard deviation [25].

(i.e., deep top surface flaws that span significant volume inside the specimens.) An appropriate scaling of the failure problem would involve the top surface of the films and would be conducted separately for each film thickness. The sidewall flaws are usually small and have been shown to be the source of failure in very small components. In a previous work by this group [9] 10-μm wide and 400-μm long ta-C specimens with 1.5 μm average thickness provided a tensile strength of 7.3 $\pm$ 1.2 GPa, while having the same, or larger, sidewall surface as more than half of the samples listed in Table 1. In the same publication [9] the authors showed that when the effect of top surface flaws was minimized by focusing the stresses to small volumes of very acute notches ($K = 27$) with a radius of curvature of 8 μm, the local mechanical strength was very consistent averaging 11.4 $\pm$ 0.8 GPa. In those cases, failure was indeed the result of the sidewall ridges in the specimen. The last point was supported by a study with microscale polycrystalline silicon specimens [27], which showed that sidewall flaw populations are responsible for failure at locations with high stress concentration factors or small radii of curvature. It should be noted, that the choice of mechanical tests and the geometry and dimensions of brittle specimens can seriously bias the outcome of material strength measurements. The results from such experiments should be analyzed and applied with caution.

3.2. Mixed Mode I/II Fracture Toughness Experiments. The mixed mode I/II fracture experiments were conducted on 1-μm thick specimens from *two* dies, originating in two different fabrication runs. The choice of film thickness was made according to the residual stress gradient in the unreleased films. Prior work showed that 1-μm films are the most appropriate to use because they are subject to a minimal effect of residual stress gradients [10]. The experiments conducted by taking this consideration into account resulted

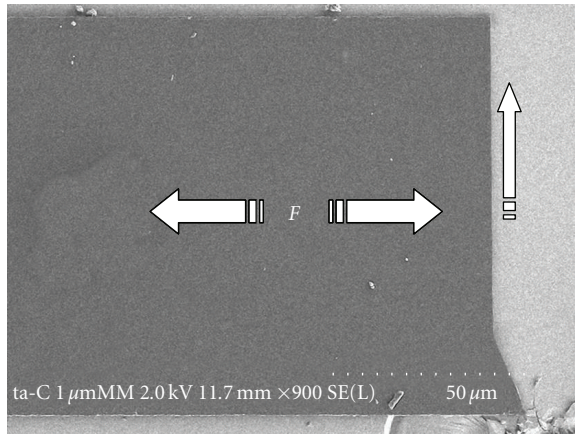

FIGURE 6: SEM micrograph of a fractured ta-C specimen showing the pre-crack (bottom) and the direction of crack propagation pointed by the vertical arrow.

in the expected mode of crack propagation. Figure 6 shows an SEM micrograph of a fractured ta-C specimen with a 30° pre-crack angle. The fracture path followed a straight line which was normal to the loading direction, indicating properly conducted experiments, as an oblique pre-crack propagates in mode I after an initiation angle and a short smooth transition from the original pre-crack angle.

The normalized stress intensity factors computed by using FRANC2DL, K_I/K_{IC}, and K_{II}/K_{IC}, where K_{IC} is the mode-I fracture toughness of ta-C, are plotted in Figure 7. The experimental uncertainty was less than 3% and 4% for K_I and K_{II}, respectively. The number next to each datum point is the pre-crack angle. The critical conditions for crack initiation in mixed mode I/II fracture and the direction of crack propagation depend on the local stress field around the crack tip. The two common theoretical criteria [17] for

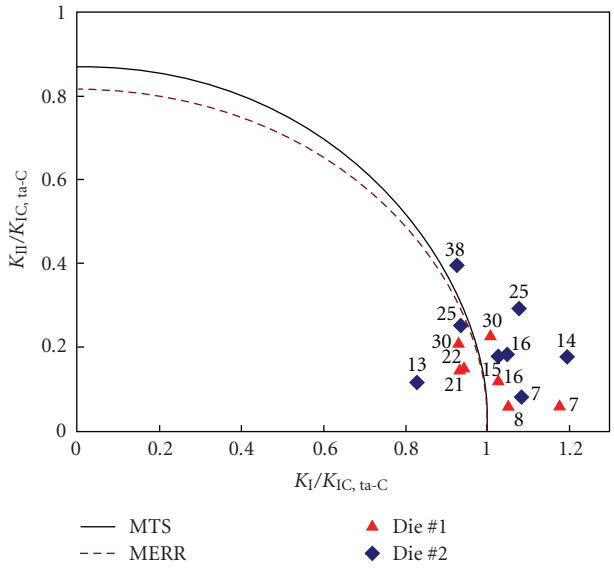

Figure 7: Normalized mixed mode stress intensity factors, K_I/K_{IC} versus K_{II}/K_{IC} for ta-C specimens. The experimental data are compared to predictions by the MERR (dashed line) and the MTS (solid line) criteria. The numbers next to the data points are the pre-crack angles.

critical crack initiation are based on the maximum tensile (or hoop) stress (MTS) [27] and the maximum energy release rate (MERR) [28]. Using these mixed-mode I/II failure criteria the locus of K_I/K_{IC} versus K_{II}/K_{IC} is plotted in Figure 7 with solid and dashed lines, respectively. These two fracture criteria provide an appropriate base for comparison with theory since ta-C is amorphous and can be treated as homogeneous and isotropic at almost all length scales.

The critical stress intensity factor, K_{IC}, used to normalize the mixed mode SIFs, was obtained from mode I experiments on specimens from the same die. This way we accounted (to some extent) for the material and gradient stress variations between the *two* dies. The mode I critical stress intensity factors for the *two* dies were 3.1 MPa $\sqrt{\text{m}}$ and 3.9 MPa $\sqrt{\text{m}}$ for die number 1 and die number 2, respectively. For each die K_I and K_{II} followed a rather monotonic trend. Without the datum point for the 7° pre-crack in die number 1, and the data points for 13° and 14° pre-cracks in die number 2, the experimental data fit the theoretical criteria very well. Actually, when compared to mixed mode I/II fracture parameters from amorphous brittle materials at the macroscale, such as PMMA [29], a similar distribution of values is seen, often with a broader distribution of values. The deviation from the MTS and MERR criteria is potentially due the stress gradient in the films before their release from their substrate, which results in a (slight) curvature in the test samples. Upon loading, this curvature is removed resulting in a bending moment at the crack tip. So the difference in K_{Ic} values between the two dies is owed to the originally different residual stress gradients in the deposited ta-C and consequently, it does not represent the intrinsic K_{Ic} value of the material. For a measurement of the intrinsic K_{Ic} of ta-C the reader is referred to reference [10] where it was found that $K_{Ic} = 4.4 \pm 0.4\,\text{MPa}\sqrt{m}$, which was consistent for ta-C specimens from different dies, which were subject to negligible residual stress gradients before their release.

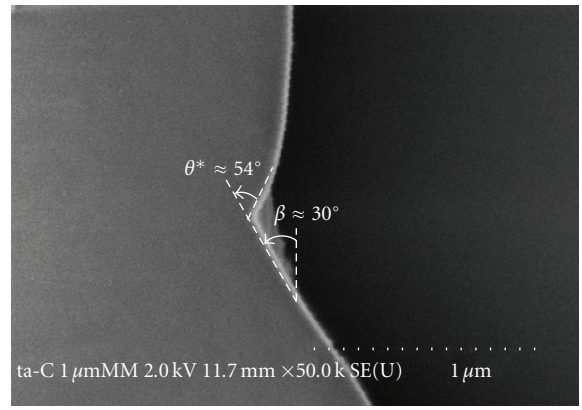

Figure 8: SEM micrograph showing the pre-crack, 30°, and the crack initiation, 54°, angles.

Finally, Figure 8 is a close up view of the pre-crack tip after fracture. At the onset of fracture, the crack propagated in the direction of the crack initiation angle and finally became normal to the loading direction. For the pre-crack angle $\beta = 30°$ the crack initiation angle was measured to be 54°. The crack initiation angle is related to the mixed mode stress intensity factors by [17]:

$$\frac{K_{II}}{K_I} = \tan(\theta) = \frac{-\sin(\beta)}{3\cos(\beta) - 1}, \tag{6}$$

where β is the critical crack initiation angle for a given θ. For instance, in this example the predicted initiation angle was 59°, which was close to the experimentally measured value.

4. Conclusions

Nanostructured materials applied to MEMS/NEMS can guarantee uniformity in their properties, that is, their effective mechanical behavior is not a function of their dimensions. On the other hand, the failure properties still depend on the size of the MEMS components. Small ta-C material volumes demonstrated high strength; the strength of acute notches with radii of curvature of 8 μm was 11.4 ± 0.8 GPa, as opposed to the strength of uniform tension ta-C specimens which was quite lower and with greater scatter in values. Thus, the high mechanical strength is an intrinsic asset of ta-C but its failure is controlled by submicron flaws that are independent of the material nanostructure and originate in the film deposition and patterning processes. The mechanical strength of the ta-C specimens tested here did not scale with the specimen volume because of the existence of two flaw populations whose density and severity varied with the film thickness; the thinnest films contained only the smallest flaws while the thickest films had significantly larger flaws. On the other hand, the intermediate film thicknesses shared both flaw types. Therefore, one may apply a Weibull

analysis to make failure probability predictions only with strength data from films of the same thickness.

As a consequence, the mechanical strength of ta-C, although intrinsically very high, is limited by fabrication hurdles. Hence, it is not an appropriate metric to compare brittle thin film materials in order to make material selections for MEMS devices, since the failure-inducing defects are not intrinsic and very often can be reduced in numbers and size or even be eliminated. In this regard, the fracture toughness is a better measure of the material durability and intrinsic failure consistency since it can probe the average material bond strength (for a brittle material) and its uniformity throughout a thin film. The high fracture toughness of ta-C, when compared to that of other films for MEMS such as polysilicon [12], places ta-C among the most failure resistant brittle materials. In this paper it was further shown that because of the amorphous nature of ta-C, more complex, and also more realistic cases of fracture, that is, mixed mode I/II fracture can be predicted very well with the aid of brittle fracture criteria derived from continuum mechanics.

Acknowledgments

The authors gratefully acknowledge the support by the Air Force Office of Scientific Research (AFOSR) through Grants F49620-03-1-0080 and FA9550-09-1-0535 with Doctor B. L. Lee as the program monitor, and by the National Science Foundation (NSF) under Grant CMS 05-15111. The authors thank Doctors T. A. Friedman, and J. P. Sullivan from the Sandia National Laboratories for providing the ta-C specimens for this work.

References

[1] D. M. Gnien, "Nanocrystalline diamond films," *Annual Review of Materials Science*, vol. 29, pp. 211–259, 1999.

[2] T. A. Friedmann, K. F. McCarty, J. C. Barbour, M. P. Siegal, and D. C. Dibble, "Thermal stability of amorphous carbon films grown by pulsed laser deposition," *Applied Physics Letters*, vol. 68, no. 12, pp. 1643–1645, 1996.

[3] I. Chasiotis and W. G. Knauss, "Experimentation at the micron- and submicron scale," in *Comprehensive Structural Integrity Vol. 8. Interfacial and Nanoscale Failure*, W. Gerberich and W. Yang, Eds., pp. 41–87, Elsevier Science, Oxford, UK, 2003.

[4] J. P. Sullivan, T. A. Friedmann, M. P. de Boer, et al., "Developing a new material for MEMS: amorphous diamond," in *Proceedings of the Materials Research Society Symposium*, vol. 657, 2001.

[5] M. P. Siegal, J. C. Barbour, P. N. Provencio, D. R. Tallant, and T. A. Friedmann, "Amorphous-tetrahedral diamondlike carbon layered structures resulting from film growth energetics," *Applied Physics Letters*, vol. 73, no. 6, pp. 759–761, 1998.

[6] J. P. Sullivan, T. A. Friedmann, and A. G. Baca, "Stress relaxation and thermal evolution of film properties in amorphous carbon," *Journal of Electronic Materials*, vol. 26, no. 9, pp. 1021–1029, 1997.

[7] T. A. Friedmann, J. P. Sullivan, J. A. Knapp, et al., "Thick stress-free amorphous-tetrahedral carbon films with hardness near that of diamond," *Applied Physics Letters*, vol. 71, no. 26, pp. 3820–3822, 1997.

[8] I. Chasiotis and W. G. Knauss, "A new microtensile tester for the study of MEMS materials with the aid of atomic force microscopy," *Experimental Mechanics*, vol. 42, no. 1, pp. 51–57, 2002.

[9] S. Cho, I. Chasiotis, T. A. Friedmann, and J. P. Sullivan, "Young's modulus, Poisson's ratio and failure properties of tetrahedral amorphous diamond-like carbon for MEMS devices," *Journal of Micromechanics and Microengineering*, vol. 15, no. 4, pp. 728–735, 2005.

[10] K. Jonnalagadda, S. W. Cho, I. Chasiotis, T. Friedmann, and J. Sullivan, "Effect of intrinsic stress gradient on the effective mode-I fracture toughness of amorphous diamond-like carbon films for MEMS," *Journal of the Mechanics and Physics of Solids*, vol. 56, no. 2, pp. 388–401, 2008.

[11] S. W. Cho, K. Jonnalagadda, and I. Chasiotis, "Mode I and mixed mode fracture of polysilicon for MEMS," *Fatigue and Fracture of Engineering Materials and Structures*, vol. 30, no. 1, pp. 21–31, 2007.

[12] I. Chasiotis, S. W. Cho, and K. Jonnalagadda, "Fracture toughness and subcritical crack growth in polycrystalline silicon," *Journal of Applied Mechanics*, vol. 73, no. 5, pp. 714–722, 2006.

[13] C. Keller, *Microfabricated High Aspect Ratio Silicon Flexures*, MEMS Precision Instruments, El Cerrito, Calif, USA, 1998.

[14] R. Ballarini, R. L. Mullen, Y. Yin, H. Kahn, S. Stemmer, and A. H. Heuer, "The fracture toughness of polysilicon microdevices: a first report," *Journal of Materials Research*, vol. 12, no. 4, pp. 915–922, 1997.

[15] T. L. Anderson, *Fracture Mechanics*, CRC Press, Boston, Mass, USA, 2nd edition, 1995.

[16] A. R. Ingraffea and P. A. Wawrzynek, "Finite element methods for linear elastic fracture mechanics," in *Comprehensive Structural Integrity*, R. de Borst and H. Mang, Eds., Elsevier Science, Oxford, UK, 2003.

[17] FRANC2DL Version 2.2, http://www.cfg.cornell.edu/software/franc2dl.htm.

[18] J. R. Rice, "A path independent integral and the approximate analysis of strain concentration by notches and cracks," *Journal of Applied Mechanics*, vol. 35, pp. 379–386, 1968.

[19] H. Ishikawa, "A finite element analysis of stress intensity factors for combined tensile and shear loading by only a virtual crack extension," *International Journal of Fracture*, vol. 16, no. 5, pp. R243–R246, 1980.

[20] F. Z. Li, C. F. Shih, and A. Needleman, "A comparison of methods for calculating energy release rates," *Engineering Fracture Mechanics*, vol. 21, no. 2, pp. 405–421, 1985.

[21] H. D. Bui, "Associated path independent J-integrals for separating mixed modes," *Journal of the Mechanics and Physics of Solids*, vol. 31, no. 6, pp. 439–448, 1983.

[22] J.-H. Kim and G. H. Paulino, "T-stress, mixed-mode stress intensity factors, and crack initiation angles in functionally graded materials: a unified approach using the interaction integral method," *Computer Methods in Applied Mechanics and Engineering*, vol. 192, no. 11-12, pp. 1463–1494, 2003.

[23] S. W. Cho, *Nanoscale deformation and fracture mechanics of polycrystalline silicon and diamond-like carbon for MEMS by the AFM/DIC method*, Ph.D. thesis, University of Virginia, 2008.

[24] B. L. Boyce, R. Ballarini, and I. Chasiotis, "An argument for proof testing brittle microsystems in high-reliability applications," *Journal of Micromechanics and Microengineering*, vol. 18, no. 11, pp. 117001–117004, 2008.

[25] A. McCarty and I. Chasiotis, "Description of brittle failure of non-uniform MEMS geometries," *Thin Solid Films*, vol. 515, no. 6, pp. 3267–3276, 2007.

[26] H. D. Espinosa, B. Peng, N. Moldovan, et al., "Elasticity, strength, and toughness of single crystal silicon carbide, ultrananocrystalline diamond, and hydrogen-free tetrahedral amorphous carbon," *Applied Physics Letters*, vol. 89, no. 7, pp. 1–3, 2006.

[27] F. Erdogan and G. C. Sih, "On the crack extension in plates under plane loading and transverse shear," *Journal of Basic Engineering*, vol. 85, pp. 519–527, 1963.

[28] C. H. Wu, "Maximum-energy-release-rate criterion applied to a tension-compression specimen with crack," *Journal of Elasticity*, vol. 8, no. 3, pp. 235–257, 1978.

[29] R. V. Mahajan and K. Ravi-Chandar, "An experimental investigation of mixed-mode fracture," *International Journal of Fracture*, vol. 41, no. 4, pp. 235–252, 1989.